

Electronic Thesis and Dissertation Repository

4-22-2024 10:30 AM

Electrosprayed Serine Octamer Magic Number Cluster: Formation via Gas phase Assembly and Collision-Induced Dissociation


Vida Alinezhad, *Western University*

Supervisor: Konermann, Lars, *The University of Western Ontario*

A thesis submitted in partial fulfillment of the requirements for the Master of Science degree in Chemistry

© Vida Alinezhad 2024

Follow this and additional works at: <https://ir.lib.uwo.ca/etd>

 Part of the [Analytical Chemistry Commons](#), [Computational Chemistry Commons](#), and the [Physical Chemistry Commons](#)

Recommended Citation

Alinezhad, Vida, "Electrosprayed Serine Octamer Magic Number Cluster: Formation via Gas phase Assembly and Collision-Induced Dissociation" (2024). *Electronic Thesis and Dissertation Repository*. 10029.

<https://ir.lib.uwo.ca/etd/10029>

This Dissertation/Thesis is brought to you for free and open access by Scholarship@Western. It has been accepted for inclusion in Electronic Thesis and Dissertation Repository by an authorized administrator of Scholarship@Western. For more information, please contact wlsadmin@uwo.ca.

Abstract

Magic number clusters refer to ion species that exhibit unusually high intensities in electrospray ionization (ESI) mass spectrometry (MS) experiments. The serine octamer cluster $[\text{Ser}_8\text{H}]^+$ is of special interest since its formation mechanism and structure remain controversial, although a recently proposed model in the literature represents a possible candidate structure. Nonetheless, the formation mechanism of $[\text{Ser}_8\text{H}]^+$ remains unexplored. Some hypotheses suggest that it may pre-exist in bulk solution, or that $[\text{Ser}_8\text{H}]^+$ can be a collision-induced dissociation (CID) product of large clusters formed in evaporating ESI droplets. We used ESI-MS, mobile proton molecular dynamics (MPMD) simulations, and density functional theory (DFT) to probe the mechanism of ESI-induced $[\text{Ser}_8\text{H}]^+$ formation. The results obtained rule out existence of $[\text{Ser}_8\text{H}]^+$ in bulk. Additionally, our data reveal that initial Ser clusters formed in shrinking ESI droplets are unstable and undergo CID. Ser monomers released during these dissociation events undergo low-temperature recluster during free jet expansion. Subsequent CID events culminate in Ser_8H^+ -dominated mass spectra.

Keywords

electrospray ionization, mass spectrometry, serine magic number cluster, molecular dynamics simulations, density functional theory, mobile proton algorithm

Summary for Lay Audience

Mass spectrometry (MS) is a technique used in research and industry for qualitative and quantitative analyses (e.g., blood samples, petrochemicals, etc). To introduce analytes into the vacuum chamber of a mass spectrometer, various methods are available. Electrospray ionization (ESI) is one of the most used approaches that includes application of a high voltage to a conductive capillary containing the analyte solution. This voltage subsequently results in ionization of the analytes. One interesting property of mass spectrometers is their ability to mimic interstellar conditions. This makes the instruments indispensable to investigate molecules/compounds that form in vacuum.

Magic number clusters (MNC) are ions that show an unusually high abundance in mass spectrometry experiments. The serine octamer cluster is one particularly interesting MNC, as both its structure and formation mechanism remain incompletely understood. Existing hypotheses suggest that the cluster pre-exists in bulk solution or that it forms within evaporating ESI nanodroplets. Subsequent dissociation events may then produce the experimentally observable $[\text{Ser}_8+\text{H}]^+$.

In this thesis, MS experiments, molecular dynamics simulation (MD), and density functional theory (DFT) were utilized to investigate the formation mechanism of $[\text{Ser}_8+\text{H}]^+$ and gain insights about its structure. In chapter 2, the results rule out the existence of the cluster in bulk and droplets, suggesting the existence of experimentally observable $[\text{Ser}_8+\text{H}]^+$ to be exclusive to vacuum conditions. On the basis of MS data and MD results, it is proposed that as ESI nanodroplets evaporate to dryness, Ser subunits aggregate and form large non-specific gaseous clusters. Dissociation of these nonspecific clusters is then followed by aggregation of neutral and positively charged Ser monomers in the gas phase. Subsequently, collision induced dissociation (CID) of these gas phase aggregates results in $[\text{Ser}_8+\text{H}]^+$.

Co-Authorship Statement

All experimental and computational work and data analysis was performed by the author under the supervision of Dr. Lars Konermann. Drafts of each chapter were prepared by the author. Subsequent revisions were performed in collaboration between the author and Dr. Lars Konermann. Python code for trajectory stitching and implementation of proton hopping in gas phase used in Chapter 2 was written by Dr. Konermann.

Acknowledgments

I would like to express my sincere gratitude to my supervisor, Dr. Lars Konermann. His mentorship has been constructive not only in my scientific development but also in my personal growth. Dr. Konermann made my master's journey a remarkable experience in my life. I feel grateful and absolutely satisfied to have had the opportunity of working on research that I was passionate about with a supervisor whom I will admire and respect for my lifetime.

I would like to acknowledge Dr. Viktor Staroverov for his valuable discussions on DFT.

My labmates Kasra, Kirsty, Evelyn, Elnaz, Nastaran, and Yousef thank you for being a great company and creating a welcoming and positive environment in the laboratory. A special thank you to Pablo who has been helpful with mass spectrometer training, always ready to answer my questions and provide help.

I am immensely grateful to Karuna DSouza for her significant assistance and support in times of crisis.

I would like to thank my friends all around the world for their unwavering support, shared laughter, and cherished memories.

I am profoundly thankful to Kayvan, who has been by my side since the beginning of this journey. You encouraged me to take every little or big step. Thanks for being my biggest cheerleader at all times. You believed in me during tough days and supported me in every possible way. I am so lucky to have someone who feels happier and prouder for my accomplishments than their own. Also, thanks for the delicious "Ghormeh Sabzis" you cooked while I was writing this thesis.

Last but not least, my heartfelt thanks go to my dear parents who have devoted their lives to my success and happiness and have always believed in me and my potential. My Lovely grandmother, my little brother, and my aunts Parvin and Fereshteh thank you for your unconditional love and support.

Table of Contents

Abstract.....	ii
Summary for Lay Audience.....	iii
Co-Authorship Statement.....	iv
Acknowledgments.....	v
Table of Contents.....	vi
List of Tables.....	ix
List of Figures.....	x
List of Appendices.....	xiii
List of Symbols and Abbreviations.....	xiv
Chapter 1.....	1
1 Introduction.....	1
1.1 Mass Spectrometry.....	1
1.2 Ion Source.....	2
1.2.1 Electrospray Ionization.....	2
1.2.2 Generation of Gas Phase Ions by ESI.....	3
1.2.3 Free Jet Expansion in the Ion Source.....	5
1.3 Mass Analyzer.....	6
1.3.1 Time of Flight Mass analyzer.....	6
1.4 Collision-Induced Dissociation.....	7
1.5 Clustering during ESI-MS.....	8
1.5.1 A Unique Case: Clustering of Serine.....	9
1.6 Previous Studies Related to Ser Octamers.....	9
1.6.1 History of Ser Octamer Cluster.....	9
1.6.2 Formation Mechanism of Ser Octamer Cluster.....	10

1.6.3	Structure of the Ser Octamer.....	11
1.7	Homochiral Assembly of Ser Octamers	11
1.8	Computational Methods in Chemistry	14
1.9	Molecular Dynamics Simulations.....	14
1.9.1	Fundamentals of MD	14
1.9.2	MD Force Fields	17
1.9.3	Periodic Boundary Conditions.....	17
1.9.4	Water Models.....	18
1.9.5	Energy Minimization: Preparation for Production Runs	19
1.9.6	Ensembles in MD.....	19
1.9.7	Trajectory Stitching	20
1.9.8	Mobile Proton Molecular Dynamics (MPMD).....	20
1.10	Density Functional Theory	21
1.10.1	Fundamentals of DFT	22
1.10.2	Functionals and Basis Sets.....	23
1.10.3	Single Point Energy Calculations	24
1.10.4	Geometry Optimization	24
1.10.5	Relaxed Scans	25
1.11	Scope of Thesis.....	25
1.12	References.....	27
Chapter 2	36
2	Electrosprayed Serine Octamer Magic Number Clusters: Formation via Gas Phase Assembly and Collision-Induced Dissociation	36
2.1	Introduction.....	36
2.2	Methods.....	41
2.2.1	Mass Spectrometry.....	41

2.2.2	General Computational Procedures	42
2.2.3	Design of Ser Monomers	44
2.2.4	Mobile Proton MD Simulations.....	48
2.3	Results and Discussion	50
2.3.1	Experimental Characterization of Ser Clusters.....	50
2.3.2	Ser Cluster MS/MS.....	52
2.3.3	Evidence for Ser Clustering in the Gas Phase	53
2.3.4	DFT and MD Characterization of the Scutelnic Model.....	55
2.3.5	Solution Phase MD Simulations	56
2.3.6	Simulating Step 1: Ser Clustering in ESI Droplets.....	59
2.3.7	Design of MPMD CID Simulations.....	61
2.3.8	Simulating Step 2: CID of Droplet-Assembled Clusters	62
2.3.9	Simulating Step 3: Ser Cluster Formation in the Gas Phase.....	64
2.3.10	Simulating Step 4: CID of Gas Phase-Assembled Clusters.....	66
2.4	Conclusions.....	68
2.5	References.....	70
Chapter 3	84
3	Summary and Future Work.....	84
3.1	Summary and Conclusion.....	84
3.2	Future Work.....	86
3.2.1	Simulations of L/D mixture of Ser in droplet.....	86
3.3	References.....	88
4	Appendix.....	89
Curriculum Vitae	95

List of Tables

Table 1 E_{DFT} energies (kJ mol^{-1}) of different Ser species from three DFT methods.	47
--	----

List of Figures

- Figure 1.1 Cartoon representation of a typical Q-TOF mass spectrometer. Twisted wave ion guides (TWIG1), ion mobility spectrometry (IMS), time of flight mass detector (TOF). 2
- Figure 1.2 Cartoon illustration of the ESI process, the red circle highlights droplet undergoing fission events. The blue sphere represents a small droplet containing two analyte molecules. 4
- Figure 1.3 Mechanisms for gas phase ion formation from ESI nanodroplets. 5
- Figure 1.4 Mass spectrum of 5 mM Ser in water/HAc 0.1%. $[8]^+$ represents the dominant MNC. 9
- Figure 1.5 Proposed Ser octamer structure³⁸, yellow dashes show hydrogen bonds. Three shared hydrogens are shown as white spheres. The α and β amino acids are colored in orange and green. 11
- Figure 1.6 L-Ser (green) and D-Ser (blue)..... 12
- Figure 1.7 (a) Theoretical binomial distribution for the number of L-Ser in Ser octamers upon electrospraying a racemic Ser mixture, without enantioselectivity. (b) complete chiral separation. Ser octamer experiments reveal a behavior resembling panel (b)..... 13
- Figure 1.8 Nonbonded interactions in MD simulations. a) Coulombic potential and b) Lennard-Jones potential. σ refers to distance between atoms corresponded to zero potential energy and ϵ refers to the minima of potential. r denotes distance between interacting atoms. 16
- Figure 2.1 A) NaCl MNC.²⁹ (B) L-Ser crystal.⁶⁹ (C) H-bonds (dashed lines) in the crystal. (D) $2 \times 2 \times 2$ excision from the Ser crystal. (E) Ser_8H^+ model proposed by Scutelnic et al.⁶¹ Dashed lines are H-bonds. Element coloring: O, red; N, blue; C, green in SEZ and cyan in SEP^+ . H is white, except for three “shared” H that are shown in magenta. Nonpolar hydrogens have been omitted in panel E. 40
- Figure 2.2 Ion path (red) in a Waters Synapt G2 instrument, from ESI source to detector (D).⁷⁷ Pressures (mBar) under trap gas “on” settings are shown in green. Light blue triangles

indicate free jet gas expansion regions. Travelling wave ion guides (TWIGs) are denoted as TWIG1, trap, IMS, and transfer..... 42

Figure 2.3 E_{DFT} data from Table 1, plotted on a relative scale where $E_{\text{DFT}}(\text{SEN})$ was shifted to zero for each DFT method. Shown along the right are B3LYP/6-311+G(d,p) geometry-optimized structures of monomeric Ser species. The red dashed line indicates the SEO rel. E_{DFT} lowered by 50 kJ mol^{-1} , as used for some MPMD simulations. 46

Figure 2.4 DFT relaxed scan of the SEZ \rightarrow SEO transition, yielding geometry-optimized structures and their E_{DFT} values for a range of NH distances r_{NH} . Data shown here were generated using B3LYP/6-311+G(d,p). Similar profiles were obtained with B3LYP/6-31G(d) and M06/6-311+G(d,p) (Appendix 2). 47

Figure 2.5 ESI mass spectra of Ser in water. Trap CV 2 V, trap collision gas off. (A) Sampling cone 5 V. (B) Sampling cone 180 V. The regions $m/z < 300$ and $m/z > 1025$ were rescaled as indicated. $[n]^{z+}$ refers to the main component, n is the number of Ser. Insets show experimental spectra and isotope models. For (A), “[8]²⁺” = $0.32[4]^+ + 0.68[8]^{2+}$ and “[8]⁺” = $0.64[8]^+ + 0.18[16]^{2+} + 0.18[24]^{3+}$. For (B), “[8]²⁺” = $0.61[4]^+ + 0.39[8]^{2+}$ and “[8]⁺” = $0.72[8]^+ + 0.16[16]^{2+} + 0.12[24]^{3+}$ 51

Figure 2.6 MS/MS of Ser clusters. Each column is for one precursor ion. Trap CV values are indicated. Row 1: trap collision gas off. Rows 2-4: trap collision gas on. The cone was set to 5 V for all spectra. Peak annotation is analogous to that of Figure 5. Precursor ions used: (A-D) $841 = \text{Ser}_8\text{H}^+ = [8]^+$, (E-H) $876 = [25]^{3+}$, (I-L) $1297 = [37]^{3+}$, (M-P) $1998 = \text{overlap of } [95]^{5+} \text{ and } [190]^{10+}$ 53

Figure 2.7 (A) The Scutelnic Ser_8H^+ model⁶¹ is displayed in thick sticks. Thin lines illustrate how this structure evolved after five independent 10 ns MD runs in the gas phase at 100 K. Individual Ser are colored differently, the single SeP (cyan) is highlighted. (B) Same as panel A, but for five MD runs at 300 K. (C) MD simulation of the Scutelnic Ser_8H^+ model in bulk water at $t = 0$, and (D) after 10 ns at 300 K. The simulation box also contained one Cl⁻ to ensure charge neutrality. (E) 4 M SEZ in bulk water at $t = 0$, and (F) after 10 ns at 300 K. 58

Figure 2.8 MD simulations of evaporating aqueous ESI nanodroplets. (A-D) Snapshots taken from a typical trajectory. SEZ and SEP are depicted in spacefill representation. (E) Droplet

composition vs. time for the run of panels A-D. (F) Composition of clusters produced in 96 repeat runs for droplet with different initial SEZ numbers. Element coloring is as in Figure 1. 60

Figure 2.9 MPMD simulations of Ser cluster CID. The $t = 0$ clusters for this data were formed in ESI droplets. (A-D) Snapshots from a trajectory where $[\text{SEZ}_{14} \text{SEP}_3]^{3+}$ dissociates into SEP^+ . (E-H) Snapshots from a trajectory where $[\text{SEZ}_{12} \text{SEP}_3]^{3+}$ dissociates into Ser_8H^+ . (I) Cluster composition vs. time for panels A-D. (J) Cluster composition vs. time for panels E-H. (K) Product distribution generated by CID of all 96 clusters..... 64

Figure 2.10 MPMD simulations of Ser clustering in the gas phase. (A-D) Snapshots from a trajectory where one SEP associates with numerous SEO into a cluster. (E) Cluster composition vs. time for panels A-D. (F) Product distribution from 96 runs with different initial SEO numbers. 66

Figure 2.11 MPMD simulations of Ser cluster CID. The $t = 0$ clusters for this data set were generated by gas phase assembly. (A-D) Snapshots from a trajectory where $[\text{SEZ}_{10} + \text{SEP} + \text{SEO}_4]^+$ undergoes stepwise dissociation into Ser_8H^+ . (E) Cluster composition vs. time for panels A-D. (F) Product distribution generated after CID of all 96 clusters. 68

Figure 3.1 Relative abundance vs number of L enantiomers in cluster for Ser_8+H^+ CID products. (a) CID of droplet generated precursors. (b) CID of gas assembled clusters. 87

List of Appendices

Appendix 1 CID of leucine enkephalin (LeuEnk, YGGFL). ¹⁴⁶ (A-D) ESI mass spectra acquired at different cone voltage, with constant trap CV. (E-H) Tandem mass spectra of the [M+H] ⁺ precursor ion (monoisotopic <i>m/z</i> 556.28) acquired at different trap CV, with constant cone voltage. The Ar trap collision gas was on for all the data shown here. Major fragment ions are indicated; identification was performed using UCSF Protein Prospector. Upper case single letters denote immonium ions, double letters represent internal fragments, # indicates unidentified contaminants.	90
Appendix 2 DFT relaxed scans of the SEZ → SEO transition, analogous to Figure 2.2. The data were generated using three different methods: B3LYP/6-31G(d), B3LYP/6-311+G(d,p), and M06/6-311+G(d,p).	91
Appendix 3 DFT-optimized vs. MD-energy minimized Ser monomer structures. Shown along the left are overlays of CHARMM36 (magenta) and OPLS-AA (orange) steepest-descent energy optimized structures, and B3LYP/6-311+G(d,p)-optimized structures (green/red/blue/white). Force field steepest descent calculations used $F \leq 100 \text{ kJ mol}^{-1} \text{ nm}^{-1}$ as convergence criterion. Numbers on the right represent all-atom RMSD values in nm. Average RMSDs are 0.008 nm for CHARMM36, and 0.015 nm for OPLS-AA.	92
Appendix 4 Comparison of the B3LYP/6-31G(d,p) Ser ₃ H ⁺ model by Scutelnic et al. ⁶¹ (with carbon atoms in green and cyan, as in Figure 2.1), and a DFT geometry optimization of this model using B3LYP/6-311+G(d,p) (blue). The RMSD between the two structures is 0.01 nm.	93
Appendix 5 Gas phase MPMD simulations of cluster CID, starting with [SEZ ₁₉ SEP ₅] ⁵⁺ . Temperature profile: 12.5 ns at 600 K, 12.5 ns at 700 K, 425 ns at 950 K. (A) E_{DFT} values as specified in Table 1. CID product = [SEZ ₁₄ SEP] ⁺ . (B) same as panel A, except that $E_{\text{DFT}}(\text{SEO})$ was lowered by 50 kJ mol ⁻¹ . CID product = SEP. Note the rapid loss of SEO immediately after each intramolecular SEZ → SEO proton transfer.	94

List of Symbols and Abbreviations

API	atmospheric pressure ionization
CEM	chain ejection model
CHARMM	Chemistry at Harvard Molecular Mechanics
CID	collision induced dissociation
CRM	charge residue model
DFT	density functional theory
ϵ_0	permittivity of vacuum
ESI	electrospray ionization
GPU	graphics processing unit
IEM	ion evaporation model
LC/MS	liquid chromatography mass spectrometry
m/z	mass-to-charge ratio
MALDI	matrix-assisted laser desorption/ionization
MD	molecular dynamics
MNC	magic number cluster
MPMD	mobile proton molecular dynamics
MS	mass spectrometry
MS/MS	tandem mass spectrometry
OPLS/AA	optimized potential for liquid simulations all atoms
PBC	periodic boundary conditions
PME	Particle Mesh Ewald
SPC	simple point charge model
TIP3P	transferable intermolecular 3-point potential
TIP4P	transferable intermolecular 4-point potential

TOF	time of flight
Q_{Ry}	Rayleigh limit
z	charge state

Chapter 1

1 Introduction

1.1 Mass Spectrometry

Mass spectrometry (MS) is one of the most popular methods for qualitative and quantitative chemical analyses, e.g., in the pharmaceutical industry.¹ This technique measures the mass-to-charge ratio (m/z) of gas-phase ions. A typical mass spectrometer consists of three main parts: ion source, mass analyzer, and ion detector. The latter two are located in a vacuum chamber, whereas the ion source can be at atmospheric pressure (Figure 1.1), or in the vacuum.²

Samples can be introduced into the mass spectrometer and ionized using different methods such as electron ionization (EI) or matrix-assisted laser desorption/ionization (MALDI). For these two ionization techniques, analyte ions are generated in the vacuum of the mass spectrometer. Electrospray ionization (ESI) is one of the most popular techniques which produces gaseous analyte ions at atmospheric pressure directly from solution, e.g., from a syringe pump or a liquid chromatography column. It involves the application of a high voltage to a conductive capillary. In most cases, a positive voltage is applied which results in $[M + zH]^{z+}$ gaseous ions, with M representing the neutral compound.¹

Mass spectrometers can be equipped with various types of mass analyzers. One of these is a quadrupole (Q), which allows for the selection and separation of specific ions, which can then be subjected to further experiments. Time-of-flight (TOF) analyzers are among the most commonly used detectors. Figure 1 shows the layout of a Q-TOF instrument, which combines a quadrupole and a TOF analyzer. Other devices shown in Figure 1D include collision cells for tandem MS (MS/MS) and traveling wave elements for ion mobility spectrometry (IMS). These tools can provide complementary information by inducing ion fragmentation, or by separating ions according to their collision cross section, respectively.³

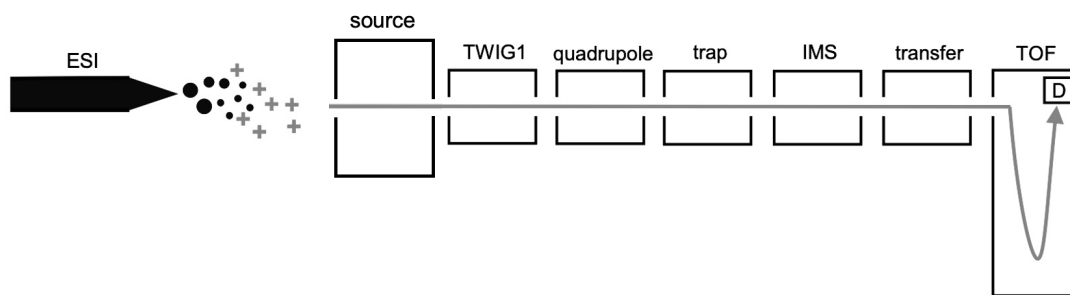


Figure 1.1 Cartoon representation of a typical Q-TOF mass spectrometer. Travelling wave ion guide (TWIG1), ion mobility spectrometry (IMS), and time of flight mass detector (TOF) are shown.

1.2 Ion Source

The ion source ionizes analyte molecules and introduces them to the instrument. Transformation of analytes to ions can be through attachment or removal of protons or electrons, or by attachment of ions such as Na^+ , K^+ , NH_4^+ , acetate, etc. Also, some analytes are intrinsically charged. Ionization techniques can be categorized as “harsh” or “soft”.⁴ Harsh methods such as EI and chemical ionization (CI) cause extensive fragmentation. Examples of soft ionization methods are ESI and MALDI; their defining characteristic is that they largely preserve the analyte covalent structure. Ionization during ESI and MALDI is usually via protonation or deprotonation. The process of ionization can occur inside a vacuum chamber (e.g. fast atom bombardant (FAB), EI, CI, MALDI) or outside a vacuum chamber at atmospheric pressure. The latter is referred as atmospheric pressure ionization (API) such as atmospheric pressure chemical ionization (APCI), and ESI.⁵

1.2.1 Electrospray Ionization

ESI-MS was first implemented by John Fenn in 1984,⁶ who won the 2002 Nobel Prize for this accomplishment.⁷ In the 1980s, ESI was mainly used for the analysis of small organic

molecules. Since then, its application has expanded greatly, all the way to biological complexes.⁸

The capability of ESI to generate gas phase ions directly from analytes in solution enables the combination of MS techniques with solution-phase separations such as liquid chromatography (LC). LC/MS is widely used for numerous applications. While analyte infusion from the outlet of an LC column is quite common, simple syringe pumps can also be used for many applications. A miniaturized version of ESI, “nano” ESI uses very small emitters, usually made from silica coated with gold.⁹

1.2.2 Generation of Gas Phase Ions by ESI

The production of gas-phase ions from analyte solution during ESI represents a continuous process (unlike MALDI, which is inherently pulsed). The ESI source represents an electrochemical cell, with the sample solution being sprayed through a conductive capillary located 1-3 cm away from the mass spectrometer inlet which represents the counter electrode. A high electric potential, V_c , of 2-3 kV is applied to the capillary which usually has an opening of $\sim 100 \mu\text{m}$ in regular ESI and $1 \mu\text{m}$ or less in nanoESI. This voltage causes the solution to be polarized following redox reactions. As a result of voltage application, the solution at the tip changes its shape into a Taylor cone (Figure 1.2). Initial droplets are released from the apex of the Taylor cone. These droplets have radii of $\sim 1 \mu\text{m}$ in ESI and $< 100 \text{ nm}$ in nanoESI. The droplet size also depends on the spray current, solution flow rate, and the nebulizer gas pressure. Typical flow rates in conventional ESI are 5-10 $\mu\text{L}/\text{min}$, or higher in LC/MS. The droplets generated at the tip of the Taylor cone are highly charged due to the presence of excess cations, such as H^+ , NH_4^+ , or Na^+ .¹⁰

In the next step of the ESI process, solvent evaporation causes the charged droplets to shrink and eventually split into smaller, highly charged offspring droplets. Fission events occur because solvent evaporation leads to droplet shrinkage while the droplet charge remains constant. As the droplet size decreases, repulsion between charges within the droplet increases. Once the droplet has shrunk to a certain size, electrostatic repulsion overcomes the cohesive force of surface tension. These conditions result in droplet fission, producing a jet of charged smaller progeny droplets. The stability limit where jet fission

occurs is given by the Rayleigh equation (Equation 1.1). Q_{Ry} is the charge on the droplet, γ the surface tension of the solvent, R the radius of the droplet, and ϵ_0 the vacuum electrical permittivity. Repeated cycles of droplet evaporation and fission eventually produce nanometer-sized droplets (as shown in Figure 1.2).^{11,12}

$$Q_{Ry} = 8\pi(\epsilon_0\gamma R^3)^{\frac{1}{2}} \quad 1.1$$

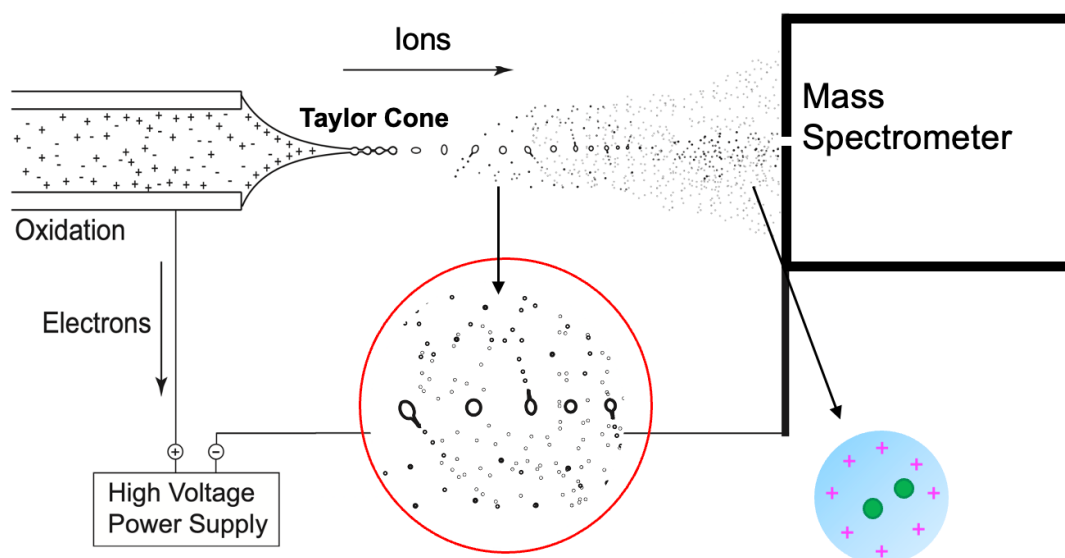


Figure 1.2 Cartoon illustration of the ESI process, the red circle highlights droplet undergoing fission events. The blue sphere represents a small droplet containing two analyte molecules.

Gas-phase ions can be generated by different mechanisms from the final nanodroplets in the ESI plume. Three main mechanisms have been proposed (Figure 1.3). The ion evaporation mechanism (IEM)¹³ describes the electrostatic ejection of ions from the droplet surface. While previously thought to be limited to small ions (such as Na^+), it has since been discovered that larger molecules such as peptides and even proteins can also undergo IEM.¹³ The second process is the charged residue mechanism (CRM) which involves the evaporation of solvent to complete dryness, leaving behind analyte ions in the gas phase.

Lastly, the chain ejection mechanism (CEM) describes the ejection of charged unfolded proteins from the droplet surface.¹¹

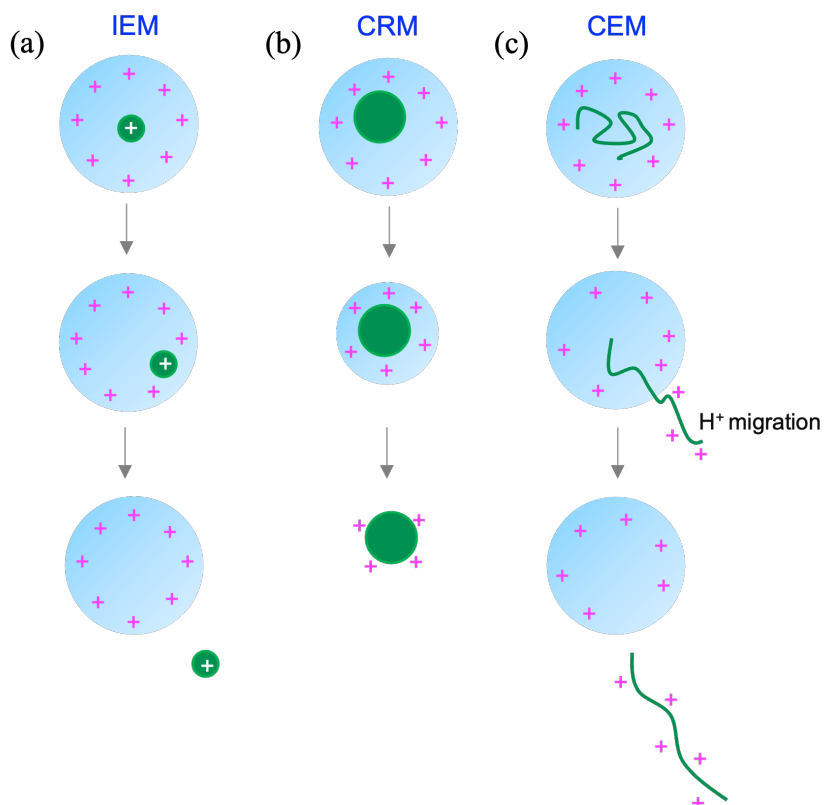


Figure 1.3 Mechanisms for gas phase ion formation from ESI nanodroplets.

1.2.3 Free Jet Expansion in the Ion Source

The principle of free jet expansion involves the rapid expansion of a gas or vapor from a region of high pressure to a region of low pressure, creating a supersonic jet or beam. In the context of an ion source in MS, the substance to be analyzed is infused into the chamber of ion source where the ambient atmosphere provides a relatively high pressure. This chamber is connected to the entrance of mass spectrometry instrument which is under vacuum. When the gas expands from the high-pressure region to the low-pressure region

through a small cone or nozzle, it undergoes an adiabatic expansion known as free jet expansion.⁶

An adiabatic process is characterized by a lack of heat exchange with the surroundings.¹⁴ The expansion considered here is adiabatic because the process occurs very rapidly. Cooling is related to the expansion work performed by the gas, along with the conversion of internal energy into translational kinetic energy. This cooling reduces the thermal motion of molecules, which can lead to the formation of clusters which can be detected and analyzed.^{15,16}

1.3 Mass Analyzer

As stated earlier, the primary purpose of MS is to carry out qualitative and quantitative analyses, such as identifying the molecular or atomic composition of a substance. This is achieved by utilizing a mass analyzer that separates and detects ions according to their m/z . There are several types of mass analyzers available, each operating on unique principles.¹⁷

1.3.1 Time of Flight Mass analyzer

TOF mass analyzers represent one of the oldest techniques. In TOF, ions are accelerated into a vacuum flight tube by an electrical pusher pulse. The flight tube, which measures between one and two meters in length (l), allows ions to travel a certain distance before they hit the detector. The pusher provides all ions of the same z with the same potential energy, which is subsequently converted to kinetic energy, as shown in Equations 1.2. and 1.3.

$$E_{pot} = E_{kin} \quad 1.2$$

$$z e \Delta U = \frac{1}{2} m v^2 \quad 1.3$$

ΔU is the voltage, m is the mass, v is the velocity, and z stands for the charge state of the ion.

The speed of the individual ion is constant, thus flight time can be obtained by

$$t_f = \frac{l}{v} \quad 1.4$$

where t_f is the time the ions require to reach the detector. Equation 1.3 can be rearranged to:

$$v = \sqrt{\frac{2 e z \Delta U}{m}} \quad 1.5$$

Combination of equations 1.4 and 1.5 leads to:

$$t_f = l \sqrt{\frac{m}{2 e z \Delta U}} = \frac{l}{\sqrt{2 e \Delta U}} \sqrt{\frac{m}{z}} \quad 1.6$$

As in seen in equation 1.6, t_f is related to m/z . Lighter ions reach the detector faster than heavier ones, thus enabling the separation of ions based on mass.

To enhance a mass spectrometer's resolution, reflectrons designed in V or W shapes are commonly employed. In the setup of V-shaped or W-shaped reflectrons, ions are pushed towards the reflectron by an electric field. Within the reflectron, the electric field is adjusted so that ions with higher kinetic energy are decelerated more than those with lower kinetic energy. This variance leads to a spatial separation of ions. The specific design of the reflectron ensures that ions with higher kinetic energy traverse a longer path than those with lower kinetic energy. Ultimately, reflectrons ensure that ions with identical m/z reach the detector at the same time.¹⁸ For sensitivity settings, the V-shaped reflectron is used, while the W-shaped configuration provides enhanced resolution.¹⁷

1.4 Collision-Induced Dissociation

After passing through the sampling cone in the ion source, ions may undergo transformations upon entering the declustering region of the mass spectrometer (Figure 1.2). This section provides a free jet environment, as discussed above.¹⁹ When ions enter

this part, they experience an electric field between sample cone and extraction cone that accelerates the ions, triggering collisions with the neutral background gas molecules. These collisions raise the ion temperature resulting in an increase of ion internal energy that promotes the loss of residual solvent molecules and/or collision-induced dissociation (CID). Also, these collisions counter cooling and clustering that the ions might otherwise experience the adiabatically cooled environment of the free jet emanating from the sampling cone. In addition, CID can be implemented further downstream, for example in the trap cell (Figure 1).²⁰

1.5 Clustering during ESI-MS

Electrosprayed ions that are observable in the mass spectrum usually mirror the properties of the corresponding solution species; most peaks represent monomeric ions. However, in some cases, the ESI process produces gas phase clusters from monomeric analytes in solution,^{21,22,23,24}

Magic number clusters (MNCs) are species that have an unusually high abundance. They tend to be characterized by a highly symmetrical shape and high thermodynamic stability. Although these attributes are often cited as the key reason for their high abundance, many aspects of their formation mechanism require further investigation. Considering the cluster formation via ESI, with the short time of this process, it is likely that MNC formation is kinetically controlled. An example of a magic number cluster is $[\text{Na}_{14}\text{Cl}_{13}]^+$. Upon electro spraying aqueous NaCl solution, clustering happens and produces various $[\text{Na}_n\text{Cl}_m]^{(n-m)+}$ species. $[\text{Na}_{14}\text{Cl}_{13}]^+$, with a cubic $3 \times 3 \times 3$ structure represents the dominant MNC under properly optimized conditions.^{25, 26, 27}

ESI-induced clustering is usually attributed to a CRM scenario. Initially, analyte monomers in ESI droplets associate with each other as the solvent evaporates and the analyte concentration increases. One key question is at what point of the process the preferential formation of MNCs occurs. For NaCl clusters, it appears that nascent clusters formed after solvent evaporation to dryness are completely nonspecific (i.e. without preference for

MNCs). Experiments and computational work suggest that MNC-dominated product distributions are formed by “maturation” of these nascent clusters during in-source CID.²³

1.5.1 A Unique Case: Clustering of Serine

Serine (Ser) is a naturally occurring amino acid that has a methyl alcohol side chain. All amino acids can form clusters under suitable conditions in ESI experiments. However, only Ser has been observed to form a specific octameric MNC with a surprisingly high abundance (Figure 1.4). Moreover, this experiment is reproducible and many researchers observed a similar behavior.²⁸

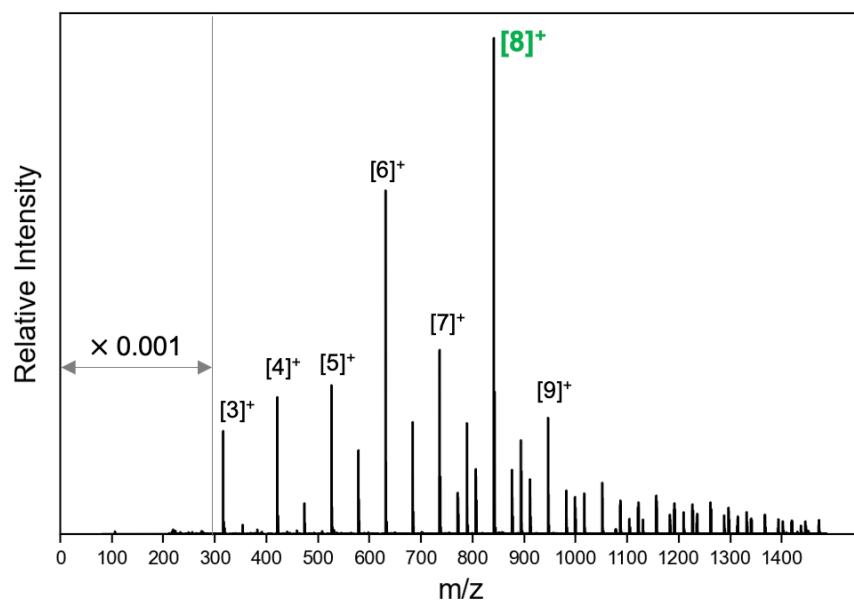


Figure 1.4 Mass spectrum of 5 mM Ser in water/HAc 0.1%. [8]⁺ represents the dominant MNC.

1.6 Previous Studies Related to Ser Octamers

1.6.1 History of Ser Octamer Cluster

The Ser octamer MNC was discovered initially in ESI-MS experiments using a high concentration of Ser (0.01 M). The relation between clusters observed in ESI and solution

aggregates is not clear. The clusters might be product of processes occurring in ESI or mass spectrometer chambers.^{28,29}

Moreover, various other spray ionization techniques have been utilized to investigate Ser clusters. These methods include cold spray ionization (CSI),^{30,31} sonic spray ionization (SSI),^{32,33} and electrosonic spray ionization (ESSI).³⁴ These techniques are considered by some researchers to provide even gentler ("softer") ways of ionization compared to regular ESI. ESSI, in particular, is known for gently producing fully desolvated ions. The relative abundance of protonated Ser octamer in relation to clusters of different sizes changes depending on the experimental conditions.²⁸

Magic number clustering of Ser is not limited to charged species but takes place even for neutral clusters. Other cationic and anionic forms of Ser octamers also show MNC behavior under appropriate experimental conditions.²⁸

1.6.2 Formation Mechanism of Ser Octamer Cluster

The processes governing the formation of Ser octamer clusters remain incompletely understood. One proposed mechanism suggests that a fraction of Ser octamers already pre-exist in bulk solution prior to ESI. The base of this hypothesis is the observation of octamer in the mass spectra even with the smallest tip opening (which ensures there is only one analyte in each ESI droplet). However, the experimental data supporting this hypothesis are inadequately elucidated. In addition, the study did not consider the possibility of octamer formation further downstream during the ESI process.³⁵

An experimental work by Jordan et al.,³⁶ suggested that Ser octamers form during ESI in ion source. Initially, larger non-specific clusters are generated inside of an ESI droplet. Subsequently, these clusters lose their solvent through CRM or IEM and turn into gaseous species. As these clusters pass toward the mass spectrometer, they undergo CID and create octamers as preferred fragmentation products.³⁷ This proposed mechanism is somewhat similar to the formation path of NaCl MNCs published in a study by Konermann et al.²³

1.6.3 Structure of the Ser Octamer

Scutelnic et al.³⁸ investigated the structure of the Ser octamer using ESI-IMS/MS and various computational methods. They claim to introduce a structural model that agrees well with experimental data. In this proposed structure, the amino acids in the cluster are bound together through a strong salt bridge and hydrogen bond network. Two monomers (α and β) have their side chains facing toward the outside of the cluster. Three hydrogens are “shared” between two adjacent functional groups: one is shared between two carboxylates, and the other two are shared between an amine and a carboxylate, Figure 1.5 (coordinates of the structure is adapted from ref)³⁸

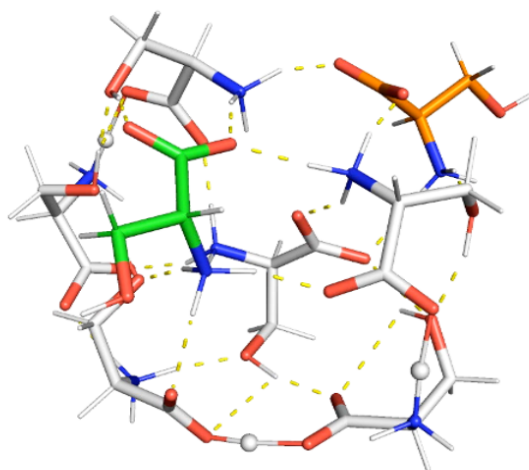


Figure 1.5 Proposed Ser octamer structure³⁸, yellow dashes show hydrogen bonds. Three shared hydrogens are shown as white spheres. The α and β amino acids are colored in orange and green.

1.7 Homochiral Assembly of Ser Octamers

Chiral molecules are spatial isomers that can exist as non-superimposable mirror images.³⁹ All amino acids are chiral molecules with their chiral center on the α -carbon. Almost all of the naturally occurring amino acids are in the L-configuration. Figure 1.6 demonstrates the structures of L-Ser and D-Ser enantiomers.

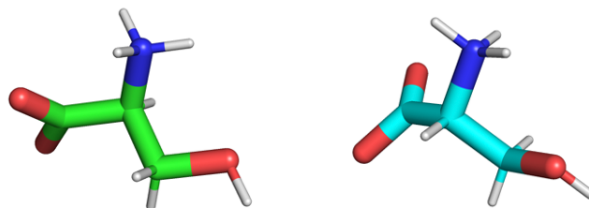


Figure 1.6 L-Ser (green) and D-Ser (blue).

The origin of homochirality (i.e., the dominance of L amino acids) in biology is still being explored. This concept is closely associated with questions related to the origin of life.⁴⁰ One hypothesis envisions the possible involvement of amino acid clusters in sequential chemical reactions. These reactions may eventually led to the emergence of chiral molecules in self-replicating systems.^{41,42} Ser has a particular significance since it is the only amino acid that forms MNCs. Importantly, these MNCs possess a remarkable homochirality, discussed in more detail below. The aforementioned observations led to the hypothesis that Ser MNCs may have played a crucial role in the first chiral selection in nature, ultimately transferring homochirality through chemical reactions to other amino acids, saccharides, and peptides.^{28,43}

If a racemic solution of L and D-Ser is infused into an ESI mass spectrometer, one might expect to see mixed D/L clusters. For a random assembly mechanism, the composition should follow a binomial distribution described by Equation 1.7 and shown in Figure 1.7.⁴⁴ In this equation, P represents the probability, k is the number of times for a specific result within n trials, $\binom{n}{k}$, number of combinations, p is the probability of success on each trial, and q = (1-p). For the case considered here, p = 0.5, n = 8, and k = 0, ..., 8 is the number of L-Ser molecules in the octamer.

$$P(k) = \binom{n}{k} p^k q^{n-k} \quad 1.7$$

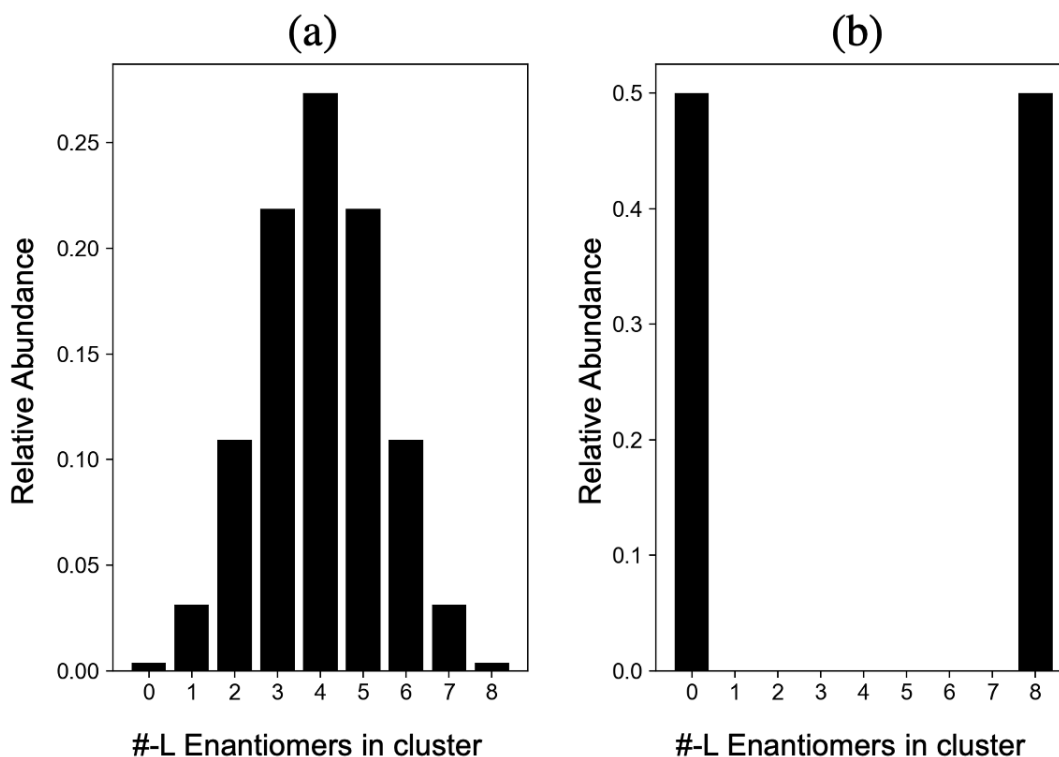


Figure 1.7 (a) Theoretical binomial distribution for the number of L-Ser in Ser octamers upon electrospraying a racemic Ser mixture, without enantioselectivity. (b) complete chiral separation. Ser octamer experiments reveal a behavior resembling panel (b).

Surprisingly, the experimental abundances of L- and D- Ser octamers show an enantiomerically enriched assemble, resembling the distribution shown in Figure 1.7.b).³⁷

For distinguishing between L- and D-Ser in ESI-MS experiments the three non-exchangeable hydrogens (-CH₂ and -CH) in one of the enantiomers are replaced with deuterium while keeping the other enantiomer unchanged. This makes the labeled enantiomer 3 mass units heavier, such that the extent of L (or D) enrichment in the clusters is directly evident from the measured mass spectra.³⁷

1.8 Computational Methods in Chemistry

Computational techniques have significantly advanced research across multiple fields, notably in chemistry, where computer-based simulations present numerous benefits. These approaches facilitate comprehensive analysis from various perspectives, aiding in the evaluation and refinement of experimental data. Moreover, they allow for the simulation of experiments that would otherwise be infeasible or unachievable in practical settings. Computational chemistry constitutes a vast domain including diverse methodologies, derived from quantum or classical mechanics.⁴⁵

Molecular dynamics (MD) simulations represent one of the fundamental techniques that belong to the classical mechanical approaches. The foundation of MD simulations traces back to the late 1950s with the pioneering work of Alder and Wainwright.⁴⁶ Today, MD simulations are extensively used by biochemists due to their relative simplicity and their ability to model large systems such as proteins in a solvent on biologically relevant time scales. The first protein MD runs were conducted in 1977 by McCammon et al.⁴⁷ Since then, the field has advanced considerably. For instance, Shaw et al. in 2009 reported on Anton, a new type of computer that dramatically increased the speed of MD simulations of biological systems by implementing a massively parallel architecture, enabling millisecond-scale simulations previously deemed unattainable. This represents an improvement of two orders of magnitude compared to the previous state of the art.⁴⁸

1.9 Molecular Dynamics Simulations

1.9.1 Fundamentals of MD

In MD simulations, atoms and bonds are considered as simple ball and spring models, and Newton's second law is used to produce a trajectory. There are three main steps to run an MD simulation. First, intermolecular and intramolecular interactions between atoms have to be defined in an MD force field. Second, calculation of atomic positions and velocities as a function of time, i.e., generation of a trajectory. Third, analysis of the trajectory data.⁴⁹

For any MD simulation, two main interaction types must be considered, i.e., bonded and non-bonded interactions. The former are captured via harmonic energy terms that describe bond stretching, angle bending, and torsion angle changes. Non-bonded contributions are van der Waals and electrostatic interactions (Figure 1.8). Equation 1.8 demonstrates the Lennard-Jones potential between pairs.

$$U_{LJ} = 4\epsilon \sum_{i,j} \left(\frac{\sigma}{r_{ij}} \right)^{12} - \left(\frac{\sigma}{r_{ij}} \right)^6 \quad 1.8$$

Here, ϵ refers to the value of minimum energy and σ corresponds to the distance between atoms in which potential energy is zero. The term $\left(\frac{\sigma}{r_{ij}} \right)^{12}$ represents the repulsive part of the potential, which refers to the Pauli exclusion principle, preventing the particles from overlapping. The term $\left(\frac{\sigma}{r_{ij}} \right)^6$ reflects the attractive part of the potential, which arises from van der Waals forces.

Equation 1.9 represents the Coulombic potential

$$U_c = \frac{1}{k_d} \frac{1}{4\pi\epsilon_0} \sum_{i,j} \frac{q_i q_j}{r_{ij}} \quad 1.9$$

in which q_i and q_j are the charges of atoms i and j , ϵ_0 is the vacuum permittivity, k_d dielectric constant e.g., ~ 80 for water at 300 K and r_{ij} is the distance between the atoms.

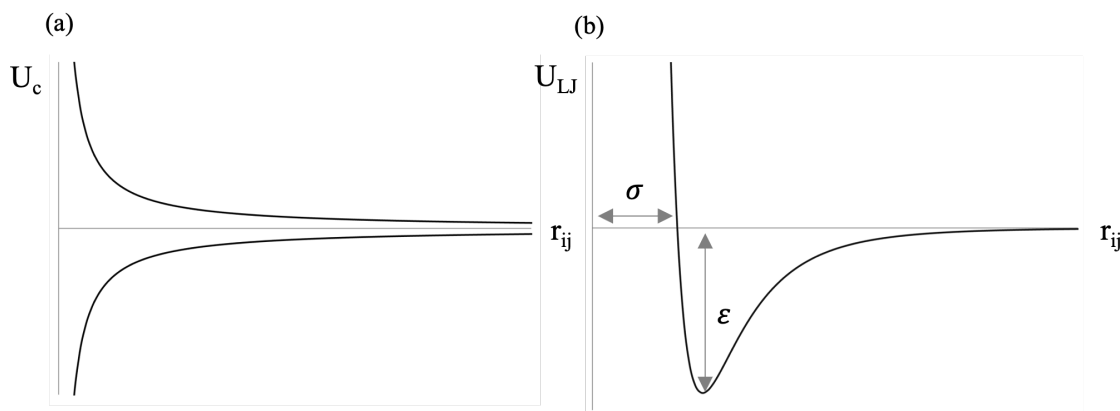


Figure 1.8 Nonbonded interactions in MD simulations. a) Coulombic potential and b) Lennard-Jones potential. σ refers to distance between atoms corresponded to zero potential energy and ϵ refers to the minima of potential. r denotes distance between interacting atoms.

Once the interactions are defined, velocities and positions of each atom can be calculated based on Equations 1.10 and 1.11. In Equation 1.10 (Newton's second law), t represents time, \mathbf{v}_i the velocity, m_i the mass and \mathbf{r}_i the position of each atom. In Equation 1.11, \mathbf{F}_i represents the force acting on atom i , U is the potential energy of the system, and ∇U , indicates the collection of all partial derivatives of U into a vector. Once the forces are known, the differential equation 1.10 can be solved in an iterative fashion. The leap frog algorithm is one of these approaches, and it is the one adopted by the Gromacs software used in this work.⁵⁰

$$\mathbf{F}_i = m_i \mathbf{a}_i = \frac{m_i d\mathbf{v}_i}{dt} = \frac{m_i d^2 \mathbf{r}_i}{dt^2} \quad 1.10$$

$$\mathbf{F}_i = -\nabla U(\mathbf{r}_1, \dots, \mathbf{r}_N) \quad 1.11$$

This Newtonian treatment allows simulations to be run on large systems having thousands of atoms with reasonable computational time.^{51,52, 53}

1.9.2 MD Force Fields

As mentioned, the initial setup for any MD simulation is to define intermolecular and intramolecular interactions between atoms. Essentially, they are sets of equations and parameters that describe how atoms interact with each other, considering factors like bond lengths, angles, dihedral angles, and non-bonded interactions (illustrated in Figure 1.8). These force fields define the potential energy surface over which the atoms and molecules move, thereby influencing the dynamics of the system. The force field's parameters are usually determined from empirical data, quantum mechanical calculations, or fitting to experimental results, such as spectroscopic measurements or structural data from X-ray crystallography.⁵³

Optimized Potential for Liquid Simulations All Atoms (OPLS/AA)⁵⁴, Assisted Model Building with Energy Refinement (AMBER)⁵⁵, and Chemistry at Harvard Molecular Mechanics (CHARMM)⁵⁶ are examples of commonly utilized force fields. These force fields are primarily designed for simulations in bulk solutions. A force field specifically optimized for gas-phase biomolecular systems has yet to be developed.

In the gas phase, parameters like charge distribution around atoms that are exposed on the surface may be different from those in solution environments. While polarizable models are capable of addressing some of these discrepancies, they come at a high computational cost. Fixed-charge force fields developed for solution simulations are also commonly applied in the gas phase.⁵⁷ In particular, force fields such as CHARMM and OPLS/AA have been shown to be effective for modeling biomolecules in both droplet environments and in the gas phase.⁵⁸

1.9.3 Periodic Boundary Conditions

MD simulations in solution commonly utilize periodic boundary conditions (PBCs) to overcome unwanted surface effects. In this approach, the system is enclosed by identical replicas of itself in all directions. Consequently, if a molecule exits one side of the simulation box, it re-enters from the opposite side, allowing for simulations of quasi-infinite bulk systems avoiding surface-related artifacts. To maintain electroneutrality, the

simulation box must be neutralized by introducing electrolyte ions like Na^+ and/or Cl^- into the solvent. Although cubic PBC boxes are the most common, other shapes can help minimize the number of water molecules to reduce computational time.⁵⁹

To apply GPU acceleration on Gromacs in systems with a net charge, a technique known as the "pseudo-PBC" can be utilized. This method avoids the need for cutoffs. This strategy is most useful for nanodroplet and cluster runs. Diving into the specifics, the droplet is positioned at the center of a large PBC box measuring $999.9 \times 999.9 \times 999.9 \text{ nm}^3$, with cutoff values set to be smaller than the dimensions of the box (for instance, 333.3 nm), and Particle Mesh Ewald (PME) summation^{60,61} is disabled. Furthermore, by adopting this approach, interactions among periodic replicas are avoided, simulating conditions akin to a vacuum environment, all while fully employing the capabilities of GPU acceleration.⁶²

1.9.4 Water Models

In MD simulations, water models are mathematical representations used to describe the behavior and interactions of water molecules. These models aim to approximate the complex behavior of real water while keeping computational cost manageable. Water models range from rigid structures to those allowing internal motions, and some even incorporate polarizability. Rigid models like the simple point charge model (SPC) and transferable intermolecular 3-point potential (TIP3P) are widely used due to their computational efficiency. These models feature different interaction sites and assign point charges to each atom, making them suitable for bulk solution simulations. The careful selection of a suitable water model is crucial for accurately simulating biomolecules, particularly when dealing with ESI droplets, where the complexities of their extensive surface area must be properly represented.⁶³

For ESI nanodroplet simulations, a model named transferable intermolecular 4-point potential (TIP4P/2005) is widely used.⁶⁴ This model is non-polarizable and introduces an additional center known as the M site, positioned coplanar with the O and H sites and

located at the bisector of the H–O–H angle. In this model, the charge of the oxygen atom is placed at the M site, resulting in a more precise representation of the electrostatic properties of water. While TIP4P/2005 involves greater computational cost compared to three-site models such as TIP3P or SPC, its ability to reproduce the water surface tension within approximately 1% across a wide temperature range enables direct comparison of simulation results with experiments. Like other MD water models, TIP4P/2005 does not consider the self-dissociation of water molecules into H^+ and OH^- .⁶⁵

1.9.5 Energy Minimization: Preparation for Production Runs

The input for MD simulations is often obtained from protein crystals or NMR structures. These structures may exhibit unfavorable local atomic interactions. Solvent molecules in the simulation box can also lead to clashes between atoms. Therefore, prior to performing MD simulations, it is critical to carry out the steepest descent energy minimization. This process aims to transition the system into a local energy minimum by relaxing unfavorable interactions between non-bonded atoms, which would otherwise result in large repulsive forces. Moreover, energy minimization takes place independently of time.

1.9.6 Ensembles in MD

MD simulations can be conducted under different ensembles. The canonical (NVT) ensemble⁶⁶ maintains the number of atoms (N), volume (V) and temperature (T) constant. Conserving N and V is trivial. Temperature control is usually achieved using thermostat algorithms. Different thermostats can be used, each with varying accuracy and computational simplicity; one common choice is the Nosé-Hoover thermostat.⁶⁷

Under the isothermal-isobaric (NPT) ensemble the number of atoms, temperature and pressure are kept constant, allowing the system size to change. Similar to the NVT ensemble, preserving the number of atoms is trivial. Thermostats are used for temperature maintenance. Pressure control requires the use of a barostat that allows for dynamic rescaling of the system volume.⁵³

1.9.7 Trajectory Stitching

Simulations of evaporating droplets can be used to mimic ESI process. In these runs, a challenge arises from solvent evaporation, which typically cools the system due to the loss of heat (evaporative cooling). Experimentally, this effect is managed by heating the ion source.⁶⁸ However, in MD simulations droplets tend to freeze as they lose kinetic energy, even when using a thermostat. To address this problem, a technique called trajectory stitching can be employed to help maintain stable temperatures throughout the simulation.^{69,70}

The concept of trajectory stitching is that evaporative cooling remains minimal during short simulation periods. Thus, long simulations are divided into shorter segments. After each segment, solvent molecules and charge carriers that have escaped the droplet are removed, and the remaining droplet is repositioned to the center of the simulation box. New velocities for the droplet's atoms, corresponding to the desired temperature, are then assigned from a Maxwell-Boltzmann distribution before continuing the next segment. A significant advantage of trajectory stitching is the increase in the efficiency of runs. Overall simulation time reduces by decreasing the number of atoms in the system over the course of the simulation.⁵³

1.9.8 Mobile Proton Molecular Dynamics (MPMD)

MD is an important tool to model gas phase ions encountered in mass spectrometry experiments. One important feature of these ions is that protons are highly mobile in the gas phase.^{71,72,73} In standard MD simulations, formation and breakage of covalent bonds is not possible.⁷⁴ However, amino acids have titratable sites which can be protonated or deprotonated. Also, in vacuum, dependent on the surrounding species, titratable sites can adapt a different proton configuration.¹⁸ In regular MD, there is no design to allow titratable sites' adaption of the most suitable charge states while practically they can jump from one titratable site to any other.

The first attempts to implement an MD model for consideration of mobile protons in gas phase were conducted by Thachuk et al.⁷⁵ Their study tried to simulate proton hopping

during CID of proteins. Although it was successfully implemented, only (de)protonation of basic sites was considered. Moreover, the force field of that study was a very simplistic coarse-grained model which is more suitable for bulk simulations rather than gas-phase studies.

Konermann et al.^{76,77} subsequently introduced a method for all-atom mobile proton MD (MPMD) simulations. This approach revolves around an energy term referred to as E_{MPMD} that has two contributions representing proton affinity (E_{pa}) and electrostatic energy V_c (Equation 1.13).

$$E_{MPMD} = E_{pa} + V_c \quad 1.13$$

The MPMD algorithm overcomes the limitations of static charges and allows proton hopping among different protonation sites in gas phase. The proton positions in a protein or cluster get shuffled and examined in each time segment to minimize E_{MPMD} .

1.10 Density Functional Theory

Hohenberg, Kohn, and Sham developed a theory that provided a solid foundation for the theoretical work of Thomas, Fermi, Dirac, and Slater.^{78,79} This contribution, made in 1964, is widely recognized as the establishment of modern Density Functional Theory (DFT).

Since then,⁸⁰ DFT has been used for quantitative understanding of molecular properties based on the fundamental laws of quantum mechanics, i.e., the Schrödinger Equation (Equation 1.14)

$$\hat{H}\psi = E\psi \quad 1.14$$

ψ is the wave function of the system's stationary states, and E is the corresponding energy level. The time-independent Schrödinger equation is commonly used in quantum mechanics to find the allowed energy levels of a system and the shape of the wave functions associated with those levels.

In the case of systems with multiple electrons, solving the Schrödinger equation becomes extremely challenging due to several reasons. In this scenario, each particle interacts with every other particle, leading to a highly complex interaction potentials. This complexity makes it difficult to formulate analytical solutions. The number of variables needed to describe the system grows rapidly with the number of particles. For example, a system with three particles in three-dimensional space requires a 9-dimensional solution, and this complexity increases linearly as the number of particles increases.

To simplify the problem, various investigations suggest applying approximations, such as the mean-field approximation or the Hartree-Fock method. However, these approximations may not fully capture the complexities of the system, leading to inaccurate solutions.

1.10.1 Fundamentals of DFT

As mentioned, a main challenge is to solve the many-body Schrödinger equation for a system of interacting electrons. However, directly solving this equation for real systems is computationally infeasible due to the complexity of the electron-electron interaction term.

81

The Kohn-Sham approach, implemented in 1965, is the key concept in DFT. The method introduces equations that simplify the problem of solving Schrödinger equation by introducing a set of auxiliary non-interacting electrons that occupy fictitious one-electron orbitals. These orbitals are determined self-consistently to reproduce the electron density of the real system. Equation 1.15 demonstrates the mathematical expression of Kohn-Sham orbitals

$$\left(-\frac{1}{2}\nabla^2 + V_{KS}\right)\psi_i = \epsilon_i\psi_i \quad 1.15$$

ψ_i are the Kohn-Sham orbitals, and ϵ_i are the corresponding eigenvalues. ∇^2 is the Laplacian operator. V_{KS} is the effective potential (Equation 1.16)

$$V_{KS} = V_{ext} + V_{el} + \frac{\delta E_{XC}}{\delta\rho} \quad 1.16$$

which consists of the external potential V_{ext} acting on the electrons (due to nuclei). V_{el} , Hartree potential representing classical electron-electron repulsion, and an exchange-

correlation energy E_{XC} that encapsulates the errors related to approximations in calculations of kinetic and potential energy. The total Kohn-Sham energy functional is provided in Equation 1.17

$$E(\rho) = T_0[\rho] + \int V_{ext}\rho dr + J[\rho] + E_{XC}[\rho] \quad 1.17$$

where T_0 is the kinetic energy correlated to a system of non-interacting electrons with density ρ . As previously stated, V_{ext} denotes external potential while $J(\rho)$ defines classical electrostatic interaction energy among electrons. $E_{XC}(\rho)$ is the exchange-correlation energy.⁸¹

The efficiency DFT enables researchers to explore larger systems, providing the electronic structure and energy. This enables the prediction of various properties such as molecular geometries, electronic spectra, and reaction energetics.

1.10.2 Functionals and Basis Sets

In each DFT calculation, there are two important variables, functional and basis set which should be treated wisely.⁸² Functionals are mathematical expressions that correlate electron density to various properties such as electronic structure and total energy. Various functionals are available, offering different levels of accuracy. Common functionals include local density approximations (LDA)⁸³, generalized gradient approximations (GGA)⁸⁴, and hybrid functionals. LDA is based on the local density of electrons. GGA includes information about the gradient of the electron density. Hybrid functionals combine Hartree-Fock exchange with the exchange-correlation functional used in standard DFT, providing a more accurate description of certain electronic properties.⁸⁵ B3LYP is a well-established hybrid functional often used in bimolecular studies in gas phase.⁸⁶

A basis set is a series of functions that are used to describe electronic wavefunctions. These basis functions are usually centered on atomic nuclei. With linear combination of basis functions the overall electronic structure can be approximated. Depending on the level of accuracy and complexity various basis sets can be chosen. A larger basis set usually provides a more accurate representation of electronic structure. However, large basis sets are associated with significant computational cost. Examples of basis sets include minimal

basis sets such as STO-3G, split-valence basis sets (e.g., 6-31G), and basis sets with polarization and diffuse functions for a more accurate representation of electron density in certain regions.⁸⁷

Both the functional and basis set choices for a DFT calculation are part of the approximations made. The selection of functional and basis set should be designed for the specific system being investigated and the accuracy required. In many cases, it is a balance between computational efficiency and the required level of detail.

1.10.3 Single Point Energy Calculations

A single point run in DFT refers to a type of calculation where the total energy of a system is computed for fixed atomic coordinates. These calculations are often used as the first step before conducting more complex analyses, such as geometry optimization, reaction path studies, or vibrational frequency calculations.

The input required for single point calculations are the atomic types and positions, the type of functional, and the basis set. The output provides the total energy of the system along with other properties, such as electronic densities and molecular orbitals, depending on the specifics of the calculation.⁸⁸

1.10.4 Geometry Optimization

Geometry optimization is a process aimed at finding the most stable structure of a molecule by minimizing its total energy. The process involves iteratively adjusting the positions of the atoms until the lowest accessible configuration is reached. In this configuration, energy is at a local minimum and the forces acting on the atoms are minimized.

For geometry optimization, an initial guess for the atomic positions has to be provided. This initial geometry can be based on experimental data, theoretical predictions, or randomly generated coordinates. Then, DFT calculations are performed to determine the energy and forces on the atoms. Based on this information, the positions of the atoms are adjusted, and the process is repeated. This loop continues until the changes in energy and

atomic positions fall below predefined thresholds, indicating that the structure is at a local energy minimum.

The optimization can be done using different algorithms, such as the Quasi-Newton method, which is common due to its balance between speed and accuracy. This method uses approximations of the Hessian matrix, which contains second derivatives of the energy with respect to atomic positions, to find the optimal direction and magnitude of atomic displacements. In DFT, the Hessian is often initially approximated and then updated as the optimization progresses. Good initial Hessian guesses can significantly improve the performance and convergence of the optimization.

The process is sensitive to the initial geometry guess, the choice of the DFT functional and basis set, and the optimization parameters. After optimization, it is typical to verify that the final structure corresponds to a real energy minimum, by checking that all the vibrational frequencies are positive.

Geometry optimization is crucial for accurately predicting molecular structures, reaction pathways, and properties of materials in chemistry, materials science, and related fields.^{88, 89}

1.10.5 Relaxed Scans

A relaxed scan in DFT involves optimizing a molecular system while systematically varying one or more fixed internal coordinates, such as bond lengths. This method helps study reaction mechanisms by observing how energy changes as specific structural parameters are altered. Typically, it starts with a fully optimized geometry, then performs a series of optimizations where the chosen parameters are incrementally changed, while the rest of the molecule adapts to these changes.⁸⁸

1.11 Scope of Thesis

The Ser Octamer MNC represents a compelling subject for investigation because of its potential exclusivity for existence in vacuum condition. Despite previous research³⁵⁻³⁸ on

the structural characteristics and formation mechanism of $[\text{Ser}_8\text{H}]^+$, many aspects related to this MNC remain poorly understood. This includes its potential pre-existence in bulk solution, formation mechanism, and the precise location of generation within mass spectrometer. Moreover, the structure of Ser_8H^+ is yet to be fully explored.

Chapter 2 of this thesis employs a blend of computational and experimental strategies, including MD and DFT, combined with MS, and MS/MS to scrutinize the properties of $[\text{Ser}_8\text{H}]^+$. Initially, we examined the likelihood of the MNC pre-existence in bulk solutions, referencing crystal structure data to support discussions. We then investigated other potential formation mechanisms for $[\text{Ser}_8\text{H}]^+$, including assembly in droplets with subsequent CID of the nascent clusters, as well as cluster assembly in gas phase.

1.12 References

1. Overview of Biological Mass Spectrometry. In *Mass Spectrometry in Structural Biology and Biophysics*, 2012; pp 52-88.
2. Richer, J.; Spencer, J.; Baird, M., Identification of Glue Vapors Using Electron Impact and Chemical Ionization Modes in GC–MS. *Journal of Chemical Education* 2006, 83 (8), 1196.
3. Liu, R.; Li, Q.; Smith, L. M., Detection of Large Ions in Time-of-Flight Mass Spectrometry: Effects of Ion Mass and Acceleration Voltage on Microchannel Plate Detector Response. *Journal of the American Society for Mass Spectrometry* 2014, 25 (8), 1374-1383.
4. Bruins, A. P., Mechanistic aspects of electrospray ionization. *Journal of Chromatography A* 1998, 794 (1), 345-357.
5. Peacock, P. M.; Zhang, W.-J.; Trimpin, S., Advances in Ionization for Mass Spectrometry. *Analytical Chemistry* 2017, 89 (1), 372-388.
6. Yamashita, M.; Fenn, J. B., Electrospray ion source. Another variation on the free-jet theme. *The Journal of Physical Chemistry* 1984, 88 (20), 4451-4459.
7. Fenn, J. B., Electrospray Wings for Molecular Elephants (Nobel Lecture). *Angewandte Chemie International Edition* 2003, 42 (33), 3871-3894.
8. Mora, J. F., Electrospray ionization of large multiply charged species proceeds via Dole's charged residue mechanism. *Analytica Chimica Acta* 2000, 406, 93-104.
9. Konermann, L.; Douglas, D. J., Unfolding of proteins monitored by electrospray ionization mass spectrometry: a comparison of positive and negative ion modes. *Journal of the American Society for Mass Spectrometry* 1998, 9 (12), 1248-1254.
10. Duez, Q.; Metwally, H.; Konermann, L., Electrospray Ionization of Polypropylene Glycol: Rayleigh-Charged Droplets, Competing Pathways, and Charge State-Dependent Conformations. *Anal Chem* 2018, 90 (16), 9912-9920.
11. Aliyari, E.; Konermann, L., Formation of Gaseous Peptide Ions from Electrospray Droplets: Competition between the Ion Evaporation Mechanism and Charged Residue Mechanism. *Analytical Chemistry* 2022, 94 (21), 7713-7721.

12. Kebarle, P.; Verkerk, U. H., Electrospray: from ions in solution to ions in the gas phase, what we know now. *Mass Spectrom Rev* 2009, 28 (6), 898-917.
13. Aliyari, E.; Konermann, L., Formation of Gaseous Proteins via the Ion Evaporation Model (IEM) in Electrospray Mass Spectrometry. *Anal Chem* 2020, 92 (15), 10807-10814.
14. Fenn, J. B., Mass spectrometric implications of high-pressure ion sources. *International Journal of Mass Spectrometry* 2000, 200 (1), 459-478.
15. Knuth, E. L., Size correlations for condensation clusters produced in free-jet expansions. *The Journal of Chemical Physics* 1997, 107 (21), 9125-9132.
16. Searcy, J. Q.; Fenn, J. B., Clustering of water on hydrated protons in a supersonic free jet expansion. *The Journal of Chemical Physics* 1974, 61 (12), 5282-5288.
17. El-Aneed, A.; Cohen, A.; Banoub, J., Mass Spectrometry, Review of the Basics: Electrospray, MALDI, and Commonly Used Mass Analyzers. *Applied Spectroscopy Reviews* 2009, 44 (3), 210-230.
18. Guilhaus, M.; Selby, D.; Mlynski, V., Orthogonal acceleration time-of-flight mass spectrometry. *Mass Spectrom Rev* 2000, 19 (2), 65-107.
19. Covey, T. R.; Thomson, B. A.; Schneider, B. B., Atmospheric pressure ion sources. *Mass Spectrom Rev* 2009, 28 (6), 870-97.
20. Gabelica, V.; De Pauw, E., Internal energy and fragmentation of ions produced in electrospray sources. *Mass Spectrom Rev* 2005, 24 (4), 566-87.
21. Li, A.; Luo, Q.; Park, S. J.; Cooks, R. G., Synthesis and catalytic reactions of nanoparticles formed by electrospray ionization of coinage metals. *Angew Chem Int Ed Engl* 2014, 53 (12), 3147-50.
22. Shukla, A.; Bogdanov, B., Lithium formate ion clusters formation during electrospray ionization: Evidence of magic number clusters by mass spectrometry and ab initio calculations. *J Chem Phys* 2015, 142 (6), 064304.
23. Konermann, L.; Haidar, Y., Mechanism of Magic Number NaCl Cluster Formation from Electrosprayed Water Nanodroplets. *Analytical Chemistry* 2022, 94 (47), 16491-16501.
24. Zhang, R.; Khalizov, A.; Wang, L.; Hu, M.; Xu, W., Nucleation and growth of nanoparticles in the atmosphere. *Chem Rev* 2012, 112 (3), 1957-2011.

25. Furuuchi, N.; Shrestha, R. G.; Yamashita, Y.; Hirao, T.; Ariga, K.; Shrestha, L. K., Self-Assembled Fullerene Crystals as Excellent Aromatic Vapor Sensors. *Sensors (Basel)* 2019, 19 (2).
26. Wang, J.; Mbah, C. F.; Przybilla, T.; Apeleo Zubiri, B.; Spiecker, E.; Engel, M.; Vogel, N., Magic number colloidal clusters as minimum free energy structures. *Nature Communications* 2018, 9 (1), 5259.
27. McBride, J. R.; Dukes, A. D.; Schreuder, M. A.; Rosenthal, S. J., On ultrasmall nanocrystals. *Chemical Physics Letters* 2010, 498 (1), 1-9.
28. Nanita, S. C.; Cooks, R. G., Serine Octamers: Cluster Formation, Reactions, and Implications for Biomolecule Homochirality. *Angewandte Chemie International Edition* 2006, 45 (4), 554-569.
29. Cooks, R. G.; Zhang, D.; Koch, K. J.; Gozzo, F. C.; Eberlin, M. N., Chiroselective Self-Directed Octamerization of Serine: Implications for Homochirogenesis. *Analytical Chemistry* 2001, 73 (15), 3646-3655.
30. Kong, X.; Lin, C.; Infusini, G.; Oh, H. B.; Jiang, H.; Breuker, K.; Wu, C. C.; Charkin, O. P.; Chang, H. C.; McLafferty, F. W., Numerous isomers of serine octamer ions characterized by infrared photodissociation spectroscopy. *Chemphyschem* 2009, 10 (15), 2603-6.
31. Sakamoto, S.; Fujita, M.; Kim, K.; Yamaguchi, K., Characterization of Self-Assembling Nano-Sized Structures by Means of Coldspray Ionization Mass Spectrometry. *Tetrahedron* 2000, 56 (7), 955-964.
32. Yamaguchi, K., Cold-spray ionization mass spectrometry: principle and applications. *Journal of Mass Spectrometry* 2003, 38 (5), 473-490.
33. Hirabayashi, A.; Sakairi, M.; Koizumi, H., Sonic Spray Ionization Method for Atmospheric Pressure Ionization Mass Spectrometry. *Analytical Chemistry* 1994, 66 (24), 4557-4559.
34. Hirabayashi, A.; Sakairi, M.; Koizumi, H., Sonic spray mass spectrometry. *Anal Chem* 1995, 67 (17), 2878-82.
35. Takáts, Z.; Wiseman, J. M.; Gologan, B.; Cooks, R. G., Electrosonic spray ionization. A gentle technique for generating folded proteins and protein complexes in the

gas phase and for studying ion-molecule reactions at atmospheric pressure. *Anal Chem* 2004, 76 (14), 4050-8.

36. Jordan, J. S.; Williams, E. R., Effects of Electrospray Droplet Size on Analyte Aggregation: Evidence for Serine Octamer in Solution. *Analytical Chemistry* 2021, 93 (3), 1725-1731.

37. Jordan, J. S.; Williams, E. R., Dissociation of large gaseous serine clusters produces abundant protonated serine octamer. *Analyst* 2021, 146 (8), 2617-2625.

38. Jordan, J. S.; Williams, E. R., Homochiral preference of serine octamer in solution and formed by dissociation of large gaseous clusters. *Analyst* 2021, 146 (22), 6822-6830.

39. Scutelnic, V.; Perez, M. A. S.; Marianski, M.; Warnke, S.; Gregor, A.; Rothlisberger, U.; Bowers, M. T.; Baldauf, C.; von Helden, G.; Rizzo, T. R.; Seo, J., The Structure of the Protonated Serine Octamer. *J Am Chem Soc* 2018, 140 (24), 7554-7560.

40. Quack, M., Structure and Dynamics of Chiral Molecules. *Angewandte Chemie International Edition in English* 1989, 28 (5), 571-586.

41. Gal, J., The discovery of biological enantioselectivity: Louis Pasteur and the fermentation of tartaric acid, 1857—A review and analysis 150 yr later. *Chirality* 2008, 20 (1), 5-19.

42. Lunine, J. I., The occurrence of Jovian planets and the habitability of planetary systems. *Proceedings of the National Academy of Sciences* 2001, 98 (3), 809-814.

43. Liu, S.; Ren, H.; Gao, Q.; Roach, D. J.; Loder, R. T.; Armstrong, T. M.; Mao, Q.; Blaga, I.; Barker, D. L.; Jovanovich, S. B., Automated parallel DNA sequencing on multiple channel microchips. *Proceedings of the National Academy of Sciences* 2000, 97 (10), 5369-5374.

44. Crisma, M.; Deschamps, J. R.; George, C.; Flippen-Anderson, J. L.; Kaptein, B.; Broxterman, Q. B.; Moretto, A.; Oancea, S.; Jost, M.; Formaggio, F.; Toniolo, C., A topographically and conformationally constrained, spin-labeled, alpha-amino acid: crystallographic characterization in peptides. *J Pept Res* 2005, 65 (6), 564-79.

45. Fujii, N.; Saito, T., Homochirality and life. *The Chemical Record* 2004, 4 (5), 267-278.

46. Tetko, I. V.; Gasteiger, J.; Todeschini, R.; Mauri, A.; Livingstone, D.; Ertl, P.; Palyulin, V. A.; Radchenko, E. V.; Zefirov, N. S.; Makarenko, A. S.; Tanchuk, V. Y.;

Prokopenko, V. V., Virtual Computational Chemistry Laboratory – Design and Description. *Journal of Computer-Aided Molecular Design* 2005, 19 (6), 453-463.

47. Alder, B. J.; Wainwright, T. E., Studies in Molecular Dynamics. I. General Method. *The Journal of Chemical Physics* 1959, 31 (2), 459-466.

48. McCammon, J. A.; Gelin, B. R.; Karplus, M., Dynamics of folded proteins. *Nature* 1977, 267 (5612), 585-90.

49. Shaw, D. E.; Dror, R. O.; Salmon, J. K.; Grossman, J. P.; Mackenzie, K. M.; Bank, J. A.; Young, C.; Deneroff, M. M.; Batson, B.; Bowers, K. J.; Chow, E.; Eastwood, M. P.; Ierardi, D. J.; Klepeis, J. L.; Kuskin, J. S.; Larson, R. H.; Lindorff-Larsen, K.; Maragakis, P.; Moraes, M. A.; Piana, S.; Shan, Y.; Towles, B., Millisecond-scale molecular dynamics simulations on Anton. In *Proceedings of the Conference on High Performance Computing Networking, Storage and Analysis, Association for Computing Machinery: Portland, Oregon, 2009*; p Article 65.

50. Lindahl, E., Molecular dynamics simulations. *Methods Mol Biol* 2015, 1215, 3-26.

51. Van Der Spoel, D.; Lindahl, E.; Hess, B.; Groenhof, G.; Mark, A. E.; Berendsen, H. J., GROMACS: fast, flexible, and free. *J Comput Chem* 2005, 26 (16), 1701-18.

52. Frenkel, D.; Smit, B., *Understanding molecular simulation: from algorithms to applications*. Elsevier: 2023.

53. Hansson, T.; Oostenbrink, C.; van Gunsteren, W., Molecular dynamics simulations. *Current Opinion in Structural Biology* 2002, 12 (2), 190-196.

54. Konermann, L.; Metwally, H.; McAllister, R. G.; Popa, V., How to run molecular dynamics simulations on electrospray droplets and gas phase proteins: Basic guidelines and selected applications. *Methods* 2018, 144, 104-112.

55. Kaminski, G. A.; Friesner, R. A.; Tirado-Rives, J.; Jorgensen, W. L., Evaluation and Reparametrization of the OPLS-AA Force Field for Proteins via Comparison with Accurate Quantum Chemical Calculations on Peptides. *The Journal of Physical Chemistry B* 2001, 105 (28), 6474-6487.

56. MacKerell, A. D.; Bashford, D.; Bellott, M.; Dunbrack, R. L.; Evanseck, J. D.; Field, M. J.; Fischer, S.; Gao, J.; Guo, H.; Ha, S.; Joseph-McCarthy, D.; Kuchnir, L.; Kuczera, K.; Lau, F. T.; Mattos, C.; Michnick, S.; Ngo, T.; Nguyen, D. T.; Prodhom, B.; Reiher, W. E.; Roux, B.; Schlenkrich, M.; Smith, J. C.; Stote, R.; Straub, J.;

- Watanabe, M.; Wiórkiewicz-Kuczera, J.; Yin, D.; Karplus, M., All-atom empirical potential for molecular modeling and dynamics studies of proteins. *J Phys Chem B* 1998, 102 (18), 3586-616.
57. Huang, J.; MacKerell Jr, A. D., CHARMM36 all-atom additive protein force field: Validation based on comparison to NMR data. *Journal of Computational Chemistry* 2013, 34 (25), 2135-2145.
58. Best, R. B.; Hummer, G., Optimized Molecular Dynamics Force Fields Applied to the Helix–Coil Transition of Polypeptides. *The Journal of Physical Chemistry B* 2009, 113 (26), 9004-9015.
59. Lee, J. H.; Pollert, K.; Konermann, L., Testing the Robustness of Solution Force Fields for MD Simulations on Gaseous Protein Ions. *The Journal of Physical Chemistry B* 2019, 123 (31), 6705-6715.
60. Kukul, A., *Molecular modeling of proteins*. Springer: 2008; Vol. 443.
61. Darden, T.; York, D.; Pedersen, L., Particle mesh Ewald: An $N \cdot \log(N)$ method for Ewald sums in large systems. *The Journal of Chemical Physics* 1993, 98 (12), 10089-10092.
62. Essmann, U.; Perera, L.; Berkowitz, M. L.; Darden, T.; Lee, H.; Pedersen, L. G., A smooth particle mesh Ewald method. *The Journal of Chemical Physics* 1995, 103 (19), 8577-8593.
63. Abraham, M. J.; Murtola, T.; Schulz, R.; Páll, S.; Smith, J. C.; Hess, B.; Lindahl, E., GROMACS: High performance molecular simulations through multi-level parallelism from laptops to supercomputers. *SoftwareX* 2015, 1-2, 19-25.
64. Jorgensen, W. L.; Jenson, C., Temperature dependence of TIP3P, SPC, and TIP4P water from NPT Monte Carlo simulations: Seeking temperatures of maximum density. *Journal of Computational Chemistry* 1998, 19 (10), 1179-1186.
65. Abascal, J. L. F.; Vega, C., A general purpose model for the condensed phases of water: TIP4P/2005. *The Journal of Chemical Physics* 2005, 123 (23).
66. Vega, C.; de Miguel, E., Surface tension of the most popular models of water by using the test-area simulation method. *J Chem Phys* 2007, 126 (15), 154707.
67. Jorgensen, W. L.; Tirado-Rives, J., The OPLS [optimized potentials for liquid simulations] potential functions for proteins, energy minimizations for crystals of cyclic

peptides and crambin. *Journal of the American Chemical Society* 1988, 110 (6), 1657-1666.

68. Hoover, W. G., Canonical dynamics: Equilibrium phase-space distributions. *Physical Review A* 1985, 31 (3), 1695-1697.

69. Braga, C.; Travis, K. P., A configurational temperature Nosé-Hoover thermostat. *The Journal of Chemical Physics* 2005, 123 (13), 134101.

70. McAllister, R. G.; Metwally, H.; Sun, Y.; Konermann, L., Release of Native-like Gaseous Proteins from Electrospray Droplets via the Charged Residue Mechanism: Insights from Molecular Dynamics Simulations. *Journal of the American Chemical Society* 2015, 137 (39), 12667-12676.

71. Andersen, H. C., Molecular dynamics simulations at constant pressure and/or temperature. *The Journal of Chemical Physics* 1980, 72 (4), 2384-2393.

72. Steinberg, M. Z.; Breuker, K.; Elber, R.; Gerber, R. B., The dynamics of water evaporation from partially solvated cytochrome c in the gas phase. *Physical Chemistry Chemical Physics* 2007, 9 (33), 4690-4697.

73. Allen, S. J.; Schwartz, A. M.; Bush, M. F., Effects of polarity on the structures and charge states of native-like proteins and protein complexes in the gas phase. *Anal Chem* 2013, 85 (24), 12055-61.

74. Ahadi, E.; Konermann, L., Ejection of Solvated Ions from Electrosprayed Methanol/Water Nanodroplets Studied by Molecular Dynamics Simulations. *Journal of the American Chemical Society* 2011, 133 (24), 9354-9363.

75. Tang, L.; Kebarle, P., Dependence of ion intensity in electrospray mass spectrometry on the concentration of the analytes in the electrosprayed solution. *Analytical chemistry* 1993, 65 (24), 3654-3668.

76. Wyttenbach, T.; Bowers, M. T., Structural stability from solution to the gas phase: native solution structure of ubiquitin survives analysis in a solvent-free ion mobility-mass spectrometry environment. *J Phys Chem B* 2011, 115 (42), 12266-75.

77. Fegan, S. K.; Thachuk, M., A Charge Moving Algorithm for Molecular Dynamics Simulations of Gas-Phase Proteins. *J Chem Theory Comput* 2013, 9 (6), 2531-9.

78. Konermann, L., Molecular Dynamics Simulations on Gas-Phase Proteins with Mobile Protons: Inclusion of All-Atom Charge Solvation. *J Phys Chem B* 2017, 121 (34), 8102-8112.
79. Popa, V.; Trecroce, D. A.; McAllister, R. G.; Konermann, L., Collision-Induced Dissociation of Electrosprayed Protein Complexes: An All-Atom Molecular Dynamics Model with Mobile Protons. *The Journal of Physical Chemistry B* 2016, 120 (23), 5114-5124.
80. Hohenberg, P.; Kohn, W., Inhomogeneous Electron Gas. *Physical Review* 1964, 136 (3B), B864-B871.
81. Kohn, W.; Sham, L. J., Self-Consistent Equations Including Exchange and Correlation Effects. *Physical Review* 1965, 140 (4A), A1133-A1138.
82. Napiórkowska, E.; Milcarz, K.; Szeleszczuk, Ł., Review of Applications of Density Functional Theory (DFT) Quantum Mechanical Calculations to Study the High-Pressure Polymorphs of Organic Crystalline Materials. *Int J Mol Sci* 2023, 24 (18).
83. Becke, A. D., Perspective: Fifty years of density-functional theory in chemical physics. *The Journal of Chemical Physics* 2014, 140 (18).
84. Jones, R. O., Density functional theory: Its origins, rise to prominence, and future. *Reviews of Modern Physics* 2015, 87, 897-923.
85. Sahni, V.; Bohnen, K. P.; Harbola, M. K., Analysis of the local-density approximation of density-functional theory. *Physical Review A* 1988, 37 (6), 1895-1907.
86. Perdew, J. P.; Burke, K.; Ernzerhof, M., Generalized Gradient Approximation Made Simple. *Physical Review Letters* 1996, 77 (18), 3865-3868.
87. Becke, A. D., A new mixing of Hartree–Fock and local density-functional theories. *The Journal of chemical physics* 1993, 98 (2), 1372-1377.
88. Becke, A. D., Density-functional thermochemistry. III. The role of exact exchange. *Journal of Chemical Physics* 1993, 98, 5648-5652.
89. Huzinaga, S., Basis sets for molecular calculations. *Computer Physics Reports* 1985, 2 (6), 281-339.
90. Jensen, F., *Introduction to computational chemistry*. John Wiley & Sons: 2017.

91. Mohr, S.; Ratcliff, L. E.; Genovese, L.; Caliste, D.; Boulanger, P.; Goedecker, S.; Deutsch, T., Accurate and efficient linear scaling DFT calculations with universal applicability. *Physical Chemistry Chemical Physics* 2015, 17 (47), 31360-31370.

Chapter 2

2 Electro sprayed Serine Octamer Magic Number Clusters: Formation via Gas Phase Assembly and Collision-Induced Dissociation

2.1 Introduction

Electrospray ionization (ESI) converts solution phase analytes to gaseous ions that can be studied by mass spectrometry (MS). During ESI, analyte solution is dispersed into charged droplets that undergo solvent evaporation and Coulomb fission, culminating in nanodroplets from which gaseous analyte ions are released.¹ These ions then pass through an ion sampling interface into the vacuum of the mass analyzer.²

Although ESI mass spectra are usually dominated by ions that represent pre-existing solution species, the ESI process can also trigger the self-assembly of clusters. Such clustering has been reported for various analytes including salts, sugars, proteins, and amino acids.³⁻²³ Clustering is generally attributed to events taking place within ESI droplets, where solvent evaporation results in high concentrations that promote the association of solutes. Most ESI-generated clusters exhibit a wide range of nonspecific stoichiometries.^{11-13, 15-18, 24-27} The clusters are released into the gas phase upon solvent evaporation to dryness (charged residue mechanism, CRM),^{4, 6, 27-29} or they may be ejected from the droplet surface (ion evaporation mechanism, IEM).^{5, 22, 30}

ESI of some analytes produces magic number clusters (MNCs), i.e., species that have a much higher abundance than other stoichiometries.^{3, 9, 10, 29, 31-39} These MNCs defy the aforementioned trend toward nonspecificity of ESI clusters.^{11-13, 15-18, 24-27} Many MNCs possess closed shell structures without defects, providing high thermodynamic stability.⁴⁰⁻

⁴⁶ However, stability alone does not explain why MNCs are favored, as many self-assembly processes yield kinetically trapped species instead of thermodynamically stable products. ⁴⁷⁻⁵¹ It has been proposed that MNCs assemble in shrinking ESI droplets. ^{52, 53} However, it is difficult to envision how droplets that contain a stochastic number of analyte molecules^{1, 27} can produce specific stoichiometries. In bulk solution, clustering continues as long as free building blocks are available, ⁵⁴ i.e., self-assembly does not stop once MNCs have formed. ^{54, 55} Therefore, MNC accumulation in evaporating droplets appears unlikely.

ESI-mediated MNC formation is relatively well understood for NaCl solutions, which form MNCs including $\text{Na}_{14}\text{Cl}_{13}^+$ (Figure 2.1A). ^{3-10, 38} Recent molecular dynamics (MD) simulations²⁹ revealed that these MNCs are produced via a two-stage process, where droplet evaporation to dryness generates large nonspecific CRM clusters. Collisional heating of these initial clusters in the ion sampling interface produces highly dynamic structures, where a MNC core is decorated with stringlike protrusions made up of excess Na^+ and Cl^- . Facile dissociation of these protrusions liberates the MNC. ²⁹ It is unclear whether similar scenarios apply to other ESI-generated MNCs.

One of the most enigmatic MNCs is the serine octamer. ^{23, 30, 32, 52, 53, 56-65} Positive ion ESI of Ser solutions yields an unusually high abundance of Ser_8H^+ . Formation of this MNC was also observed after sublimation of solid Ser, ⁶⁶ while negative ion ESI generates $[\text{Ser}_8+2\text{Cl}]^{2-}$ and $[\text{Ser}_8+2\text{Br}]^{2-}$ MNCs. ^{65, 67} Neutral Ser_8 has been detected in nebulization experiments. ⁶² One feature that makes these octamers particularly interesting is their homochiral preference, where racemic mixtures segregate into L- Ser_8H^+ and D- Ser_8H^+ .^{23,}

The structure and formation mechanism of Ser_8H^+ continue to be controversial.^{23, 30, 32, 52, 53, 56-65, 67} MNCs often have compact, symmetrical low-energy motifs packed analogously to bulk crystals,⁴⁰⁻⁴⁶ exemplified by the $\text{Na}_{14}\text{Cl}_{13}^+$ MNC (Figure 2.1A).^{3, 9, 10, 29, 38, 39, 68} The situation for Ser_8H^+ is not as straightforward. L-Ser forms monoclinic crystals (Figure 2.1B) consisting of zwitterionic Ser (SEZ).⁶⁹ The $^+\text{H}_3\text{N-R}$ and R-COO^- groups of SEZ form H-bond-reinforced salt bridges. Sidechain hydroxyls are H-bonded as well, such that all donor/acceptor capabilities are saturated (Figure 2.1B, C).^{69, 70} These crystals provide no clues as to why Ser_8H^+ is a MNC. Unlike for NaCl, Ser crystal sub-structures do not represent viable clusters. For example, excision of a $2 \times 2 \times 2$ cube generates a poor constellation with exposed $^+\text{H}_3\text{N-}$ and $-\text{COO}^-$ groups (Figure 2.1C). Conflicting ring, cubic, and other Ser_8H^+ structures have been proposed. The only consensus in those studies is that Ser_8H^+ consists of seven SEZ and one positively charged Ser (SEP^+).^{32, 53, 56, 57, 60, 61}

Using ion mobility spectrometry (IMS), IR spectroscopy, and density functional theory (DFT), Scutelnic et al.⁶¹ proposed the Ser_8H^+ model in Figure 2.1D (we focus on the “B” form which is closest to the measured 191 \AA^2 collision cross section).⁶¹ While this structure does not have any discernible symmetry, it is extensively linked by salt bridges and H-bonds. Three hydrogens are “shared”, i.e., the corresponding donor-H \cdots acceptor pairs have slightly elongated donor-H bonds (from 0.1 to 0.11-0.12 nm) while the H \cdots acceptor contacts are shortened (from 0.16-0.19 to 0.14-0.15 nm). The Scutelnic model⁶¹ constitutes a significant advance, but its generality remains under debate because IR and deuteration data demonstrated that Ser_8H^+ exhibits considerable heterogeneity, pointing to the existence of alternative structures.^{60, 71, 72}

In addition to the question of Ser_8H^+ structure, it remains unclear where and how during ESI this MNC forms. Scutelnic et al.⁶¹ did not address the Ser_8H^+ formation mechanism; their work screened a large number of candidates to identify the lowest energy structure that provided a reasonable match with IR and IMS data. Proposals that Ser_8H^+ already exists in bulk solution^{32, 52, 65} are at odds with NMR and IR experiments on bulk samples that only detected monomeric Ser.^{73, 74} Other studies suggested that Ser_8H^+ forms in shrinking ESI droplets,^{30, 53, 59, 63} even though such a mechanism would likely favor nonspecific stoichiometries as discussed above. Ser_8H^+ can form in MS/MS experiments during the collision-induced dissociation (CID) of larger clusters,⁶³ but it is unclear to what extent this pathway generates Ser_8H^+ under regular ESI conditions.

Here we used a combination of ESI-MS, mobile-proton MD (MPMD) simulations, and DFT to probe the mechanism of ESI-induced Ser_8H^+ formation. Our data reveal that initial Ser clusters formed in shrinking ESI droplets are extremely labile and undergo CID in the ion sampling interface. Ser monomers released during these dissociation events undergo low-temperature recluster during free jet expansion. Subsequent CID events culminate in Ser_8H^+ -dominated mass spectra.

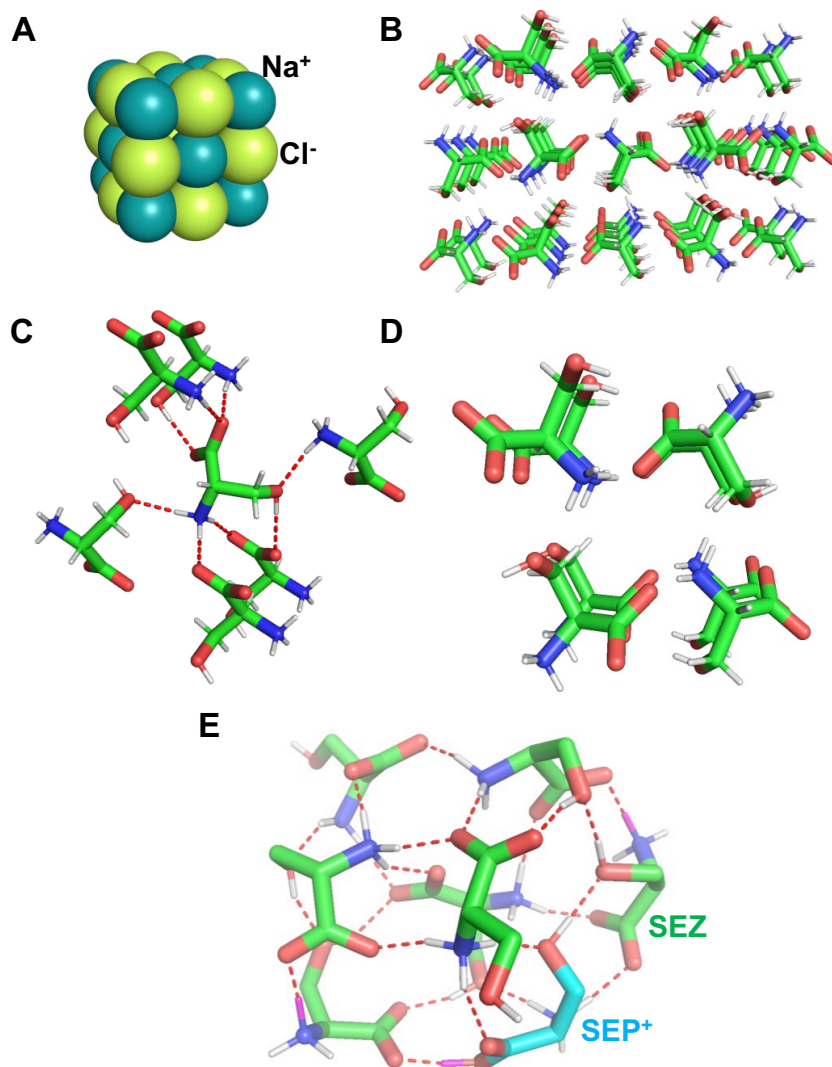


Figure 2.1 A) NaCl MNC.²⁹ (B) L-Ser crystal.⁶⁹ (C) H-bonds (dashed lines) in the crystal. (D) $2 \times 2 \times 2$ excision from the Ser crystal. (E) Ser₈H⁺ model proposed by Scutelnic et al.⁶¹ Dashed lines are H-bonds. Element coloring: O, red; N, blue; C, green in SEZ and cyan in SEP⁺. H is white, except for three “shared” H that are shown in magenta. Nonpolar hydrogens have been omitted in panel E.

2.2 Methods

2.2.1 Mass Spectrometry

Mass spectra were acquired on a SYNAPT G2 quadrupole time-of-flight (Q-TOF) instrument (Waters, Milford, MA, Figure 2.2). 5 mM Ser in water with 0.1% acetic acid was infused into the ESI source at $5 \mu\text{L min}^{-1}$, with the ESI capillary set to +2.8 kV. N_2 served as desolvation and cone gas. The desolvation and source temperatures were 30 and 70 °C, respectively. Collisional activation in the source was controlled by adjusting the sampling cone voltage between 5 V and 180 V (DC difference between sampling and extraction cones). The light blue triangles in Figure 2.2 indicate free jets where the background N_2 gas undergoes adiabatic cooling.⁷⁵ Cooling of analyte ions in the sampling cone jet is counteracted by the sampling cone voltage which accelerates the ions relative to the background gas, resulting in collisional activation.^{2, 75} Collisional activation in the subsequent extraction cone jet is minimal, as the extraction cone voltage was fixed at 3 V (DC difference between extraction cone and TWIG1). The trap gas was switched off for some experiments; in all other cases the trap was filled with Ar collision gas. MS/MS precursor ions were selected in the quadrupole, prior to CID in the trap. The trap collision voltage (CV) was set between 2 and 185 V (DC difference between TWIG1 exit and trap exit)⁷⁶, and the transfer collision voltage was zero.

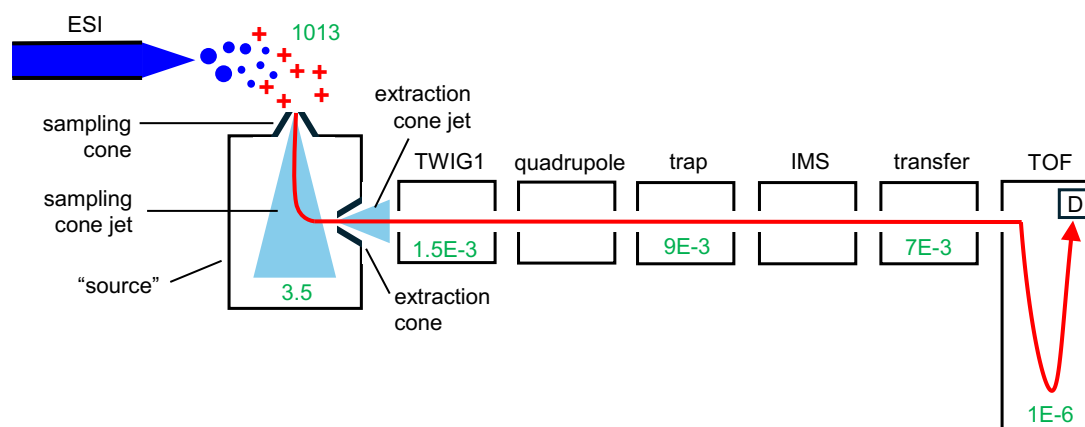


Figure 2.2 Ion path (red) in a Waters Synapt G2 instrument, from ESI source to detector (D).⁷⁷ Pressures (mBar) under trap gas “on” settings are shown in green. Light blue triangles indicate free jet gas expansion regions. Travelling wave ion guides (TWIGs) are denoted as TWIG1, trap, IMS, and transfer.

2.2.2 General Computational Procedures

All data related to the Scutelnic Ser₈H⁺ model⁶¹ employed a structure assembled from eight L-Ser, as this is the biologically dominant Ser enantiomer. The published structure⁶¹ consists of eight D-Ser [D-SEZ₇ + D-SEP]⁺. L-Ser₈H⁺ coordinates were generated from the published data using the Gromacs *editconf* command with option `-scale -1 1 1`.

Gaussian 09⁷⁸ was used for density functional theory (DFT) calculations. The B3LYP functional⁷⁹ was employed with the 6-31G(d) and 6-311+G(d,p) basis sets. We also performed calculations at the M06/6-311+G(d,p) level.⁸⁰ DFT yielded geometry-optimized structures and their energies (E_{DFT} , often referred to as “total” energy), which includes nuclear repulsion, nuclear-electronic attraction, and kinetic plus potential electronic energy.

MD simulations were carried out using GROMACS 2020.4.⁸¹ Most simulations employed the CHARMM36 force field⁸² which is widely used for modeling biomolecular dynamics in solution⁸³ and *in vacuo*.⁸⁴⁻⁸⁶ In addition, we performed gas phase MD using OPLS-AA force field⁸⁷ which is another commonly used choice for gas phase applications.⁸⁸⁻⁹³

Bulk solution simulation followed standard procedures,⁹⁴ employing periodic boundary conditions (PBCs) in a (3 nm)³ cubic box with particle mesh Ewald summation, LINCS-constrained hydrogen-heavy atom bonds, a modified Berendsen thermostat, a 2 fs integration step, and TIP3P water. After steepest descent energy minimization, the bulk systems were equilibrated under *NVT* and *NPT* conditions for 100 ps each, followed by 10 ns *NPT* production runs.

ESI droplet simulations were performed similar to previous work,²⁹ using TIP4P/2005 water. A pseudo-PBC approach was employed that is equivalent to vacuum boundary conditions without cutoffs for nonbonded interactions. Bond constraints and integration step were the same as for bulk simulations, with temperature control by the Nosé-Hoover thermostat. In accordance with experiments, the initial droplet charge was chosen to be at the Rayleigh limit,^{1, 95, 96} where the number of excess elementary charges (e) is $z_R = 8\pi/e \times (\epsilon_0 \gamma r^3)^{1/2}$. For a droplet radius $r = 2.5$ nm and the surface tension $\gamma = 0.05891$ N m⁻¹, $z_R = 14+$. This net charge was implemented by placing 14 SEP⁺ in random positions within the droplet. The SEP_{up} conformer (defined below) was chosen for this purpose because of its presence in the Scutelnic Ser₃H⁺ model,⁶¹ although C-C bond rotation in our MD runs rapidly erased any memory of the initial -COOH orientation. In addition, 5 to 20 SEZ were inserted into the droplet as well, with six replicates for each initial droplet composition.

Following steepest descent energy minimization, droplets were equilibrated for 1 ns during which the temperature was raised from 10 K to 370 K. The droplets were then kept at 370 K for 25 ns, followed by 5 ns at 450 K for removal of residual solvent. Trajectory stitching was used to remove evaporated moieties from the simulations in 0.25 ns intervals.

MD studies of Ser clusters in the gas phase followed procedures similar to those outlined above for ESI droplet (pseudo-PBC with trajectory stitching in 0.25 ns intervals). However, Ser clusters were modeled without bond constraints which required shortening of the integration step to 0.5 fs. Gas phase cluster assembly was simulated at 100 K for 10 ns. Like previous studies,^{29, 86, 97} a thermostat was used to control the cluster temperature instead of explicitly modeling a collision gas. CID simulations covered a 150 ns window (0.5 ns of initial equilibration with a 10 to 700 K temperature ramp, then 12.5 ns at 700 K, 12.5 ns at 800 K, followed by 125 ns at 850 K). MPMD runs for gas phase Ser cluster formation is discussed below. MPMD and trajectory stitching were implemented using in-house Python programs that were interfaced with Gromacs via bash scripts.

2.2.3 Design of Ser Monomers

The Ser amino group can exist in two protonation states ($^+\text{H}_3\text{N-R}$ or $\text{H}_2\text{N-R}$), as does the carboxyl group (R-COOH or R-COO^-). This gives rise to the four species SEN^- , SEZ (zwitterionic), SEO (both sites neutral), and SEP^+ . GROMACS *pdb2gmx* was used to add the corresponding hydrogens to monomeric Ser coordinates extracted from the L-Ser crystal structure.⁶⁹

DFT geometry optimization of SEN^- , SEO , and SEP^+ *in vacuo* yielded relaxed structures along with their E_{DFT} energies (Table 1, Figure 2.3). Dealing with SEZ was more

challenging. Like Gly,⁹⁸⁻¹⁰¹ isolated zwitterionic Ser is unstable, resulting in intramolecular SEZ \rightarrow SEO proton transfer during geometry optimization. We solved this problem by employing relaxed potential energy scanning, where the NH distance r_{NH} was fixed at certain values while the rest of the molecule was allowed to relax. SEZ structures and E_{DFT} values were extracted from these $E_{\text{DFT}}(r_{\text{NH}})$ profiles at $r_{\text{NH}} = 0.1$ nm, yielding a $^+\text{H}_3\text{N-R}$ geometry with three identical N-H bond lengths (Figure 2.4).

Two conformers were considered for SEP^+ , differing in the orientation of the carboxyl hydrogen. The lowest energy conformer had this hydrogen pointing “down” relative to the nitrogen (SEP_{down}), whereas $\sim 180^\circ$ rotation around the $\text{C}_\alpha\text{-COOH}$ bond yielded a slightly higher E_{DFT} (SEP_{up}). Table 1 summarizes E_{DFT} data from all three DFT methods. These data are plotted in Figure 2.3 on a relative scale, where each set of energy values was shifted such that the corresponding $E_{\text{DFT}}(\text{SEN}^-)$ became zero. The three DFT methods yielded similar results. Data for the more extensive 6-311+G(d,p) basis set with B3LYP and M06 were virtually indistinguishable. The widespread application of B3LYP for gaseous biomolecules,^{61, 102-113} prompted us to use B3LYP/6-311+G(d,p) E_{DFT} values for the remainder of this work. The corresponding geometry-optimized structures (Figure 2.3) served as starting point for MD simulations.

Next, we tested to what degree the DFT-optimized Ser monomer structures were retained under the MD force fields used here. The monomers were exposed to CHARMM36 or OPLS-AA energy minimization in the gas phase, with $F \leq 100$ kJ mol⁻¹ nm⁻¹ as convergence criterion. CHARMM36 retained the DFT-optimized structures more closely than OPLS-AA, evident from the average RMSD values of 0.008 vs. 0.015 nm (Appendix

3). This behavior prompted us to primarily rely on CHARMM36 for the MD simulations outlined below.

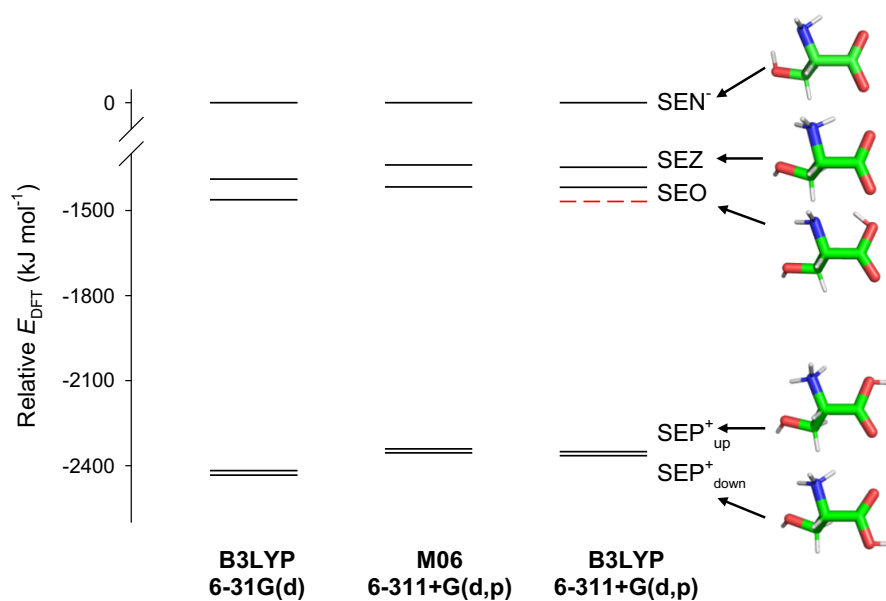


Figure 2.3 E_{DFT} data from Table 1, plotted on a relative scale where $E_{\text{DFT}}(\text{SEN})$ was shifted to zero for each DFT method. Shown along the right are B3LYP/6-311+G(d,p) geometry-optimized structures of monomeric Ser species. The red dashed line indicates the SEO rel. E_{DFT} lowered by 50 kJ mol⁻¹, as used for some MPMD simulations.

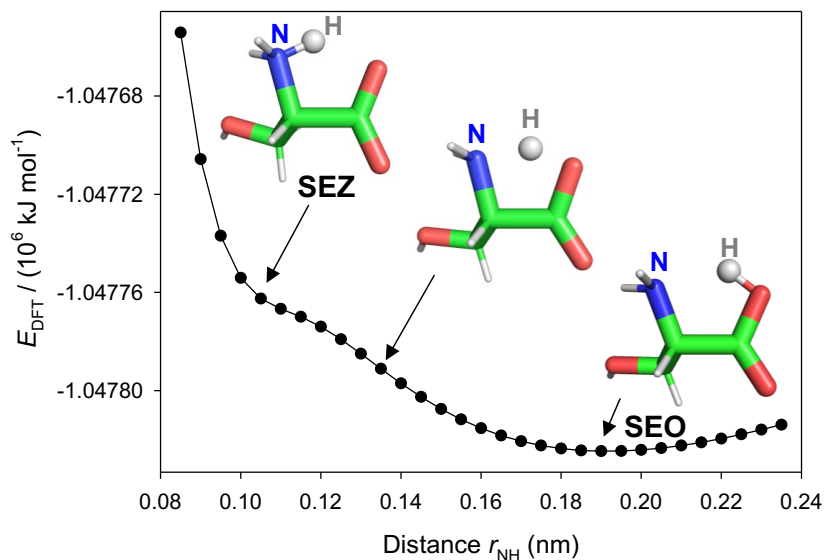


Figure 2.4 DFT relaxed scan of the SEZ \rightarrow SEO transition, yielding geometry-optimized structures and their E_{DFT} values for a range of NH distances r_{NH} . Data shown here were generated using B3LYP/6-311+G(d,p). Similar profiles were obtained with B3LYP/6-31G(d) and M06/6-311+G(d,p) (Appendix 2).

Table 1 E_{DFT} energies (kJ mol^{-1}) of different Ser species from three DFT methods.

Designation	Composition ^c	B3LYP/6-31G(d)	M06/6-311+G(d,p)	B3LYP/6-311+G(d,p)
SEN ^a	$\text{H}_2\text{N-R-COO}^-$	-1045969.5	-1045804.8	-1046406.5
SEZ ^b	$^+\text{H}_3\text{N-R-COO}^-$	-1047358.9	-1047144.2	-1047754.1
SEO ^a	$\text{H}_2\text{N-R-COOH}$	-1047431.9	-1047221.6	-1047824.7
SEP ⁺ _{up} ^a	$^+\text{H}_3\text{N-R-COOH}$	-1048386.6	-1048145.1	-1048756.8
SEP ⁺ _{down} ^a	$^+\text{H}_3\text{N-R-COOH}$	-1048402.5	-1048159.2	-1048770.8

(a) Energies refer to geometry-optimized conformers. (b) Energies were determined from relaxed scans (Figures 2.2, Appendix 2). (c) R represents $\text{CH-CH}_2\text{-OH}$.

2.2.4 Mobile Proton MD Simulations

The MPMD approach of ref. ¹¹⁴ (which had been designed for gaseous proteins) was adapted to Ser clusters. With this technique, short static-proton MD segments alternate with proton redistribution events, such that extended trajectories can be modeled while quasi-continuously updating the protonation state of all titratable sites. For the Ser clusters considered here, all protons were allowed to “hop” from occupied sites ($\text{NH}_3^+\text{-R}$ and R-COOH) to vacant sites ($\text{NH}_2\text{-R}$ and R-COO^-). Proton hopping was performed using a steepest-descent algorithm that minimizes the energy.

$$E_{MPMD} = E_{int} + E_{Coul} \quad 2.1$$

E_{Coul} in Equation 2.1 comprises electrostatic interactions among all atoms.

$$E_{Coul} = \frac{1}{4\pi\epsilon_0} \sum_{\substack{i \in I, j \in J \\ I > J}} \frac{q_i q_j}{r_{ij}} \quad 2.2$$

I and J refer to individual Ser, q_i and q_j are atomic charges in the MD force field, r_{ij} represents the corresponding distances. The intrinsic cluster energy E_{intr} in Equation 2.1 is given by Equation 2.3.

$$E_{intr} = n_{SEZ} E_{DFT}(SEZ) + n_{SEP} E_{DFT}(SEP^+) + n_{SEO} E_{DFT}(SEO) + n_{SEN} E_{DFT}(SEN^-) \quad 2.3$$

where n_{SEZ} , n_{SEP} , n_{SEO} , and n_{SEN} reflect the number of copies for each species in the cluster. E_{DFT} corresponds to the B3LYP/6-311+G(d,p) values in Table 1. For MPMD, a minor modification was applied to the E_{DFT} values to ensure that all species had the same 15 atoms, i.e., two free H^+ (internal energy = $2 \times 3/2 RT$) were added for SEN, and one free H^+ ($3/2 RT$) for SEZ and SEO. ¹¹⁵

MPMD runs employed 0.25 ns segments during which protons remained stationary. The simulation was then halted, protons were allowed to move, and the next MD segment commenced with the newly optimized proton configuration. Initial tests revealed that performing proton hopping in fixed 0.25 ns intervals was ineffective because the clusters preferentially existed in E_{MPMD} local minima, characterized by extensive salt bridges and H-bonds. Barrier crossing to more favorable E_{MPMD} was possible only during brief thermal fluctuations that perturbed charge solvation motifs. Almost none of those fluctuations coincided with the end of an MD segment, such that the use of predetermined 0.25 ns hopping intervals would imply that most opportunities to improve E_{MPMD} went unutilized. This problem was solved by allowing for proton hopping at the most likely point during each 0.25 ns segment: After completing each segment, the trajectory was analyzed to identify the structure with the largest radius of gyration (R_g). Major structural fluctuations responsible for these R_g maxima tended to provide situation with sub-optimal charge solvation, thereby promoting favorable proton hopping to a lower E_{MPMD} . In the event of successful proton hopping, the next trajectory segment continued from the maximum R_g structure with its newly optimized proton configuration. In the absence of proton hopping, the next trajectory segment continued from the final frame of the 0.25 ns segment.

2.3 Results and Discussion

2.3.1 Experimental Characterization of Ser Clusters

Earlier studies produced Ser_8H^+ by electrospraying acidified water/methanol^{53, 56, 63} or water/acetonitrile.⁵⁷ Here, we used water without organic cosolvent to simplify subsequent MD simulations. We initially acquired ESI mass spectra with minimal collisional activation (sampling cone 5 V, trap CV 2 V, trap collision gas off). The $m/z > 300$ range was dominated by Ser_8H^+ . Intense SEP^+ and dimer signals were seen at lower m/z , while low intensity larger clusters were detected at $m/z > 900$ (Figure 2.5A). These data confirm^{23, 30, 32, 52, 53, 56-65} that ESI of Ser solutions produces Ser_8H^+ as a highly abundant MNC. Figure 2.5A also shows a strong signal at m/z 421.2, dominated by $[\text{Ser}_8+2\text{H}]^{2+}$. This doubly charged MNC has been reported previously,⁶³ albeit in lower abundance than in our experiments.

Collisional activation in the ion sampling interface can trigger CID.^{2, 116-119} On our instrument, this source activation is controlled by the sampling cone voltage, illustrated in Appendix 1 for a peptide. Under gentle conditions the $[\text{M}+\text{H}]^+$ peptide ion remained intact (sampling cone 5 V, Appendix 1A). Raising the cone to 60 V caused extensive CID (Appendix 1B). At 120 V the peptide was almost completely dissociated, and at 180 V not even fragment ions remained (Appendix 1C-D).

From these peptide data it would be expected that few, if any, clusters survive when increasing the sampling cone voltage to 180 V. Surprisingly, Ser spectra acquired under these extremely harsh conditions (Figure 2.5B) were very similar to those obtained under gentle (5 V) settings. In particular, Ser_8H^+ remained dominant at 180 V. One minor

difference was that $[\text{Ser}_4+\text{H}]^+$ became the main contributor at m/z 421.2, instead of $[\text{Ser}_2+\text{H}]^{2+}$ (Figure 2.5 insets). In summary, Ser clustering and MNC formation were almost unaffected by changing the sampling cone from 5 V to 180 V, while leaving all other instrument parameters unchanged. The same was true for values in-between these two extremes (data not shown). This behavior is extremely odd, keeping in mind that “regular” analytes undergo complete CID at sampling cone 180 V (Appendix 1A-D).

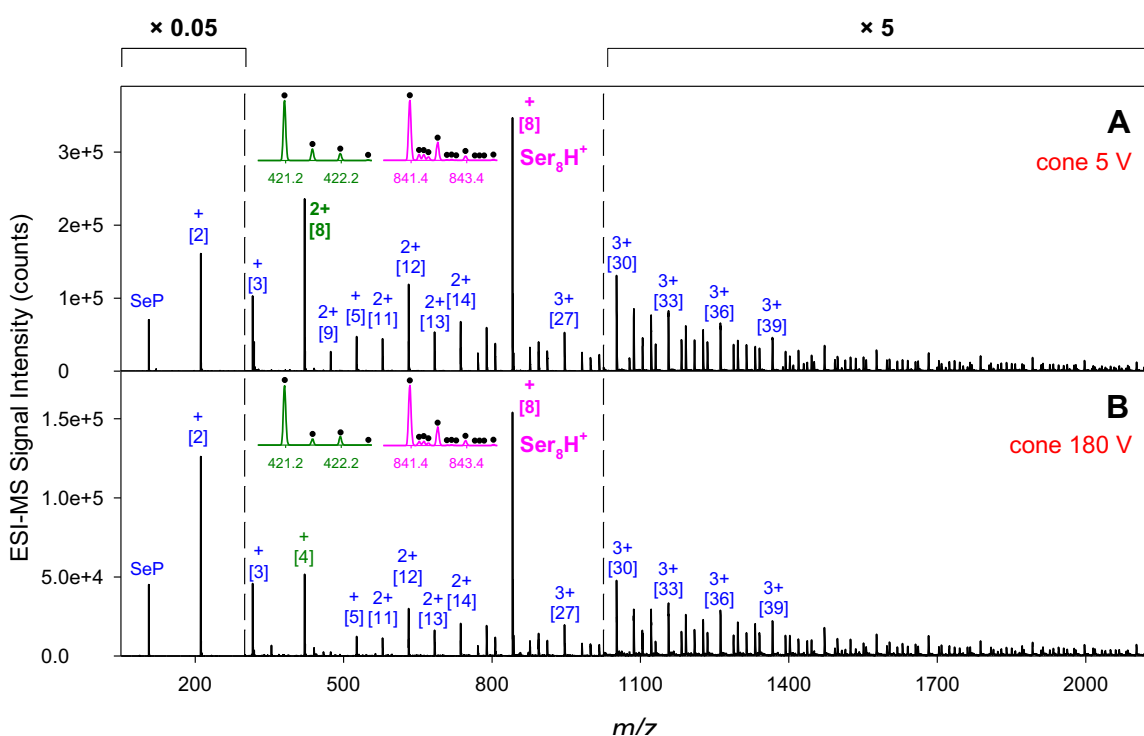


Figure 2.5 ESI mass spectra of Ser in water. Trap CV 2 V, trap collision gas off. (A) Sampling cone 5 V. (B) Sampling cone 180 V. The regions $m/z < 300$ and $m/z > 1025$ were rescaled as indicated. $[n]^{z+}$ refers to the main component, n is the number of Ser. Insets show experimental spectra and isotope models. For (A), “[8]²⁺” = 0.32[4]⁺ + 0.68[8]²⁺ and “[8]⁺” = 0.64[8]⁺ + 0.18[16]²⁺ + 0.18[24]³⁺. For (B), “[8]²⁺” = 0.61[4]⁺ + 0.39[8]²⁺ and “[8]⁺” = 0.72[8]⁺ + 0.16[16]²⁺ + 0.12[24]³⁺.

2.3.2 Ser Cluster MS/MS

It is tempting to explain the apparent resilience of Ser_8H^+ against source CID (Figure 2.5) by assuming that this MNC is highly stable, allowing it to survive extreme collisional activation. However, MS/MS experiments showed this interpretation to be incorrect. Quadrupole isolation of Ser_8H^+ at a trap CV of 2 V without collision gas produced a clean precursor signal (Figure 2.6A). Addition of collision gas under otherwise identical conditions triggered extensive fragmentation (Figure 2.6B), even though collisional activation at this trap CV is minimal (causing no fragmentation for peptide ions (Appendix 1E) or NaCl MNCs¹²⁰).

A slight increase in trap CV to 8 V led to near-complete CID of Ser_8H^+ (Figure 2.6C). Other Ser clusters were similarly sensitive to MS/MS CID, exemplified in Figure 2.6E-P. In all cases, the lowest possible trap CV already triggered extensive fragmentation. Each cluster showed a size-specific trap CV where Ser_8H^+ was formed in relatively high abundance, accompanied by other fragments (Figure 2.6G, K, O). High trap CV values mainly produced SEP^+ and Ser dimers (Figure 2.5H, L, P). The data of Figure 2.6 are consistent with earlier work.⁶³ The low MS/MS resilience seen in Figure 2.6 makes the immunity of Ser clusters to source activation (Figure 2.5) even more perplexing.

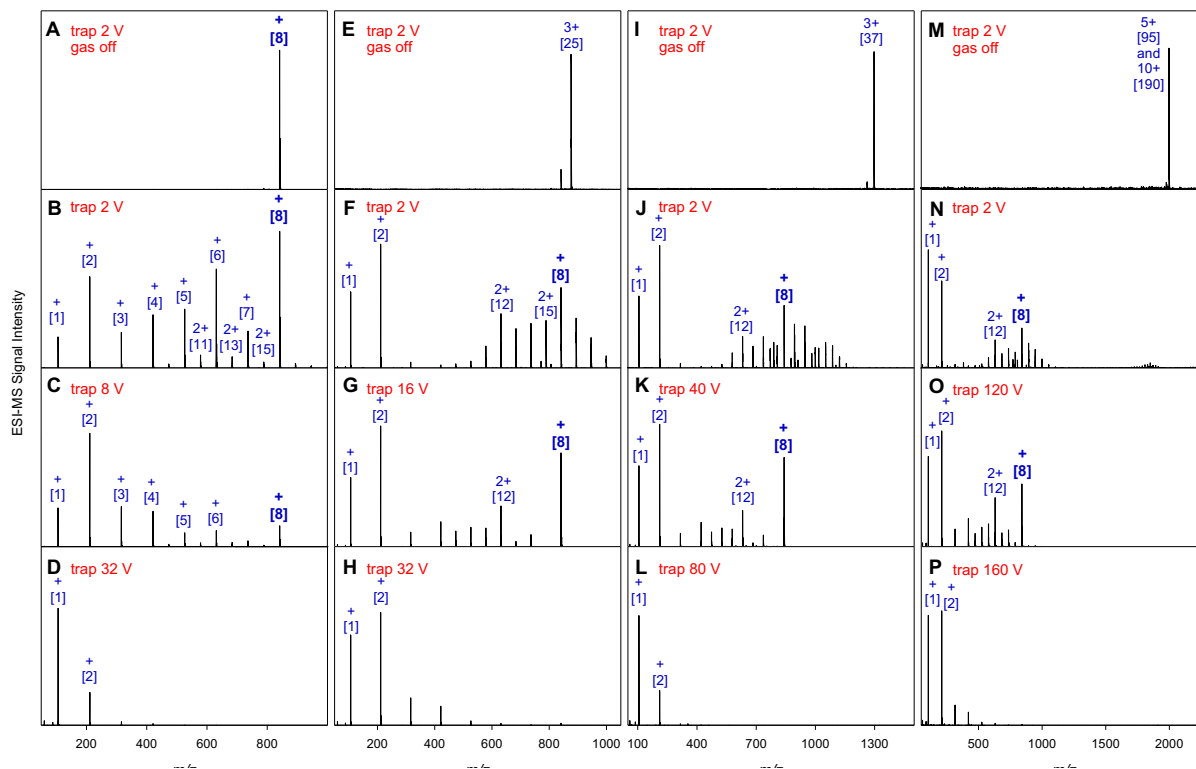


Figure 2.6 MS/MS of Ser clusters. Each column is for one precursor ion. Trap CV values are indicated. Row 1: trap collision gas off. Rows 2-4: trap collision gas on. The cone was set to 5 V for all spectra. Peak annotation is analogous to that of Figure 5. Precursor ions used: (A-D) $841 = \text{Ser}_8\text{H}^+ = [8]^+$, (E-H) $876 = [25]^{3+}$, (I-L) $1297 = [37]^{3+}$, (M-P) $1998 =$ overlap of $[95]^{5+}$ and $[190]^{10+}$.

2.3.3 Evidence for Ser Clustering in the Gas Phase

How can one reconcile that Ser_8H^+ “survives” under the harshest possible source conditions, while being extremely vulnerable to MS/MS CID? Our explanation initially focuses on data acquired at sampling cone 180 V. We propose that Ser clusters formed in evaporating ESI droplets^{30, 53, 59, 63} undergo near-complete source CID, producing abundant SEP^+ and neutral Ser monomers. These neutrals will adopt the non-zwitterionic SEO state.
^{32, 99} Experimentally observable clusters arise from *reclustering* of these SEP^+/SEO

monomers in the gas phase after the source. Specifically, we envision SEP⁺/SEO association in the extraction cone jet, where clustering is favored by adiabatic cooling. The relationship¹²¹ $T/T_0 = (p/p_0)^{0.29}$ implies that T in the extraction cone free jet can drop to ~30 K, for a p/p_0 pressure ratio of 0.0004 (Figure 2.2) and an initial temperature of $T_0 = 300$ K. Ion-neutral clustering is a well-known phenomenon,¹²² particularly in free jets.⁷⁵

¹²¹ SEP⁺/SEO clustering is promoted by the high Ser concentration used here and in previous work (≥ 5 mM).^{53, 56, 57, 63} Typical ESI solutions are much more dilute (μ M).¹ Low intensity larger clusters in Figure 2.5B may be the remnants of droplet-generated clusters, after incomplete source CID, followed by association with SEO in the gas phase.

Next, one must ask why virtually identical spectra were observed under harsh and gentle source conditions (Figure 2.5A vs. 5B). This similarity of outcomes suggests that both scenarios share a similar cluster formation mechanism. Accordingly, we propose that even at sampling cone 5 V source CID of droplet-generated clusters produces abundant SEP⁺ and SEO. CID can take place at low sampling cone voltages because (i) the +2800 V potential of the ESI capillary is a significant contributor to source activation,¹²³ and (ii) Ser clusters are extremely CID-vulnerable (Figure 2.5). We envision that SEP⁺ and SEO liberated by source CID then recluster in the extraction cone jet, as outlined above for sampling cone 180 V.

In summary, we propose the following main pathway for Ser₈H⁺ formation under typical ESI conditions (e.g., Figure 2.5A). Step 1: Nonspecific Ser clusters form in evaporating ESI droplets. Step 2: Droplet-generated clusters undergo facile CID in the source, forming SEP⁺ and SEO. Step 3: SEP⁺ and SEO form clusters in the low temperature of the extraction cone jet, driven by charge-dipole interactions. The clusters generated in this way may again

experience collisional activation and dissociation as they pass through downstream ion optics such as TWIG1 in Figure 2.2 (Step 4).

Our proposal reconciles the perplexing observation that Ser_8H^+ and other Ser clusters are seemingly immune to source CID, while being highly sensitive to MS/MS CID. We attribute cluster immunity to source CID to cluster formation in the gas phase, after the source. To our knowledge, gas phase assembly as the major pathway toward MS-observable Ser clusters under standard conditions has not been identified previously (despite cursory speculations in the early literature³²).

2.3.4 DFT and MD Characterization of the Scutelnic Model

DFT represents the gold standard for gas phase computational investigations,^{61, 102-113} but ESI and CID events take place on ns to ms time scales¹ that are inaccessible to such high level methods. Classical MD simulations represent an alternative, as they can probe large systems on long time scales. However, compared to DFT, MD force-fields take a somewhat simplified view of atomic interactions. We scrutinized the MD tools used in this work by benchmarking them against DFT data, focusing on the Scutelnic Ser_8H^+ model.⁶¹ That model had been developed using DFT at the B3LYP/6-31G(d,p) level (Figure 2.1E).⁶¹ Prior to any MD, we performed B3LYP geometry optimization of the Scutelnic model using the larger 6311+G(d,p) basis set. This procedure preserved the Ser_8H^+ structure⁶¹ (RMSD 0.01 nm, Appendix 4), confirming that the Scutelnic model⁶¹ represents a viable octamer structure.

Next, the Scutelnic model⁶¹ was used as starting point for 10 ns gas phase CHARMM36 MD simulations at 100 K. The resulting MD structures remained close to their starting point (RMSD 0.081 ± 0.002 nm, Figure 2.7A), demonstrating that the DFT structure is

CHARMM36-compatible. The cluster stayed intact even at 300 K, although this higher MD temperature caused reorientation of some Ser building blocks (RMSD 0.27 ± 0.03 nm, Figure 2.7B). These 300 K dynamics are consistent with experimentally observed Ser₈H⁺ structural heterogeneity,^{60, 71, 72} keeping in mind that the Scutelnic model⁶¹ represents a 0 K structure that does not reflect the cluster behavior at higher temperatures. The situation is reminiscent of cryogenic protein crystal structures that do not capture dynamic motions taking place under ambient conditions.^{124, 125} Overall, Figures 2.7A, B demonstrate that CHARMM36 can retain gas phase structures similar to the Scutelnic model,⁶¹ confirming that this MD force field is compatible with DFT results of Ser clustering.

2.3.5 Solution Phase MD Simulations

Some studies proposed Ser₈H⁺ formation via Ser clustering in bulk solution prior to ESI.^{32, 52, 65, 73} We examined this possibility, first by performing MD simulations of the Scutelnic model⁶¹ in water at 300 K. The Ser₈H⁺ structure started to dissolve within 1 ns, and after 10 ns the cluster had completely disintegrated (Figure 2.7C, D). Similar dissolution kinetics were observed for a neutral Ser₈ cluster (where SEP⁺ had been converted to SEZ, data not shown). Rapid dissolution of Ser₈H⁺ in water is in stark contrast to the gas phase MD data of Figure 2.7B, where the cluster remained intact.

Next, we tested the possibility of Ser cluster formation in aqueous solution at the solubility limit of 4 M at 300 K.¹²⁶ The simulations employed SEZ, reflecting the dominance of this zwitterionic state in solution.^{32, 99} 10 ns MD simulations yielded a loosely connected SEZ network with dynamic salt bridges, resembling the behavior of other amino acids.¹²⁷ These bulk simulations provided no evidence for Ser octamers or other distinct clusters. Our data are consistent with spectroscopic experiments that found no Ser clusters in aqueous

solution.^{73, 74} Thus, clustering in bulk solution as an explanation for the highly abundant Ser_8H^+ signal in ESI mass spectra is unlikely, although a minor contribution of this formation mechanism cannot be ruled out.⁵²

We now return to the Ser_8H^+ formation mechanism that we proposed above on the basis of our experiments (Figures 2.5 and 2.6). Each of the four steps will be scrutinized in MD simulations.

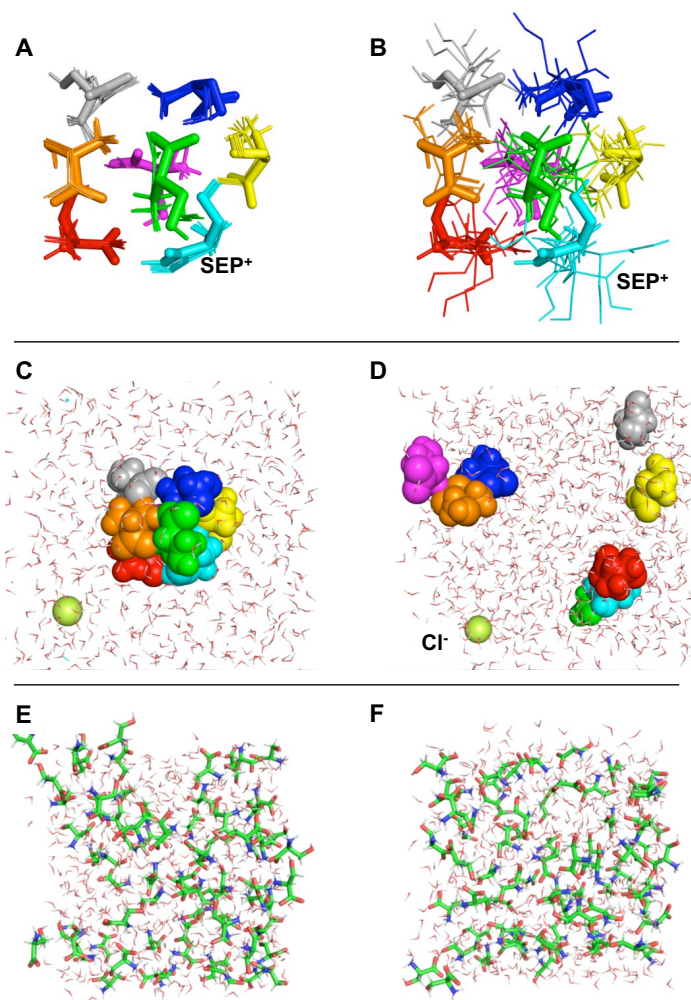


Figure 2.7 (A) The Scutelnic Ser₈H⁺ model⁶¹ is displayed in thick sticks. Thin lines illustrate how this structure evolved after five independent 10 ns MD runs in the gas phase at 100 K. Individual Ser are colored differently, the single SEP (cyan) is highlighted. (B) Same as panel A, but for five MD runs at 300 K. (C) MD simulation of the Scutelnic Ser₈H⁺ model in bulk water at $t = 0$, and (D) after 10 ns at 300 K. The simulation box also contained one Cl⁻ to ensure charge neutrality. (E) 4 M SEZ in bulk water at $t = 0$, and (F) after 10 ns at 300 K.

2.3.6 Simulating Step 1: Ser Clustering in ESI Droplets

ESI simulations were conducted on aqueous droplets with a 2.5 nm initial radius, consistent with nanodroplets in the ESI plume.¹ The prevalence of zwitterionic amino acids in solution^{32, 99, 100, 128} prompted us to use SEZ as the default species. However, ESI droplets carry a net charge caused by electrolytically generated protons (14+ for $r = 2.5$ nm, see Methods).¹²⁹ Rather than exist as free H_3O^+ ,^{130, 131} these protons will be consumed via $\text{SEZ} \rightarrow \text{SEP}^+$ conversion, as dictated by the equilibrium constant¹³² of $\text{R-COO}^- + \text{H}^+ \rightleftharpoons \text{RCOOH}$, $K = (K_a)^{-1} \approx 10^4$. Accordingly, the 14+ droplet charge was implemented by including 14 SEP^+ .

Figure 2.8A-D shows snapshots from a typical MD trajectory, for a droplet initially containing 12 SEZ and 14 SEP^+ . Temporal changes in droplet composition are summarized in Figure 2.8E. Water evaporation caused progressive shrinkage. Electrostatically driven IEM events triggered the loss of most SEP^+ (Figure 2.8B), resembling the behavior of other charge carriers in earlier ESI simulations.¹³³⁻¹³⁵ The nonvolatile nature and lack of net charge caused all SEZ to remain in the droplet, giving rise to the horizontal profile in Figure 2.8E. This particular run culminated in a dry $[\text{SEZ}_{12} + \text{SEP}_3]^{3+}$ cluster (Figure 2.8D). Cluster formation via solvent evaporation to dryness was observed in all our droplet runs, consistent with the CRM.^{4, 6, 27-29}

Simulations were performed for droplets containing 14 SEP^+ and 5 to 20 SEZ, covering compositions that could potentially generate octamers. Six independent runs were performed for each composition, for 96 simulations in total. The resulting cluster sizes ranged from $[\text{SEZ}_3 + \text{SEP}_2]^{2+}$ to $[\text{SEZ}_{19} + \text{SEP}_5]^{5+}$. All clusters exhibited an extensive salt

bridge network among the SEZ and SEP⁺. All but one of the droplet-generated clusters were multiply charged (Figure 2.8F).

Our simulations confirm the occurrence of CRM clustering in evaporating ESI droplets, as proposed earlier.^{30, 53, 59, 63} However, our data do not support the view^{52, 53} that this clustering preferentially generates Ser₈H⁺. Instead, the simulations produced a broad distribution of clusters (Figure 2.8F), resembling nonspecific association events seen for many other analytes.^{11-13, 15-18, 24-27}

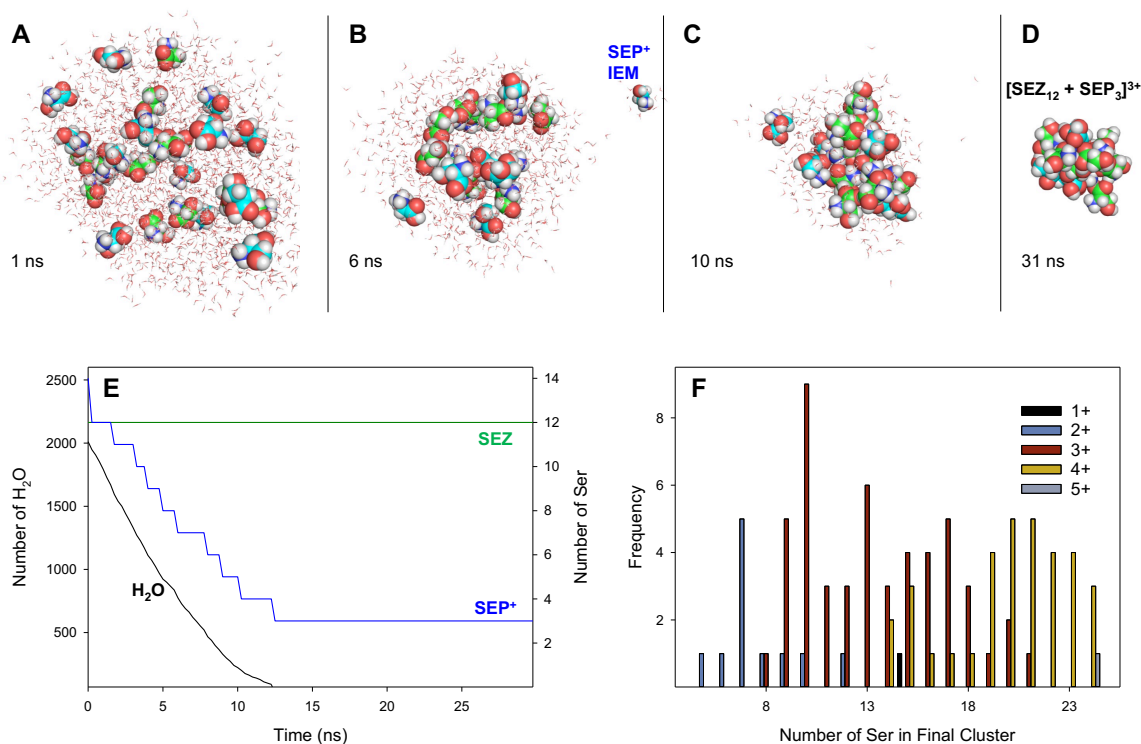


Figure 2.8 MD simulations of evaporating aqueous ESI nanodroplets. (A-D) Snapshots taken from a typical trajectory. SEZ and SEP are depicted in spacefill representation. (E) Droplet composition vs. time for the run of panels A-D. (F) Composition of clusters produced in 96 repeat runs for droplet with different initial SEZ numbers. Element coloring is as in Figure 1.

2.3.7 Design of MPMD CID Simulations

Prior to tackling Step 2 of our proposed mechanism, we have to address an important issue. Protons in gaseous biomolecular ions are highly mobile.^{97, 114, 136-141} Unfortunately, conventional MD force fields do not allow for proton transfer. To address this limitation, we recently developed a MPMD technique¹¹⁴ that permits time-dependent changes of proton configurations in proteins. Here, we adapted this approach to Ser clusters (see Methods).

MPMD allows for conversion between SEZ, SEP⁺, SEO, and SEN⁻, subject to charge conservation. However, we found that E_{MPMD} considerations (equation 1) only permitted for certain types of events. All SEP⁺ remained stable, i.e., they did not transfer protons to other units. SEN⁻ never became populated because of its unfavorable E_{DFT} (Figure 2.3). Intramolecular SEZ \rightleftharpoons SEO conversion was the only prevalent proton transfer event in our MPMD runs. Isolated SEO is more stable than SEZ (Figures 2.3, 2.4). However, SEZ can become favored by electrostatic stabilization in the cluster, triggering SEO \rightarrow SEZ conversion.^{32, 53, 69, 98-101} Conversely, reduced electrostatic destabilization due to changes of the SEZ environment can promote SEZ \rightarrow SEO events.

Figure 2.6 demonstrates that MS/MS of large Ser clusters produces abundant monomers, in addition to Ser₈H⁺ and other clusters.⁶³ Those experiments served as benchmark for designing proper CID simulation conditions. Initial tests showed that droplet-generated Ser clusters (from Figure 2.8F) were quite heat-resistant during MPMD. For example, heating of [SEZ₁₉ SEP₅]⁵⁺ to 950 K triggered several [SEZ + SEP]⁺ ejections, but the remaining cluster remained intact for hundreds of nanoseconds (Appendix 5A). Several features of such MPMD data are inconsistent with experiments. (i) High thermal stability clashes with

the cluster sensitivity to MS/MS (Figure 2.6).⁶³ (ii) MPMD did not trigger neutral losses which are prevalent in MS/MS.^{53, 63} (iii) Although protons are known to be highly mobile,^{97, 114, 136-141} MPMD executed only very few transfers, e.g., one SEZ \rightarrow SEO transition in Appendix 5A. (iv) The conditions of Appendix 5A did not generate Ser₈H⁺. (v) 950 K is higher than the 550 K to 740 K ion temperatures in standard experiments.^{112, 142, 143}

Issues i-iii are caused by the overrepresentation of SEZ under the conditions of Appendix 5A, keeping in mind that SEZ forms salt bridges that are very stable in the gas phase.¹⁴⁴ We addressed this problem by a slight $E_{\text{DFT}}(\text{SEO})$ shift (by -50 kJ mol^{-1} , dashed line in Figure 2.3). This minor modification had major repercussions, as it favored complete cluster dissociation (Appendix 5B consistent with our MS/MS data at high trap CV (Figure 2.6). The reduced cluster stability after this $E_{\text{DFT}}(\text{SEO})$ adjustment is caused by more frequent SEZ \rightarrow SEO transitions. SEO H-bonding in the cluster (as opposed to more stable salt bridge formation) implies that SEZ \rightarrow SEO conversion invariably triggers SEO neutral loss. Issue iv was addressed by exempting clusters consisting of eight Ser from the aforementioned $E_{\text{DFT}}(\text{SEO})$ modification. This empirical intervention was designed to capture the experimentally observed formation of Ser₈H⁺ at certain trap CV. For addressing issue v, we settled on lower temperatures (12.5 ns at 700 K, 12.5 ns at 800 K, and 125 ns at 850 K) which are close to the experimentally determined range.^{112, 142, 143}

2.3.8 Simulating Step 2: CID of Droplet-Assembled Clusters

We modeled source CID of all droplet-generated clusters (Figure 2.8F) using the MPMD conditions identified in the preceding section. Most runs showed a behavior similar to that illustrated along the top of Figure 2.9. Occasional SEZ \rightarrow SEO conversion triggered SEO evaporation from the cluster (Figure 2.9B). Another dissociation pathway was the ejection

or SEP^+ , almost always in the form of dimers ($[\text{SEZ} + \text{SEP}]^+$, Figure 2.9C). Ultimately, these events decimated the clusters to monomeric SEP^+ and SEO (Figure 2.9D). Time-dependent changes in cluster composition are exemplified in Figure 2.9I. A different behavior was seen for 14% of the simulations (Figure 2.9E-H, J). Although the initial SEO and SEP^+ losses were similar to the events described above, Ser_8H^+ remained as survivor of the CID process (Figure 2.9H).

Overall, CID simulations of droplet-generated clusters resulted in the product distribution shown in Figure 2.9K. The main products were SEP^+ and SEO, the latter being ca. fourfold more abundant. The Ser_8H^+ contribution of to the overall ion count in Figure 2.9K was 4%, the remainder being SEP^+ . Qualitatively, these simulated CID data match the experimental MS/MS behavior at moderate to high trap CV values, with dominant dissociation of multiply charged clusters into monomers with a small Ser_8H^+ contribution (Figure 2.6, bottom two rows).

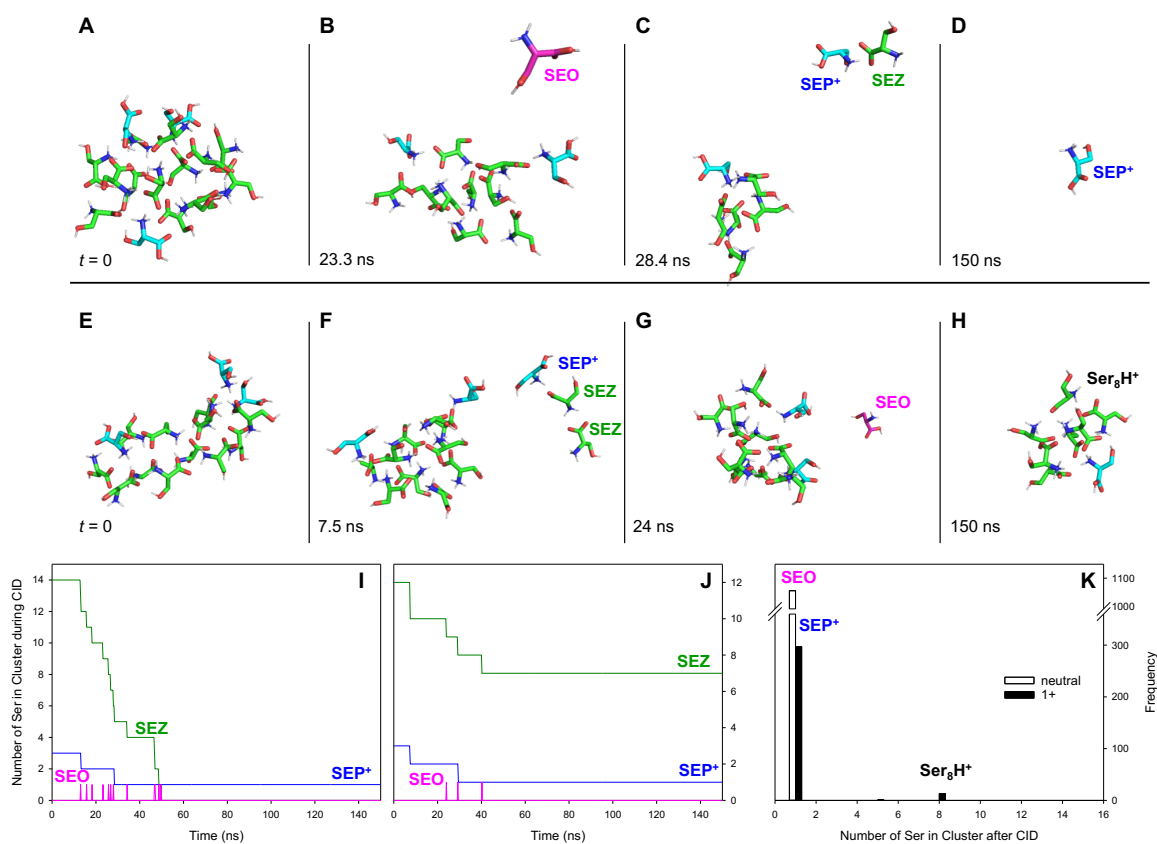


Figure 2.9 MPMD simulations of Ser cluster CID. The $t = 0$ clusters for this data were formed in ESI droplets. (A-D) Snapshots from a trajectory where $[\text{SEZ}_{14} \text{SEP}_3]^{3+}$ dissociates into SEP^+ . (E-H) Snapshots from a trajectory where $[\text{SEZ}_{12} \text{SEP}_3]^{3+}$ dissociates into Ser_8H^+ . (I) Cluster composition vs. time for panels A-D. (J) Cluster composition vs. time for panels E-H. (K) Product distribution generated by CID of all 96 clusters.

2.3.9 Simulating Step 3: Ser Cluster Formation in the Gas Phase

MPMD simulations were conducted to examine the viability of the next step of our proposed mechanism, i.e., clustering of gaseous monomers in the extraction cone jet. The temperature of 100 K used for this stage is a conservative estimate, as adiabatic cooling may generate temperatures as low as 30 K (discussed above). The simulations were based on free monomeric SEP^+ and SEO , which were formed in high abundance in the preceding step (Figure 2.9K). Repeat MPMD simulations were performed by placing a single SEP in

the center of a (15 nm)³ box, surrounded by randomly placed SEO. Trajectory snapshots demonstrate the facile formation of Ser clusters in the gas phase, driven charge-dipole attraction between SEO and the SEP⁺-containing nucleus (Figure 2.10A-D). Time-dependent changes in the composition of a typical cluster are displayed in Figure 2.10E, highlighting how most of the captured SEO units convert to SEZ as a result of favorable charge solvation within the cluster, concomitant with extensive salt bridge formation.

Different initial scenarios were considered, with 5 to 20 SEO in the simulation box, and 6 repeat runs for each condition for a total of 96 gas-phase assembled clusters. A histogram summarizing the outcome of these simulations shows a wide range of nonspecific cluster compositions (Figure 2.9F). Thus, our data confirm a strong propensity for Ser cluster formation in the gas phase, supporting the viability of Step 3 in our proposed clustering mechanism.

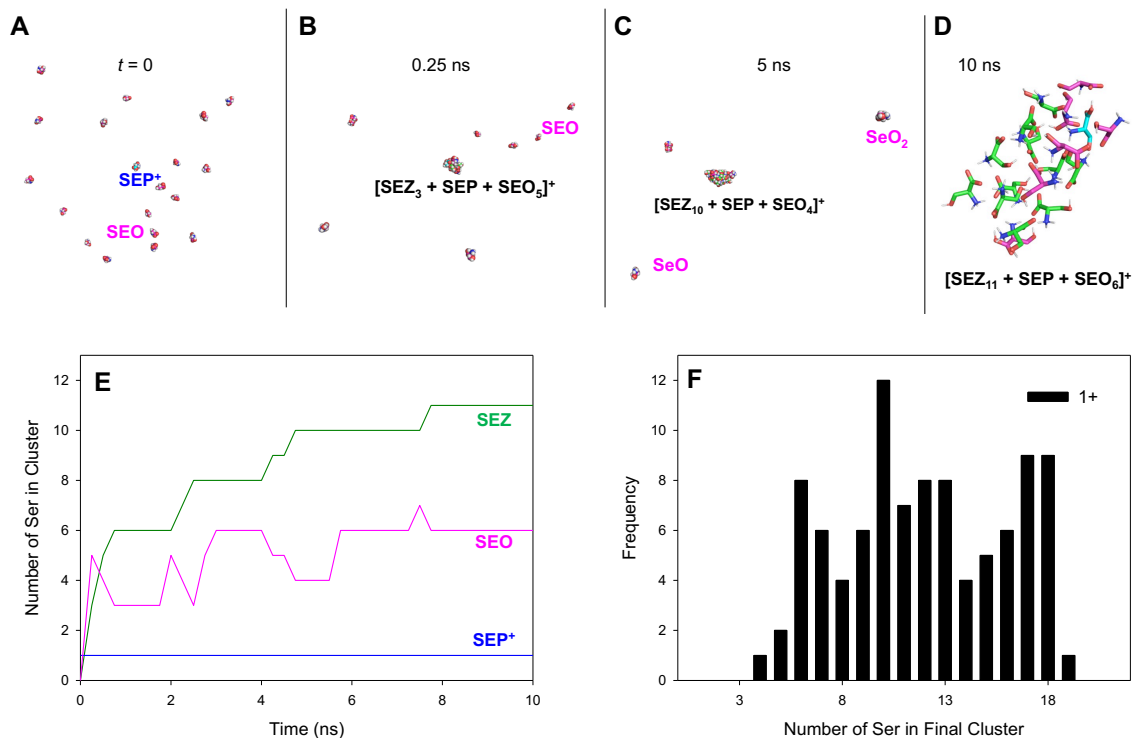


Figure 2.10 MPMD simulations of Ser clustering in the gas phase. (A-D) Snapshots from a trajectory where one SEP associates with numerous SEO into a cluster. (E) Cluster composition vs. time for panels A-D. (F) Product distribution from 96 runs with different initial SEO numbers.

2.3.10 Simulating Step 4: CID of Gas Phase-Assembled Clusters

Because Ser clustering in the gas phase did not result in preferential Ser₈H⁺ formation (Step 3, Figure 2.10F), CID of the gas phase-assembled clusters is included as the Step 4 of our proposed MNC formation mechanism. This collisional heating may take place in TWIG1, i.e., directly after the extraction cone jet (Figure 2.2), where effective ion temperatures up to 744 K may be encountered.¹⁴³ RF heating in the quadrupole can contribute to cluster activation as well.¹⁴⁵

Using the same MPMD simulation conditions as above for Figure 2.9, we simulated CID of all 96 gas phase assembled Ser clusters from Figure 2.10F. We emphasize that all of these gas phase assembly products are singly charged. As a result, SEZ \rightarrow SEO conversion with subsequent SEO evaporation was the dominant cluster decomposition pathway (Figure 2.11A-E). Gratifyingly, a large fraction (40%) of the CID trajectories under these conditions culminated in Ser₈H⁺. The Ser₈H⁺ contribution of to the overall ion count in Figure 2.11F was 40%, the remainder being SEP⁺ and low abundance 5mers to 10mers. The tenfold higher Ser₈H⁺ yield observed here for gas phase-assembled clusters compared to CID of droplet-assembly products is attributed to the fact that the latter are multiply charged (Figure 2.8F), providing them with a high propensity for extensive dissociation. In contrast, the singly charged gas phase assembly products of Figure 2.10F are less reactive, resulting in much gentler CID events that tend to seize once the metastable Ser₈H⁺ MNC is attained.

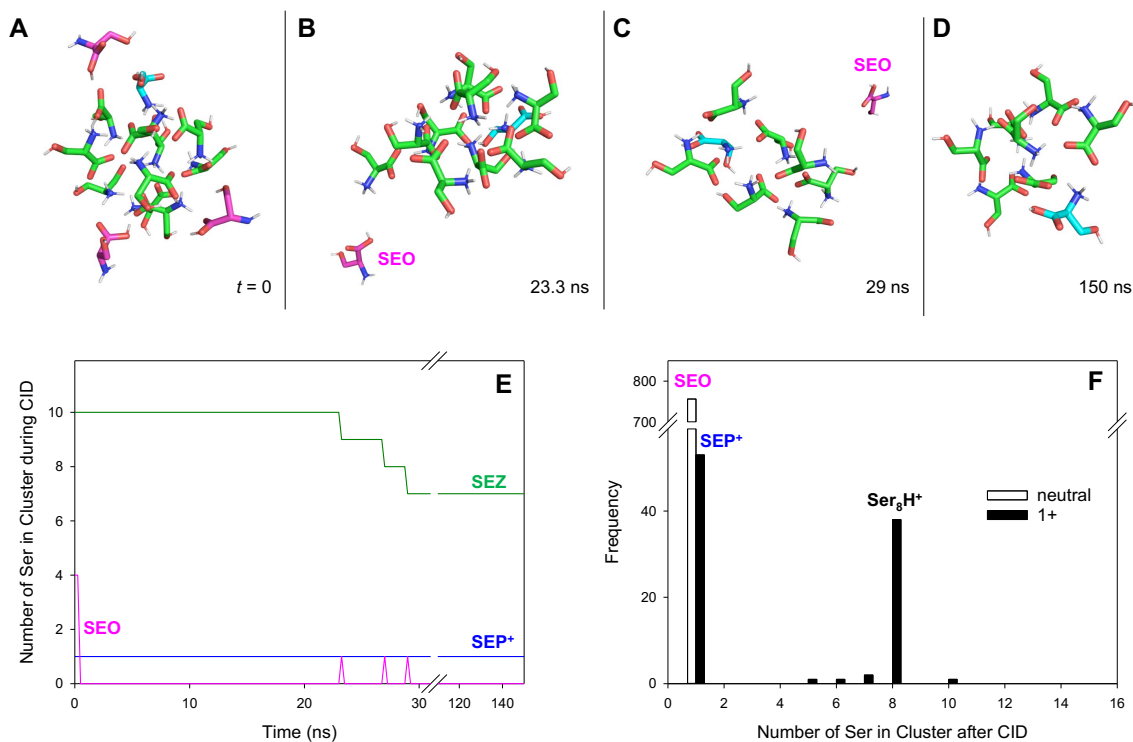


Figure 2.11 MPMD simulations of Ser cluster CID. The $t = 0$ clusters for this data set were generated by gas phase assembly. (A-D) Snapshots from a trajectory where $[\text{SEZ}_{10} + \text{SEP} + \text{SEO}_4]^+$ undergoes stepwise dissociation into Ser_8H^+ . (E) Cluster composition vs. time for panels A-D. (F) Product distribution generated after CID of all 96 clusters.

2.4 Conclusions

For the first time, this work provides a compelling mechanism that accounts for the formation of a highly abundant Ser_8H^+ MNC following ESI of 5 mM Ser in aqueous solution. Starting from the perplexing experimental observation that Ser_8H^+ and other (lower abundance) Ser clusters are seemingly immune to source CID, we proposed a step-by-step mechanism that involves cluster assembly in the gas phase as a key element. As far as we are aware, the involvement of gas phase assembly processes has not thus far been seriously considered in the Ser cluster literature. Rather than just rely on conjecture during the interpretation of our experiments, we verified that each step of our proposed Ser_8H^+

clustering mechanism can be recreated in atomistic MD simulations. The inclusion of a custom-designed MPMD protocol was essential in this context, because otherwise it would have been impossible to model Ser cluster CID events which rely on intramolecular SEZ \rightarrow SEO proton transfer. Overall, we propose that Ser₈H⁺ MNC formation under standard ESI experimental conditions starts with nonspecific Ser clusters form in evaporating ESI droplets. These initial clusters then undergo CID in the source, forming SEP⁺ and SEO. Subsequently, SEP⁺ and SEO recluster in the low temperature of the extraction cone jet. The final step is the “maturation” of these gas phase assembly products by gentle collisional activation, favoring the formation of Ser₈H⁺ MNC as the final reaction product. Overall, this study illustrates that ESI-MS detectable clusters can originate from highly complex events that involve successive stages of clustering and dissociation. It remains to be seen if the scenario uncovered here for Ser₈H⁺ also applies to other MNCs.

2.5 References

- (1) Kebarle, P.; Verkerk, U. H. Electrospray: From Ions in Solutions to Ions in the Gas Phase, What We Know Now. *Mass Spectrom. Rev.* **2009**, *28*, 898-917.
- (2) Gabelica, V.; De Pauw, E. Internal Energy and Fragmentation of Ions Produced in Electrospray Sources. *Mass Spectrom. Rev.* **2005**, *24*, 566-587.
- (3) Feketeova, L.; O'Hair, R. A. J. Comparison of collision- versus electron-induced dissociation of sodium chloride cluster cations. *Rapid Commun. Mass Spectrom.* **2009**, *23*, 60-64.
- (4) Wang, G.; Cole, R. B. Charged residue versus ion evaporation for formation of alkali metal halide clusters ions in ESI. *Anal. Chim. Acta* **2000**, *406*, 53-65.
- (5) Gamero-Castano, M.; de la Mora, J. F. Modulations in the Abundance of Salt Clusters in Electrosprays. *Anal. Chem.* **2000**, *72*, 1426-1429.
- (6) Juraschek, R.; Dulcks, T.; Karas, M. Nanoelectrospray - More than just a Minimized-Flow Electrospray Ionization Source. *J. Am. Soc. Mass Spectrom.* **1999**, *10*, 300-308.
- (7) Hudgins, R. R.; Dugourd, P.; Tenenbaum, J. M.; Jarrold, M. F. Structural transitions in sodium chloride nanocrystals. *Phys. Rev. Lett.* **1997**, *78*, 4213-4216.
- (8) Boock, J. J.; Yost, R. A. Behavior of transition metal salts during the electrospray ionization process. *Int. J. Mass Spectrom.* **2019**, *446*, 8.
- (9) Hao, C. Y.; March, R. E.; Croley, T. R.; Smith, J. C.; Rafferty, S. P. Electrospray ionization tandem mass spectrometric study of salt cluster ions. Part 1 - Investigations of alkali metal chloride and sodium salt cluster ions. *J. Mass Spectrom.* **2001**, *36*, 79-96.
- (10) Zhang, D. X.; Cooks, R. G. Doubly charged cluster ions (NaCl)_m(Na)₂ (2⁺): magic numbers, dissociation, and structure. *Int. J. Mass Spectrom.* **2000**, *195*, 667-684.
- (11) Lubbert, C.; Peukert, W. Characterization of Electrospray Drop Size Distributions by Mobility-Classified Mass Spectrometry: Implications for Ion Clustering in Solution and Ion Formation Pathways. *Anal. Chem.* **2021**, *93*, 12862-12871.
- (12) Lane, L. A.; Ruotolo, B. T.; Robinson, C. V.; Favrin, G.; Benesch, J. L. P. A Monte Carlo approach for assessing the specificity of protein oligomers observed in nano-electrospray mass spectra. *Int. J. Mass Spectrom.* **2009**, *283*, 169-177.

- (13) Aliyari, E.; Konermann, L. Atomistic Insights into the Formation of Nonspecific Protein Complexes during Electrospray Ionization. *Anal. Chem.* **2021**, *93*, 12748-12757.
- (14) Susa, A. C.; Xia, Z. J.; Williams, E. R. Native Mass Spectrometry from Common Buffers with Salts That Mimic the Extracellular Environment. *Angew. Chem.-Int. Edit.* **2017**, *56*, 7912-7915.
- (15) Wang, W.; Kitova, E. N.; Klassen, J. S. Nonspecific Protein-Carbohydrate Complexes Produced by Nanoelectrospray Ionization. Factors Influencing Their Formation and Stability. *Anal. Chem.* **2005**, *77*, 3060-3071.
- (16) Jørgensen, T. J. D.; Hvelplund, P.; Andersen, J. U.; Roepstorff, P. Tandem mass spectrometry of specific vs. nonspecific noncovalent complexes of vancomycin antibiotics and peptide ligands. *Int. J. Mass Spec.* **2002**, *219*, 659-670.
- (17) Hu, J.; Guan, Q. Y.; Wang, J.; Jiang, X. X.; Wu, Z. Q.; Xia, X. H.; Xu, J. J.; Chen, H. Y. Effect of Nanoemitters on Suppressing the Formation of Metal Adduct Ions in Electrospray Ionization Mass Spectrometry. *Anal. Chem.* **2017**, *89*, 1838-1845.
- (18) Daubenfeld, T.; Bouin, A.-P.; van der Rest, G. A Deconvolution Method for the Separation of Specific Versus Nonspecific Interactions in Noncovalent Protein-Ligand Complexes Analyzed by ESI-FT-ICR Mass Spectrometry. *J. Am. Soc. Mass Spectrom.* **2006**, *17*, 1239-1248.
- (19) Leib, R. D.; Williams, E. R. Simultaneous Quantitation of Amino Acid Mixtures using Clustering Agents. *J. Am. Soc. Mass Spectrom.* **2011**, *22*, 624-632.
- (20) Do, T. D.; de Almeida, N. E. C.; LaPointe, N. E.; Chamas, A.; Feinstein, S. C.; Bowers, M. T. Amino Acid Metaclusters: Implications of Growth Trends on Peptide Self-Assembly and Structure. *Anal. Chem.* **2016**, *88*, 868-876.
- (21) Nemes, P.; Schlosser, G.; Vékey, K. Amino acid cluster formation studied by electrospray ionization mass spectrometry. *J. Mass Spectrom.* **2005**, *40*, 43-49.
- (22) Meng, C. K.; Fenn, J. B. Formation of Charged Clusters During Electrospray Ionization of Organic Solute Species. *Org. Mass Spectrom.* **1991**, *26*, 542-549.
- (23) Julian, R. R.; Myung, S.; Clemmer, D. E. Spontaneous anti-resolution in heterochiral clusters of serine. *Journal of the American Chemical Society* **2004**, *126*, 4110-4111.

- (24) Qian, C.; Fu, H. Q.; Kovalchik, K. A.; Li, H. H.; Chen, D. D. Y. Specific Binding Constant and Stoichiometry Determination in Free Solution by Mass Spectrometry and Capillary Electrophoresis Frontal Analysis. *Anal. Chem.* **2017**, *89*, 9483-9490.
- (25) Marchand, A.; Gabelica, V. Native Electrospray Mass Spectrometry of DNA G-Quadruplexes in Potassium Solution. *J. Am. Soc. Mass Spectrom.* **2014**, *25*, 1146-1154.
- (26) Davidson, K. L.; Oberreit, D. R.; Hogan, C. J.; Bush, M. F. Nonspecific aggregation in native electrokinetic nanoelectrospray ionization. *Int. J. Mass Spectrom.* **2017**, *420*, 35-42.
- (27) Benesch, J. L. P.; Ruotolo, B. T.; Simmons, D. A.; Robinson, C. V. Protein Complexes in the Gas Phase: Technology for Structural Genomics and Proteomics. *Chem. Rev.* **2007**, *107*, 3544-3567.
- (28) Zhou, S.; Hamburger, M. Formation of Sodium Cluster Ions in Electrospray Mass Spectrometry. *Rapid Commun. Mass Spectrom.* **1996**, *10*, 797-800.
- (29) Konermann, L.; Haidar, Y. Mechanism of Magic Number NaCl Cluster Formation from Electrosprayed Water Nanodroplets. *Anal. Chem.* **2022**, *94*, 16491-16501.
- (30) Spencer, E. A. C.; Ly, T.; Julian, R. K. Formation of the serine octamer: Ion evaporation or charge residue? *Int. J. Mass Spectrom.* **2008**, *270*, 166-172.
- (31) Shukla, A.; Bogdanov, B. Lithium formate ion clusters formation during electrospray ionization: Evidence of magic number clusters by mass spectrometry and ab initio calculations. *J. Chem. Phys.* **2015**, *142*, 13.
- (32) Schalley, C. A.; Weis, P. Unusually stable magic number clusters of serine with a surprising preference for homochirality. *Int. J. Mass Spectrom.* **2002**, *221*, 9-19.
- (33) Ryding, M. J.; Izsak, R.; Merlot, P.; Reine, S.; Helgaker, T.; Uggerud, E. Geometry of the magic number H⁺(H₂O)₍₂₁₎ water cluster by proxy. *Phys. Chem. Chem. Phys.* **2015**, *17*, 5466-5473.
- (34) Lee, S. W.; Freivogel, P.; Schindler, T.; Beauchamp, J. L. Freeze-dried biomolecules: FT-ICR studies of the specific solvation of functional groups and clathrate formation observed by the slow evaporation of water from hydrated peptides and model compounds in the gas phase. *J. Am. Chem. Soc.* **1998**, *120*, 11758-11765.
- (35) Hogan, C. J.; de la Mora, J. F. Ion-Pair Evaporation from Ionic Liquid Clusters. *J. Am. Soc. Mass Spectrom.* **2010**, *21*, 1382-1386.

- (36) Chang, T. M.; Cooper, R. J.; Williams, E. R. Locating Protonated Amines in Clathrates. *J. Am. Chem. Soc.* **2013**, *135*, 14821-14830.
- (37) Fournier, J. A.; Johnson, C. J.; Wolke, C. T.; Weddle, G. H.; Wolk, A. B.; Johnson, M. A. Vibrational spectral signature of the proton defect in the three-dimensional H+(H₂O)(21) cluster. *Science* **2014**, *344*, 1009-1012.
- (38) Blades, A. T.; Peschke, M.; Verkerk, U. H.; Kebarle, P. Hydration energies in the gas phase of select (MX)(m)M⁺ ions, where M⁺ = Na⁺, K⁺, Rb⁺, Cs⁺, NH₄(⁺) and X⁻ = F⁻, Cl⁻, Br⁻, I⁻, NO₂⁻, NO₃⁻. Observed magic numbers of (MX)(m)M⁺ ions and their possible significance. *J. Am. Chem. Soc.* **2004**, *126*, 11995-12003.
- (39) Wakisaka, A. Nucleation in alkali metal chloride solution observed at the cluster level. *Faraday Discuss.* **2007**, *136*, 299-308.
- (40) Wilcoxon, J. P.; Abrams, B. L. Synthesis, structure and properties of metal nanoclusters. *Chem. Soc. Rev.* **2006**, *35*, 1162-1194.
- (41) Echt, O.; Sattler, K.; Recknagel, E. Magic Numbers for Sphere Packings: Experimental Verification in Free Xenon Clusters. *Phys. Rev. Lett.* **1981**, *47*, 1121-1124.
- (42) Brack, M. The physics of simple metal clusters: self-consistent jellium model and semiclassical approaches. *Rev. Mod. Phys.* **1993**, *65*, 677-732.
- (43) McBride, J. R.; Dukes, A. D.; Schreuder, M. A.; Rosenthal, S. J. On ultrasmall nanocrystals. *Chem. Phys. Lett.* **2010**, *498*, 1-9.
- (44) Wang, J. W.; Mbah, C. F.; Przybilla, T.; Zubiri, B. A.; Spiecker, E.; Engel, M.; Vogel, N. Magic number colloidal clusters as minimum free energy structures. *Nat. Commun.* **2018**, *9*, 10.
- (45) Smalley, R. E. Self-assembly of the fullerenes. *Acc. Chem. Res.* **1992**, *25*, 98-105.
- (46) Guo, B. C.; Kerns, K. P.; Castleman, A. W. Ti₈C₁₂⁺-Metallo-Carbohedrenes: A New Class of Molecular Clusters? *Science* **1992**, *255*, 1411-1413.
- (47) Whitlam, S.; Jack, R. L. The Statistical Mechanics of Dynamic Pathways to Self-Assembly. *Annu. Rev. Phys. Chem.* **2015**, *66*, 143-163.
- (48) Kim, S.; Zhou, S.; Hu, Y. K.; Acik, M.; Chabal, Y. J.; Berger, C.; de Heer, W.; Bongiorno, A.; Riedo, E. Room-temperature metastability of multilayer graphene oxide films. *Nat. Materials* **2012**, *11*, 544-549.

- (49) Gettins, P. G. W. Serpin Structure, Mechanism, and Function. *Chem. Rev.* **2002**, *102*, 4751-4803.
- (50) Anderson, S. L.; Gladysiak, A.; Boyd, P. G.; Ireland, C. P.; Miéville, P.; Tiana, D.; Vlaisavljevich, B.; Schouwink, P.; van Beek, W.; Gagnon, K. J., et al. Formation pathways of metal-organic frameworks proceeding through partial dissolution of the metastable phase. *Crystengcomm* **2017**, *19*, 3407-3413.
- (51) Mbah, C. F.; Wang, J. W.; Englisch, S.; Bommineni, P.; Varela-Rosales, N. R.; Spiecker, E.; Vogel, N.; Engel, M. Early-stage bifurcation of crystallization in a sphere. *Nat. Commun.* **2023**, *14*, 9.
- (52) Jordan, J. S.; Williams, E. R. Effects of Electrospray Droplet Size on Analyte Aggregation: Evidence for Serine Octamer in Solution. *Anal. Chem.* **2021**, *93*, 1725-1731.
- (53) Julian, R. R.; Hodyss, R.; Kinnear, B.; Jarrold, M. F.; Beauchamp, J. L. Nanocrystalline aggregation of serine detected by electrospray ionization mass spectrometry: Origin of the stable homochiral gas-phase serine octamer. *J. Phys. Chem. B* **2002**, *106*, 1219-1228.
- (54) Lanaro, G.; Patey, G. N. Birth of NaCl Crystals: Insights from Molecular Simulations. *J. Phys. Chem. B* **2016**, *120*, 9076-9087.
- (55) Lutsko, J. F. How crystals form: A theory of nucleation pathways. *Sci. Adv.* **2019**, *5*, eaav7399.
- (56) Cooks, R. G.; Zhang, D. X.; Koch, K. J.; Gozzo, F. C.; Eberlin, M. N. Chiroselective self-directed octamerization of serine: Implications for homochirogenesis. *Anal. Chem.* **2001**, *73*, 3646-3655.
- (57) Counterman, A. E.; Clemmer, D. E. Magic number clusters of serine in the gas phase. *J. Phys. Chem. B* **2001**, *105*, 8092-8096.
- (58) Julian, R. R.; Myung, S.; Clemmer, D. E. Do homochiral aggregates have an entropic advantage? *Journal of Physical Chemistry B* **2005**, *109*, 440-444.
- (59) Nanita, S. C.; Cooks, R. G. Serine octamers: Cluster formation, reactions, and implications for biomolecule homochirality. *Angew. Chem.-Int. Edit.* **2006**, *45*, 554-569.
- (60) Sunahori, F. X.; Yang, G. C.; Kitova, E. N.; Klassen, J. S.; Xu, Y. J. Chirality recognition of the protonated serine dimer and octamer by infrared multiphoton dissociation spectroscopy. *Phys. Chem. Chem. Phys.* **2013**, *15*, 1873-1886.

- (61) Scutelnic, V.; Perez, M. A. S.; Marianski, M.; Warnke, S.; Gregor, A.; Rothlisberger, U.; Bowers, M. T.; Baldauf, C.; von Helden, G.; Rizzo, T. R., et al. The Structure of the Protonated Serine Octamer. *J. Am. Chem. Soc.* **2018**, *140*, 7554-7560.
- (62) Zhang, H.; Wei, Z. W.; Jiang, J.; Cooks, R. G. Nebulization Prior to Isolation, Ionization, and Dissociation of the Neutral Serine Octamer Allows Its Characterization. *Angew. Chem.-Int. Edit.* **2018**, *57*, 17141-17145.
- (63) Jordan, J. S.; Williams, E. R. Dissociation of large gaseous serine clusters produces abundant protonated serine octamer. *Analyst* **2021**, *146*, 2617-2625.
- (64) Jordan, J. S.; Williams, E. R. Homochiral preference of serine octamer in solution and formed by dissociation of large gaseous clusters. *Analyst* **2021**, *146*, 6822-6830.
- (65) Seo, J.; Warnke, S.; Pagel, K.; Bowers, M. T.; von Helden, G. Infrared spectrum and structure of the homochiral serine octamer-dichloride complex. *Nat. Chem.* **2017**, *9*, 1263-1268.
- (66) Yang, P. X.; Xu, R. F.; Nanita, S. C.; Cooks, R. G. Thermal formation of homochiral serine clusters and implications for the origin of homochirality. *J. Am. Chem. Soc.* **2006**, *128*, 17074-17086.
- (67) Nanita, S. C.; Cooks, R. G. Negatively-charged halide adducts of homochiral serine octamers. *J. Phys. Chem. B* **2005**, *109*, 4748-4753.
- (68) Aguado, A. An ab initio study of the structures and relative stabilities of doubly charged (NaCl)(m)(Na)(2) (2+) cluster ions. *J. Phys. Chem. B* **2001**, *105*, 2761-2765.
- (69) Kistenmacher, T. J.; Rand, G. A.; Marsh, R. E. Refinements of the Crystal Structures of DL-Serine and Anhydrous L-Serine. *Acta Crystallogr. Sect. B-Struct. Sci. Cryst. Eng. Mat.* **1974**, *30*, 2573-2578.
- (70) Costa, S. N.; Sales, F. A. M.; Freire, V. N.; Maia, F. F.; Caetano, E. W. S.; Ladeira, L. O.; Albuquerque, E. L.; Fulco, U. L. L-Serine Anhydrous Crystals: Structural, Electronic, and Optical Properties by First-Principles Calculations, and Optical Absorption Measurement. *Cryst. Growth Des.* **2013**, *13*, 2793-2802.
- (71) Kong, X. L.; Lin, C.; Infusini, G.; Oh, H. B.; Jiang, H. H.; Breuker, K.; Wu, C. C.; Charkin, O. P.; Chang, H. C.; McLafferty, F. W. Numerous Isomers of Serine Octamer Ions Characterized by Infrared Photodissociation Spectroscopy. *ChemPhysChem* **2009**, *10*, 2603-2606.

- (72) Mazurek, U.; Geller, O.; Lifshitz, C.; McFarland, M. A.; Marshall, A. G.; Reuben, B. G. Protonated serine octamer cluster: Structure elucidation by gas-phase H/D exchange reactions. *J. Phys. Chem. A* **2005**, *109*, 2107-2112.
- (73) Vandenbussehe, S.; Vandenbussche, G.; Reisse, J.; Bartik, K. Do serine octamers exist in solution? Relevance of this question in the context of the origin of homochirality on earth. *Eur. J. Org. Chem.* **2006**, *2006*, 3069-3073.
- (74) Ramírez, F. J.; Tuñón, I.; Silla, E. Amino acid chemistry in solution:: structural properties and vibrational dynamics of serine using density functional theory and a continuum solvent model. *Chemical Physics* **2004**, *303*, 85-96.
- (75) Fenn, J. B. Mass spectrometric implications of high-pressure ion sources. *Int. J. Mass Spectrom.* **2000**, *200*, 459-478.
- (76) Michaelevski, I.; Kirshenbaum, N.; Sharon, M. T-wave Ion Mobility-mass Spectrometry: Basic Experimental Procedures for Protein Complex Analysis. *J. Vis. Exp.* **2010**, *40*, e1954.
- (77) Pringle, S. D.; Giles, K.; Wildgoose, J. L.; Williams, J. P.; Slade, S. E.; Thalassinos, K.; Bateman, R. H.; Bowers, M. T.; Scrivens, J. H. An investigation of the mobility separation of some peptide and protein ions using a new hybrid quadrupole/travelling wave IMS/oa-ToF instrument. *Int. J. Mass Spectrom.* **2007**, *261*, 1-12.
- (78) Frisch, M. J.; Trucks, G. W.; Schlegel, H. B.; Scuseria, G. E.; Robb, M. A.; Cheeseman, J. R.; Scalmani, G.; Barone, V.; Mennucci, B.; Petersson, G. A., et al., *Gaussian 09 Revision E.01*. Gaussian Inc.: Wallingford CT, 2013.
- (79) Stephens, P. J.; Devlin, F. J.; Chabalowski, C. F.; Frisch, M. J. Ab initio calculation of vibrational absorption and circular dichroism spectra using density functional force fields. *J. Phys. Chem.* **1994**, *98*, 11623-11627.
- (80) Zhao, Y.; Truhlar, D. G. The M06 suite of density functionals for main group thermochemistry, thermochemical kinetics, noncovalent interactions, excited states, and transition elements: two new functionals and systematic testing of four M06-class functionals and 12 other functionals. *Theor. Chem. Acc.* **2008**, *120*, 215-241.
- (81) Abraham, M. J.; Murtola, T.; Schulz, R.; Páll, S.; Smith, J. C.; Hess, B.; Lindahl, E. GROMACS: High performance molecular simulations through multi-level parallelism from laptops to supercomputers. *SoftwareX* **2015**, *1-2*, 19-25.

- (82) Huang, J.; MacKerell, A. D. CHARMM36 all-atom additive protein force field: Validation based on comparison to NMR data. *J. Comput. Chem.* **2013**, *34*, 2135-2145.
- (83) Piana, S.; Lindorff-Larsen, K.; Shaw, D. E. Atomic-level description of ubiquitin folding. *Proc. Natl. Acad. Sci. U.S.A.* **2013**, *110*, 5915-5920.
- (84) Mao, Y.; Woenckhaus, J.; Kolafa, J.; Ratner, M. A.; Jarrold, M. F. Thermal unfolding of unsolvated cytochrome c: Experiment and molecular dynamics simulations. *J. Am. Chem. Soc.* **1999**, *121*, 2712-2721.
- (85) Lee, J. W.; Davidson, K. L.; Bush, M. F.; Kim, H. I. Collision cross sections and ion structures: development of a general calculation method via high-quality ion mobility measurements and theoretical modeling. *Analyst* **2017**, *142*, 4289-4298.
- (86) Zhang, J. C.; Bogdanov, B.; Parkins, A.; McCallum, C. M. Observation of Magic Number Clusters from Thermal Dissociation Molecular Dynamics Simulations of Lithium Formate Ionic Clusters. *J. Phys. Chem. A* **2020**, *124*, 3535-3541.
- (87) Kaminski, G. A.; Friesner, R. A.; Tirado-Rives, J.; Jorgensen, W. L. Evaluation and reparametrization of the OPLS-AA force field for proteins via comparison with accurate quantum chemical calculations on peptides. *J. Phys. Chem. B* **2001**, *105*, 6474-6487.
- (88) Fegan, S. K.; Thachuk, M. Suitability of the MARTINI Force Field for Use with Gas-Phase Protein Complexes. *J. Chem. Theory Comput.* **2012**, *8*, 1304-1313.
- (89) Popa, V.; Trecroce, D. A.; McAllister, R. G.; Konermann, L. Collision-Induced Dissociation of Electrosprayed Protein Complexes: An All-Atom Molecular Dynamics Model with Mobile Protons. *J. Phys. Chem. B* **2016**, *120*, 5114-5124.
- (90) Marchese, R.; Grandori, R.; Carloni, R.; Raugei, S. A Computational Model for Protein Ionization by Electrospray Based on Gas-Phase Basicity. *J. Am. Soc. Mass Spectrom.* **2012**, *23*, 1903-1910.
- (91) Patriksson, A.; Adams, C. M.; Kjeldsen, F.; Zubarev, R. A.; van der Spoel, D. A direct comparison of protein structure in the gas and solution phase: The TRP-cage. *J. Phys. Chem. B* **2007**, *111*, 13147-13150.
- (92) Ly, T.; Julian, R. R. Elucidating the Tertiary Structure of Protein Ions in Vacuo with Site Specific Photoinitiated Radical Reactions. *J. Am. Chem. Soc.* **2010**, *132*, 8602-8609.

- (93) Bleiholder, C.; Liu, F. C. Structure Relaxation Approximation (SRA) for Elucidation of Protein Structures from Ion Mobility Measurements. *J. Phys. Chem. B* **2019**, *123*, 2756-2769.
- (94) Lemkul, J. A. From Proteins to Perturbed Hamiltonians: A Suite of Tutorials for the GROMACS-2018 Molecular Simulation Package. *Living J. Comp. Mol. Sci* **2019**, *1*, 5068.
- (95) de la Mora, J. F. Electrospray Ionization of large multiply charged species proceeds via Dole's charged residue mechanism. *Anal. Chim. Acta* **2000**, *406*, 93-104.
- (96) Grimm, R. L.; Beauchamp, J. L. Evaporation and Discharge Dynamics of Highly Charged Multicomponent Droplets Generated by Electrospray Ionization. *J. Phys. Chem. A* **2010**, *114*, 1411-1419.
- (97) Fegan, S. K.; Thachuk, M. A Charge Moving Algorithm for Molecular Dynamics Simulations of Gas-Phase Proteins. *J. Chem. Theory Comput.* **2013**, *9*, 2531-2539.
- (98) Yu, D.; Armstrong, D. A.; Rauk, A. Hydrogen bonding and internal rotation barriers of glycine and its zwitterion (hypothetical) in the gas phase. *Can. J. Chem.* **1992**, *70*, 1762-1772.
- (99) Locke, M. J.; McIver, R. T. Effect of Solvation on the Acid/Base Properties of Glycine. *J. Am. Chem. Soc.* **1983**, *105*, 4226-4232.
- (100) Jensen, J. H.; Gordon, M. S. On the Number of Water Molecules Necessary To Stabilize the Glycine Zwitterion. *J. Am. Chem. Soc.* **1995**, *117*, 8159-8170.
- (101) Wyttenbach, T.; Witt, M.; Bowers, M. T. On the stability of amino acid zwitterions in the gas phase: The influence of derivatization, proton affinity, and alkali ion addition. *J. Am. Chem. Soc.* **2000**, *122*, 3458-3464.
- (102) Marchese, R.; Grandori, R.; Carloni, P.; Raugei, S. On the Zwitterionic Nature of Gas-Phase Peptides and Protein Ions. *PLoS Comput. Biol.* **2010**, *6*, e1000775.
- (103) Bonner, J. G.; Lyon, Y. A.; Nellessen, C.; Julian, R. R. Photoelectron Transfer Dissociation Reveals Surprising Favorability of Zwitterionic States in Large Gaseous Peptides and Proteins. *J. Am. Chem. Soc.* **2017**, *139*, 10286-10293.
- (104) Heiles, S.; Berden, G.; Oomens, J.; Williams, E. R. Competition between salt bridge and non-zwitterionic structures in deprotonated amino acid dimers. *Phys. Chem. Chem. Phys.* **2018**, *20*, 15641-15652.

- (105) Bell, M. R.; Cruzeiro, V. W. D.; Cismesia, A. P.; Tesler, L. F.; Roitberg, A. E.; Polfer, N. C. Probing the Structures of Solvent-Complexed Ions Formed in Electrospray Ionization Using Cryogenic Infrared Photodissociation Spectroscopy. *J. Phys. Chem. A* **2018**, *122*, 7427-7436.
- (106) Stedwell, C. N.; Galindo, J. F.; Gulyuz, K.; Roitberg, A. E.; Polfer, N. C. Crown Complexation of Protonated Amino Acids: Influence on IRMPD Spectra. *J. Phys. Chem. A* **2013**, *117*, 1181-1188.
- (107) Bleiholder, C.; Suhai, S.; Paizs, B. Revising the proton affinity scale of the naturally occurring alpha-amino acids. *J. Am. Soc. Mass Spectrom.* **2006**, *17*, 1275-1281.
- (108) Fu, W.; Carr, P. J. J.; Lecours, M. J.; Burt, M.; Marta, R. A.; Steinmetz, V.; Fillion, E.; McMahon, T. B.; Hopkins, W. S. Intramolecular cation-pi interactions in protonated phenylalanine derivatives. *Phys. Chem. Chem. Phys.* **2017**, *19*, 729-734.
- (109) Chen, Y.; Rodgers, M. T. Structural and Energetic Effects in the Molecular Recognition of Amino Acids by 18-Crown-6. *J. Am. Chem. Soc.* **2012**, *134*, 5863-5875.
- (110) Ziegler, B. E.; Lecours, M.; Marta, R. A.; Featherstone, J.; Fillion, E.; Hopkins, W. S.; Steinmetz, V.; Keddie, N. S.; O'Hagan, D.; McMahon, T. B. Janus Face Aspect of All-cis 1,2,3,4,5,6-Hexafluorocyclohexane Dictates Remarkable Anion and Cation Interactions in the Gas Phase. *J. Am. Chem. Soc.* **2016**, *138*, 7460-7463.
- (111) Shaffer, C. J.; Andrikopoulos, P. C.; Řezáč, J.; Rulišek, L.; Tureček, F. Efficient Covalent Bond Formation in Gas-Phase Peptide-Peptide Ion Complexes with the Photoleucine Stapler. *J. Am. Soc. Mass Spectrom.* **2016**, *27*, 633-645.
- (112) Carpenter, J. E.; McNary, C. P.; Furin, A.; Sweeney, A. F.; Armentrout, P. B. How Hot are Your Ions Really? A Threshold Collision-Induced Dissociation Study of Substituted Benzylpyridinium "Thermometer" Ions. *J. Am. Soc. Mass Spectrom.* **2017**, *28*, 1876-1888.
- (113) Rodriguez, C. F.; Orlova, G.; Guo, Y.; Li, X.; Siu, C.-K.; Hopkinson, A. C.; Siu, K. W. M. Gaseous Bradykinin and Its Singly, Doubly, and Triply Protonated Forms: A First-Principles Study. *J. Phys. Chem. B.* **2006**, *110*, 7528-7537.
- (114) Moore, C. C.; Staroverov, V. N.; Konermann, L. Using Density Functional Theory for Testing the Robustness of Mobile-Proton Molecular Dynamics Simulations on

Electrosprayed Ions: Structural Implications for Gaseous Proteins. *J. Phys. Chem. B* **2023**, *127*, 4061-4071.

(115) Moser, A.; Range, K.; York, D. M. Accurate Proton Affinity and Gas-Phase Basicity Values for Molecules Important in Biocatalysis. *J. Phys. Chem. B* **2010**, *114*, 13911-13921.

(116) Kitova, E. N.; El-Hawiet, A.; Schnier, P. D.; Klassen, J. S. Reliable Determinations of Protein–Ligand Interactions by Direct ESI-MS Measurements. Are We There Yet? *J. Am. Soc. Mass Spectrom.* **2012**, *23*, 431-441.

(117) Collings, B. A.; Douglas, D. J. Conformation of Gas-Phase Myoglobin Ions. *J. Am. Chem. Soc.* **1996**, *118*, 4488-4489.

(118) Thomson, B. A. Declustering and Fragmentation of Protein Ions from an Electrospray Ion Source. *J. Am. Soc. Mass Spectrom.* **1997**, *8*, 1053-1058.

(119) Wilson, J. W.; Donor, M. T.; Shepherd, S. O.; Prell, J. S. Increasing Collisional Activation of Protein Complexes Using Smaller Aperture Source Sampling Cones on a Synapt Q-IM-TOF Instrument with a Stepwave Source. *J. Am. Soc. Mass Spectrom.* **2020**, *31*, 1751-1754.

(120) Schachel, T.; Metwally, H.; Popa, V.; Konermann, L. Collision-Induced Dissociation of Electrosprayed NaCl Clusters: Using Molecular Dynamics Simulations to Visualize Reaction Cascades in the Gas Phase. *J. Am. Soc. Mass Spectrom.* **2016**, *27*, 1846-1854.

(121) Smalley, R. E.; Wharton, L.; Levy, D. H. Molecular Optical Spectroscopy with Supersonic Beams and Jets. *Accounts Chem. Res.* **1977**, *10*, 139-145.

(122) Haack, A.; Crouse, J.; Schluter, F.-J.; Benter, T.; Hopkins, W. S. A First Principle Model of Differential Ion Mobility: the Effect of Ion-Solvent Clustering. *J. Am. Soc. Mass Spectrom.* **2019**, *30*, 2711-2725.

(123) Shepherd, S. O.; Green, A. W.; Resendiz, E. S.; Newton, K. R.; Kurulugama, R. T.; Prell, J. S. Effects of Nano-Electrospray Ionization Emitter Position on Unintentional In-Source Activation of Peptide and Protein Ions. *J. Am. Soc. Mass Spectrom.* **2024**, *35*, 498-507.

- (124) Perez, L. M.; Ielasi, F. S.; Bessa, L. M.; Maurin, D.; Kragelj, J.; Blackledge, M.; Salvi, N.; Bouvignies, G.; Palencia, A.; Jensen, M. R. Visualizing protein breathing motions associated with aromatic ring flipping. *Nature* **2022**, *602*, 695-+.
- (125) Henzler-Wildman, K. A.; Lei, M.; Thai, V.; Kerns, S. J.; Karplus, M.; Kern, D. A hierarchy of timescales in protein dynamics is linked to enzyme catalysis. *Nature* **2007**, *450*, 913-918.
- (126) Fan, Y. W.; Zhu, W. J.; Hu, Y. H.; Yang, W. G.; Xu, Q.; Liu, X. X.; Heng, B. The Research and Measurement about the Solubility of L-Serine in Eight Common Pure Solvents and Four Binary Mixed Solvents for $T = (278.15-333.15)$ K. *J. Chem. Eng. Data* **2019**, *64*, 4398-4411.
- (127) Ng, Y. K.; Konermann, L. Mechanism of Protein Aggregation Inhibition by Arginine: Blockage of Anionic Side Chains Favors Unproductive Encounter Complexes. *J. Am. Chem. Soc.* **2024**, *146*, 8394-8406.
- (128) Sweatman, M. B.; Afify, N. D.; Ferreira-Rangel, C. A.; Jorge, M.; Sefcik, J. Molecular Dynamics Investigation of Clustering in Aqueous Glycine Solutions. *Journal of Physical Chemistry B* **2022**, *126*, 4711-4722.
- (129) Van Berkel, G. J.; Kertesz, V. Using the Electrochemistry of the Electrospray Ion Source. *Anal. Chem.* **2007**, *79*, 5511-5520.
- (130) Cordes, M. S.; Gallagher, E. S. Molecular Dynamics Simulations of Native Protein Charging via Proton Transfer during Electrospray Ionization with Grotthuss Diffuse H₃O⁺. *Anal. Chem.* **2024**, *in press*.
- (131) Konermann, L.; Liu, Z. Y.; Haidar, Y.; Willans, M. J.; Bainbridge, N. A. On the Chemistry of Aqueous Ammonium Acetate Droplets during Native Electrospray Ionization Mass Spectrometry. *Anal. Chem.* **2023**, *95*, 13957-13966.
- (132) Creighton, T. E., *Proteins*. W. H. Freeman & Co: New York, 1993.
- (133) Konermann, L.; Metwally, H.; McAllister, R. G.; Popa, V. How to run molecular dynamics simulations on electrospray droplets and gas phase proteins: Basic guidelines and selected applications. *Methods* **2018**, *144*, 104-112.
- (134) Znamenskiy, V.; Marginean, I.; Vertes, A. Solvated Ion Evaporation from Charged Water Droplets. *J. Phys. Chem. A* **2003**, *107*, 7406-7412.

- (135) Consta, S. Fragmentation reactions of charged aqueous clusters. *J. Mol. Struct. (Theochem)* **2002**, *591*, 131-140.
- (136) Dongré, A. R.; Jones, J. L.; Somogyi, Á.; Wysocki, V. H. Influence of Peptide Composition, Gas-Phase Basicity, and Chemical Modification on Fragmentation Efficiency: Evidence for the Mobile Proton Model. *J. Am. Chem. Soc.* **1996**, *118*, 8365-8374.
- (137) Summerfield, S. G.; Gaskell, S. J. Fragmentation efficiencies of peptide ions following low energy collisional activation. *Int. J. Mass Spectrom.* **1997**, *165/166*, 509-521.
- (138) Boyd, R. K.; Somogyi, Á. The Mobile Proton Hypothesis in Fragmentation of Protonated Peptides: A Perspective. *J. Am. Soc. Mass Spectrom.* **2010**, *21*, 1275-1278.
- (139) Polasky, D. A.; Dixit, S. M.; Keating, M. F.; Gadkari, V. V.; Andrews, P. C.; Ruotolo, B. T. Pervasive Charge Solvation Permeates Native-like Protein Ions and Dramatically Influences Top-down Sequencing Data. *J. Am. Chem. Soc.* **2020**, *142*, 6750-6760.
- (140) Jurchen, J. C.; Williams, E. R. Origin of Asymmetric Charge Partitioning in the Dissociation of Gas-Phase Protein Homodimers. *J. Am. Chem. Soc.* **2003**, *125*, 2817-2826.
- (141) Felitsyn, N.; Kitova, E. N.; Klassen, J. S. Thermal Decomposition of a Gaseous Multiprotein Complex Studied by Blackbody Infrared Radiative Dissociation. Investigating the Origin of the Asymmetric Dissociation Behavior. *Anal. Chem.* **2001**, *73*, 4647-4661.
- (142) Morsa, D.; Gabelica, V.; De Pauw, E. Effective Temperature of Ions in Traveling Wave Ion Mobility Spectrometry. *Anal. Chem.* **2011**, *83*, 5775-5782.
- (143) Merenbloom, S. I.; Flick, T. G.; Williams, E. R. How Hot are Your Ions in TWAVE Ion Mobility Spectrometry? *J. Am. Soc. Mass Spectrom.* **2012**, *23*, 553-562.
- (144) Yin, S.; Xie, Y.; Loo, J. A. Mass Spectrometry of Protein-Ligand Complexes: Enhanced Gas-Phase Stability of Ribonuclease-Nucleotide Complexes. *J. Am. Soc. Mass Spectrom.* **2008**, *19*, 1199-1208.
- (145) Tolmachev, A. V.; Vilkov, A. N.; Bogdanov, B.; Pasa-Tolic, L.; Masselon, C. D.; Smith, R. D. Collisional activation of ions in RF ion traps and ion guides: The effective ion temperature treatment. *J. Am. Soc. Mass Spectrom.* **2004**, *15*, 1616-1628.

- (146) Sztáray, J.; Memboeuf, A.; Drahos, L.; Vékey, K. Leucine enkephalin-a mass spectrometry standard. *Mass Spectrom. Rev.* **2011**, *30*, 298-320.

Chapter 3

3 Summary and Future Work

3.1 Summary and Conclusion

Magic number clusters refer to ion species that exhibit unusually high intensities in MS spectra.¹ Ser₈+H⁺ is of special interest; its formation proceeds via an enantioselective pathway that possibly has been crucial in the primary emergence of homochirality in biology.² Over several decades, there have been various investigations into the structure of Ser₈+H⁺ and its formation mechanism. Currently, the structure proposed by Scutelnic et al.³ is regarded to be the most likely conformation, displaying reasonable agreement with experimental data. Nonetheless, the formation mechanism of Ser₈+H⁺ remains poorly understood. Some hypotheses suggest that it may pre-exist in bulk solution or, that Ser₈+H⁺ can be a CID product of large clusters generated in ESI droplets.⁴⁻⁶

In chapter 2, ESI-MS and MS² experiments were combined with computational tools (MD and DFT) to elucidate the formation mechanism of Ser₈+H⁺.

Our experimental work involved ESI-MS analysis of a highly concentrated serine solution (5 mM) in water with 0.1% acetic acid. Sampling cone settings of 5 and 180 volts were tested to examine the octamer stability. An unusual observation was the persistence of octamer at the increased cone voltage of 180. A peptide, Leu-Enk was examined under the same conditions showing complete fragmentation at such a high cone voltage. Subsequent MS/MS experiments revealed a high sensitivity of Ser₈+H⁺ to fragmentation, already under very gentle conditions. These conflicting findings were reconciled by hypothesizing that Ser₈+H⁺ formation takes place after ion source, during free jet expansion, in transition from atmospheric pressure to vacuum pressures in the mass spectrometer.

Next, we utilized computational techniques to investigate possible octamer formation mechanisms.

Our initial step was the design of suitable monomers that maintained stable conformations under our simulation conditions. DFT geometry optimization and relaxed scan calculations were performed for monomer preparation.

Subsequently, we started our simulations by testing the existence of Ser_8+H^+ in bulk or droplet using various strategies. Initially, a saturated concentration of zwitterionic monomers was placed in a water box and allowed to interact for 10 ns. No octamers formed under these conditions. Moreover, the cluster structure proposed by Scutelnic et al. immediately dissolved in water.

Next, ESI droplets were simulated with 14 SEP and various initial numbers of SEZ. Different temperature profiles were applied to the system to supply the heat needed for evaporation. The processes resulted in the formation of multiply charged nascent clusters via the CRM.

Another strategy involved gas phase assembly in vacuum condition, intended to replicate the clustering effect observed in free jet expansion.⁷ In the vacuum environment, positive ions repel each other but gaseous neutral Sers can approach positive ones and aggregate. This process was simulated using one SEP and a varying number of initial SEO monomers (5,6,...,20) in a pseudo-PBC box. The initial aggregation products consisted of singly charged clusters ranging from $[\text{Ser}_5+\text{H}]^+$ to $[\text{Ser}_{20}+\text{H}]^+$.

Finally, the droplet CRM products and gas phase assembled clusters were heated to high temperatures to simulate CID. The results showed that the octamer forms as a preferential product. However, gas phase assembled clusters dissociate to Ser_8+H^+ to a greater extent than the dissociation of the multiply charged droplet CRM products.

Overall, our investigation suggests that experimentally observable Ser_8+H^+ forms via the assembly of monomeric Ser in the gas phase followed by CID events. To our knowledge, such a formation mechanism has not previously been proposed in the literature.

3.2 Future Work

As described in Chapter 1, Ser_8+H^+ exhibits an unusual homochirality, i.e., upon electrospraying a racemic Ser solution to mass spectrometer, enantiomerically enriched octamers are observed. This phenomenon appears to be nearly exclusive to Ser_8+H^+ . However, the mechanisms responsible for such enantioselectivity remain unclear. Chapter 2 exclusively focused on the behavior of L-Ser. Ideally, it should be possible to extend our work to explore why the formation of Ser_8+H^+ takes place enantioselectively. We will very briefly mention preliminary tests that we undertook to explore this aspect.

The technical details of our tests were analogous to those used for L-Ser in Chapter 2.

3.2.1 Simulations of L/D mixture of Ser in droplet

The framework used for modeling L- Ser in droplets with subsequent CID was also utilized for runs on 50-50 L/D mixtures. Unfortunately, this approach did not provide any evidence supporting the enantioselectivity of octamer formation. Instead, the outcome of the simulations resembled a binomial distribution that would be expected for random assembly without enantioselectivity (Figure 3.1.a).

Similarly, we tested the gas phase assembly with subsequent CID for a 50-50 L/D Ser mixture. Once again, the results did not show any enantioselectivity in the formation of Ser_8+H^+ , (Figure 3.1.b). We hope that future work with improved gas phase force fields may be able to capture the experimentally observed enantioselective formation of Ser_8+H^+ .

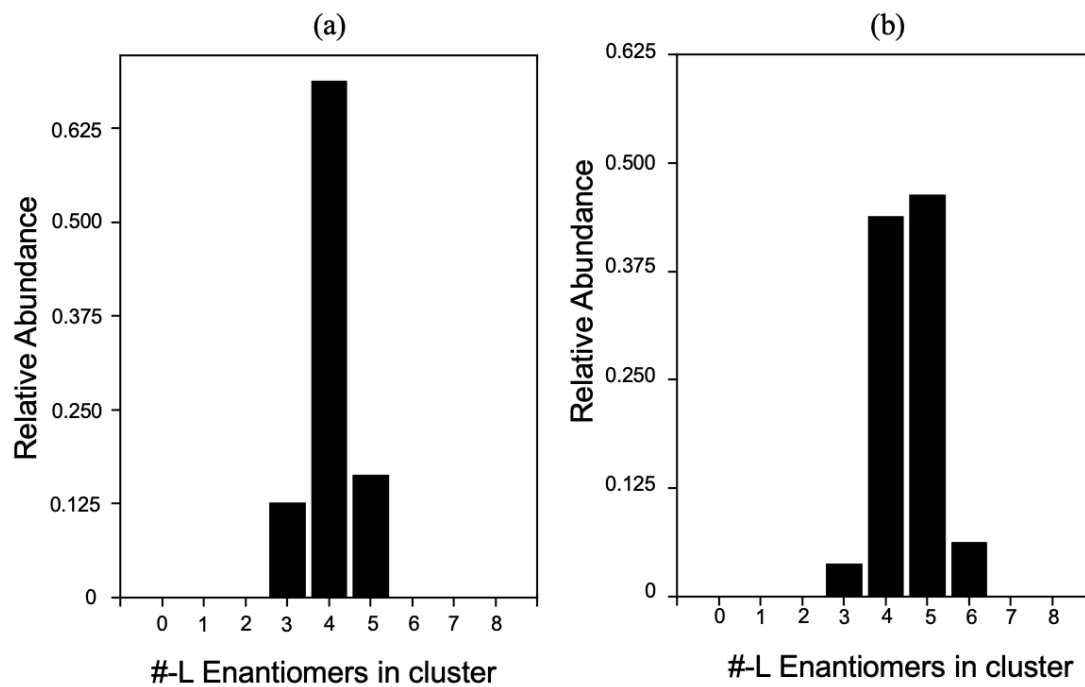
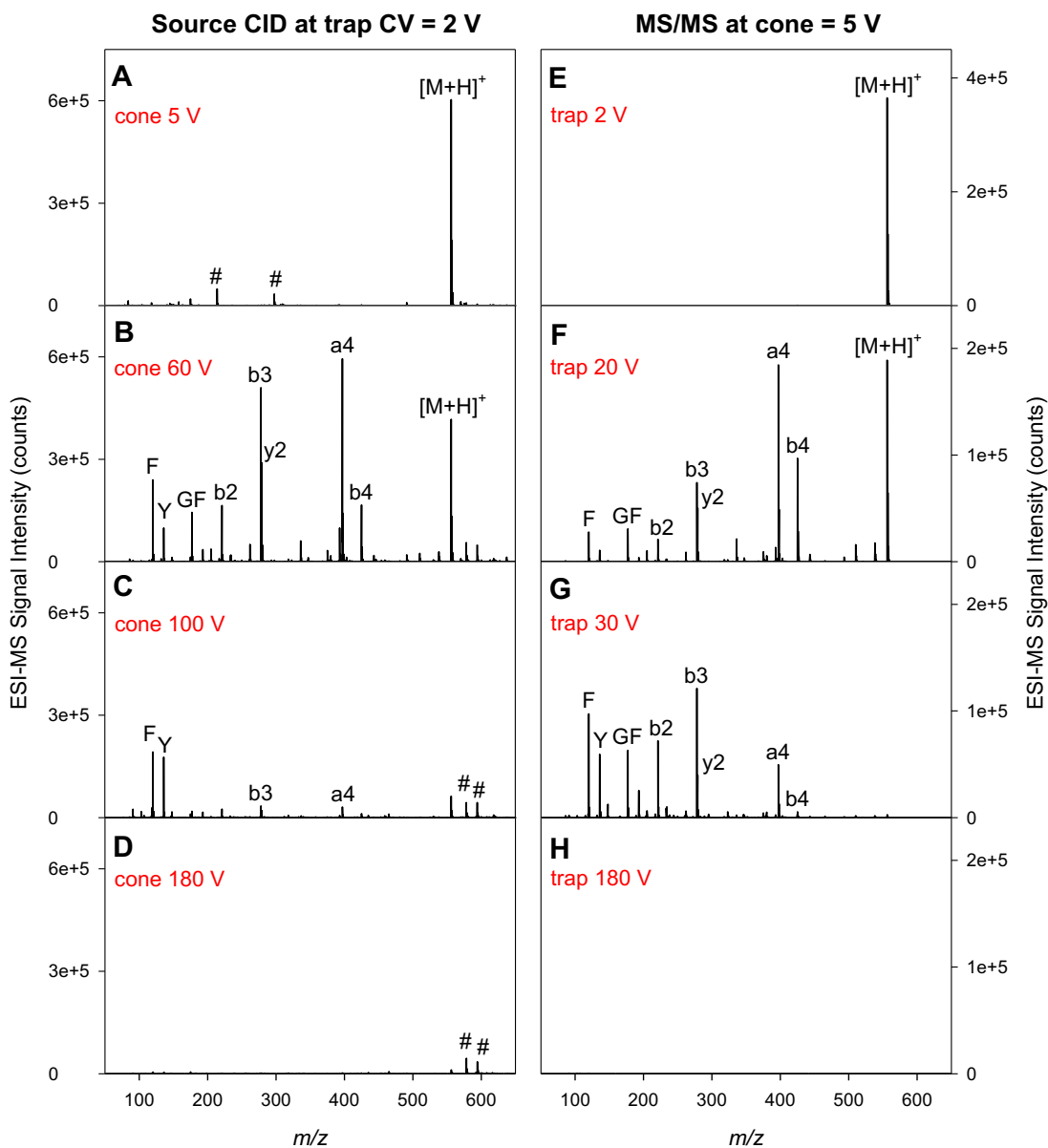


Figure 3.1 Relative abundance vs number of L enantiomers in cluster for Ser₈+H⁺ CID products. (a) CID of droplet generated precursors. (b) CID of gas assembled clusters.

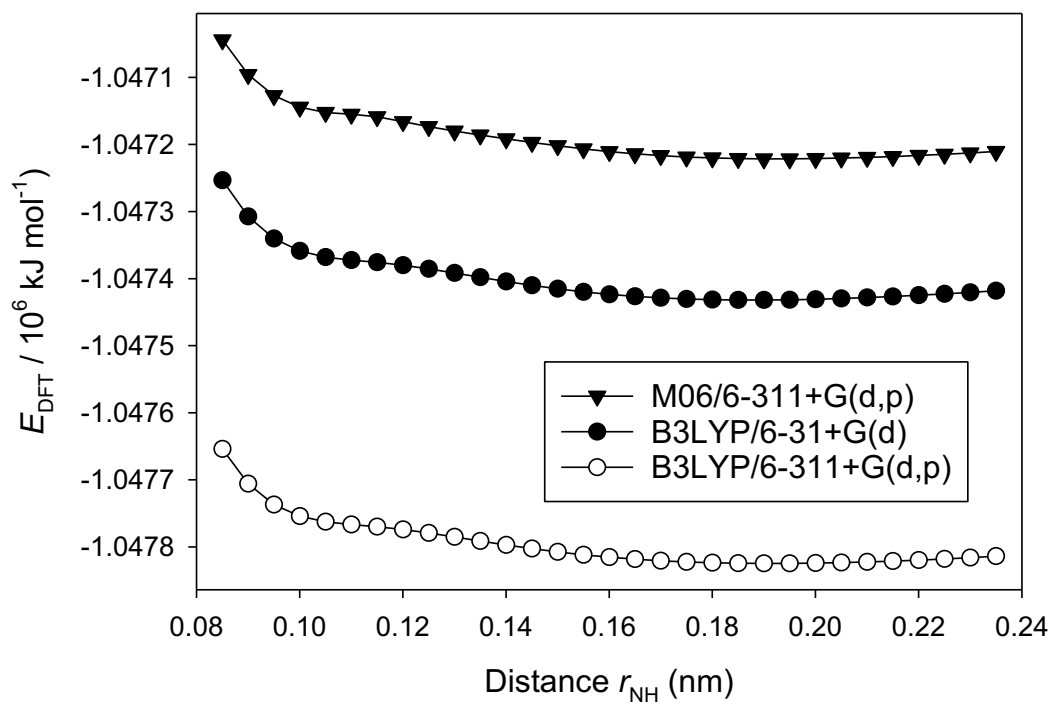
3.3 References

- (1) Konermann, L.; Haidar, Y. Mechanism of Magic Number NaCl Cluster Formation from Electrosprayed Water Nanodroplets. *Analytical Chemistry* **2022**, *94* (47), 16491-16501. DOI: 10.1021/acs.analchem.2c04141.
- (2) Nanita, S. C.; Cooks, R. G. Serine Octamers: Cluster Formation, Reactions, and Implications for Biomolecule Homochirality. *Angewandte Chemie International Edition* **2006**, *45* (4), 554-569.
- (3) Scutelnic, V.; Perez, M. A. S.; Marianski, M.; Warnke, S.; Gregor, A.; Rothlisberger, U.; Bowers, M. T.; Baldauf, C.; von Helden, G.; Rizzo, T. R.; et al. The Structure of the Protonated Serine Octamer. *J Am Chem Soc* **2018**, *140* (24), 7554-7560. DOI: 10.1021/jacs.8b02118 From NLM.
- (4) Jordan, J. S.; Williams, E. R. Dissociation of large gaseous serine clusters produces abundant protonated serine octamer. *Analyst* **2021**, *146* (8), 2617-2625, 10.1039/D1AN00273B. DOI: 10.1039/D1AN00273B.
- (5) Jordan, J. S.; Williams, E. R. Effects of Electrospray Droplet Size on Analyte Aggregation: Evidence for Serine Octamer in Solution. *Analytical Chemistry* **2021**, *93* (3), 1725-1731. DOI: 10.1021/acs.analchem.0c04343.
- (6) Jordan, J. S.; Williams, E. R. Homochiral preference of serine octamer in solution and formed by dissociation of large gaseous clusters. *Analyst* **2021**, *146* (22), 6822-6830. DOI: 10.1039/d1an01646f From NLM.
- (7) Searcy, J. Q.; Fenn, J. B. Clustering of water on hydrated protons in a supersonic free jet expansion. *The Journal of Chemical Physics* **1974**, *61* (12), 5282-5288. DOI: 10.1063/1.1681876 (accessed 3/25/2024).

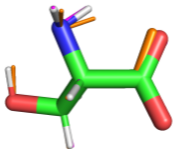
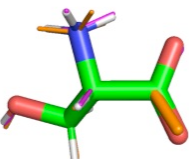
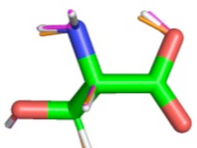
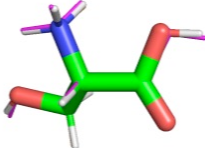
4 Appendix



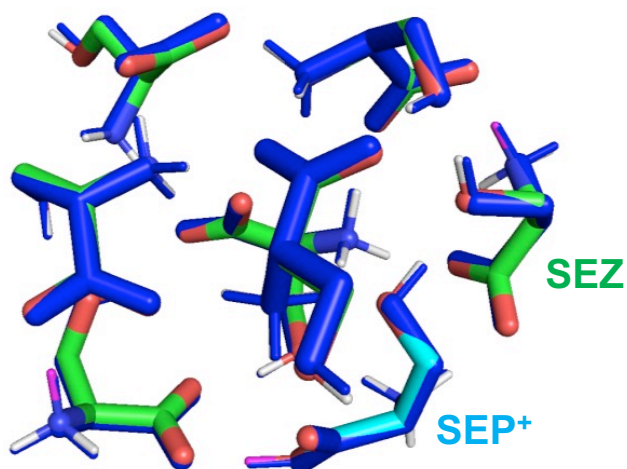
Appendix 1 CID of leucine enkephalin (LeuEnk, YGGFL)¹⁴⁶ (A-D) ESI mass spectra acquired at different cone voltage, with constant trap CV. (E-H) Tandem mass spectra of the [M+H]⁺ precursor ion (monoisotopic m/z 556.28) acquired at different trap CV, with constant cone voltage. The Ar trap collision gas was on for all the data shown here. Major fragment ions are indicated; identification was performed using UCSF Protein Prospector. Upper case single letters denote immonium ions, double letters represent internal fragments, # indicates unidentified contaminants.



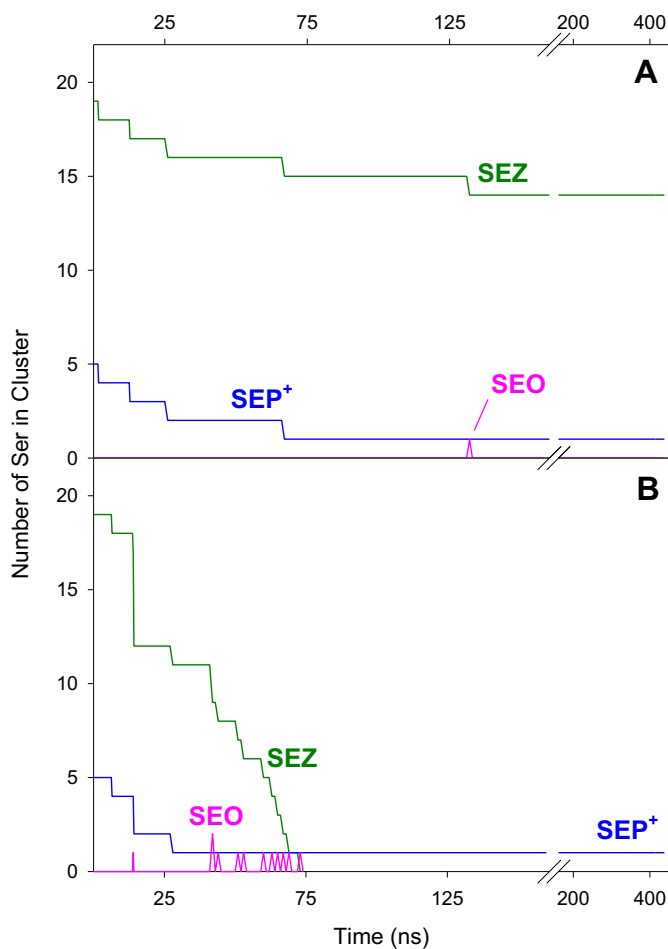
Appendix 2 DFT relaxed scans of the SEZ \rightarrow SEO transition, analogous to Figure 2.2. The data were generated using three different methods: B3LYP/6-31G(d), B3LYP/6-311+G(d,p), and M06/6-311+G(d,p).

		RMSD (nm) for DFT vs.	
		CHARMM36	OPLS-AA
SEN⁻		0.0056	0.0151
SEZ		0.0081	0.0305
SEO		0.0082	0.0091
SEP⁺_{up}		0.0100	0.0042

Appendix 3 DFT-optimized vs. MD-energy minimized Ser monomer structures. Shown along the left are overlays of CHARMM36 (magenta) and OPLS-AA (orange) steepest-descent energy optimized structures, and B3LYP/6-311+G(d,p)-optimized structures (green/red/blue/white). Force field steepest descent calculations used $F \leq 100 \text{ kJ mol}^{-1} \text{ nm}^{-1}$ as convergence criterion. Numbers on the right represent all-atom RMSD values in nm. Average RMSDs are 0.008 nm for CHARMM36, and 0.015 nm for OPLS-AA.



Appendix 4 Comparison of the B3LYP/6-31G(d,p) Ser₈H⁺ model by Scutelnic et al.⁶¹ (with carbon atoms in green and cyan, as in Figure 2.1), and a DFT geometry optimization of this model using B3LYP/6-311+G(d,p) (blue). The RMSD between the two structures is 0.01 nm.



Appendix 5 Gas phase MPMD simulations of cluster CID, starting with $[\text{SEZ}_{19} \text{SEP}_5]^{5+}$. Temperature profile: 12.5 ns at 600 K, 12.5 ns at 700 K, 425 ns at 950 K. (A) E_{DFT} values as specified in Table 1. CID product = $[\text{SEZ}_{14} \text{SEP}]^+$. (B) same as panel A, except that $E_{\text{DFT}}(\text{SEO})$ was lowered by 50 kJ mol^{-1} . CID product = SEP. Note the rapid loss of SEO immediately after each intramolecular $\text{SEZ} \rightarrow \text{SEO}$ proton transfer.

Curriculum Vitae

Name: Vida Alinezhad

Post-secondary Education and Degrees: The University of Western Ontario
London, Ontario, Canada
2021-present M.Sc. Physical and Analytical Chemistry
Supervisor: Professor Lars Konermann

Sharif University of Technology
Tehran, Iran
2016-2021 B.Sc. Applied Chemistry

Honors and Awards: Western Graduate Research Scholarship (WGRS)
2021-2024

Related Work Experience Teaching Assistant
The University of Western Ontario
2021-2024

Publications:

1. V. Alinezhad, L. Konermann, "Electrosprayed Serine Octamer Magic Number Clusters: Formation via Gas phase Assembly and Collision-Induced Dissociation", In Preparation.
2. N.Rabiee, A.Ghadiri, V.Alinezhad et al., "Synthesis of green benzamide-decorated UiO-66-NH₂ for biomedical applications", *Chemosphere*, 2022, 299,134359.

Presentations and Posters:

1. Canadian Chemistry Conference and Exhibition (June 2023)
V. Alinezhad, L. Konermann, Serine Octamer Cluster Formation during Electrospray Ionization (Poster)
2. Annual Conference of the American Society of Mass Spectrometry (June 2023)
L. Konermann, Y. Haidar, V. Alinezhad, E. Aliyari, Unravelling the Mechanisms of Magic Number Custer Formation During Electrospray Ionization (Oral Presentation)
3. Annual Conference of the American Society of Mass Spectrometry (June 2024)
L. Konermann, M. Dolatkah, V. Alinezhad, K. Hanifi, Atomistic Modeling of the ESI Process: From Taylor Cones to Biomolecular Ions and Magic Number Clusters (Oral Presentation)